

Calibration and Online Monitoring of the PHENIX Drift Chamber

A Thesis Presented

by

Tassilo Sebastian Wolfgang Christ

to

The Graduate School

in Partial Fulfillment of the Requirements

for the Degree of

Master of Arts

in

Physics

State University of New York

at

Stony Brook

May 2000

State University of New York
at Stony Brook

The Graduate School

Tassilo Sebastian Wolfgang Christ

We, the thesis committee for the above candidate for the Master of Arts degree,
hereby recommend acceptance of the thesis.

Professor Axel Drees (Advisor)
Department of Physics and Astronomy

Professor John Hobbs
Department of Physics and Astronomy

Professor John Smith
Yang Institute for Theoretical Physics

This thesis is accepted by the Graduate School.

Graduate School

Abstract of the Thesis

Calibration and Online Monitoring of the PHENIX Drift Chamber

by

Tassilo Sebastian Wolfgang Christ

Master of Arts

in

Physics

State University of New York at Stony Brook

2000

The present thesis is dedicated to the description of calibration and monitoring of the drift chamber tracking detector in the PHENIX experiment (*Pioneering High Energy Nuclear Interaction eXperiment*) at the Brookhaven National Laboratory (BNL) in Upton, New York. A brief introduction into the physics of high-energy heavy-ion collisions is provided and the basic physics goals of PHENIX and the Relativistic Heavy Ion Collider (RHIC) at BNL are outlined. The principles of constructing and operating drift chambers are presented and a more detailed explanation of

the chambers built for PHENIX is given. The most important design features of the chambers are summarized and the software environment used for data acquisition and analysis in PHENIX is explained. The latter also includes a presentation of the drift chamber's tracking algorithm which makes use of a twofold combinatorial Hough transformation to obtain track information. The main task of the present thesis is to discuss parameters that have proven useful to describe the detector's response and behavior under operating conditions and to evaluate the performance of the detector according to these quantities. To extract these parameters, to assess the detector response, and to check the full offline analysis chain, data from a cosmic-ray test are used. The software which was written to obtain and display the performance parameters is to become an essential part of the online monitoring system of the drift chamber. The algorithms and their embedding in the online computing system of PHENIX are explained. The results of these tests are to be used in the calibration of the drift chamber in upcoming engineering and physics runs.

To my friends and colleagues at
Stony Brook and Brookhaven

Contents

Acknowledgements	xv
1 The PHENIX Experiment	1
1.1 Ultra-Relativistic Heavy-Ion Collisions	1
1.2 Physical Phenomena	3
1.2.1 Deconfinement and Quark Gluon Plasma	3
1.2.2 Chiral Symmetry Restoration	7
1.3 The Physics Goals of PHENIX	12
1.3.1 Physical Observables	12
1.3.2 Experimental Setup	16
2 The PHENIX Drift Chamber Detectors	23
2.1 Operational Principles of Drift Chambers	23
2.1.1 Primary Ionization in the Working Gas	23
2.1.2 Charge Drift and Amplification	25
2.2 Design of the PHENIX Drift Chambers	29
2.2.1 Mechanical Construction	29
2.2.2 Drift Cell Design	30

2.3	Data Readout and Data Handling in PHENIX	36
2.3.1	Trigger for Data Readout	36
2.3.2	Front End Electronics	37
3	Calibration Software Structure	40
3.1	The Data Analysis Framework	40
3.1.1	Data Stream to the Monitoring Processes	40
3.1.2	Data Management with PHOOL	42
3.1.3	Data Visualization with ROOT	42
3.2	Calibration and Monitoring Software	43
3.2.1	Concept and Environment	43
3.2.2	Calibration Code Library	44
4	Processing of Raw Data	45
4.1	Unpacking the Data Stream	45
4.2	Calibration of Hits in the Drift Chamber	46
4.2.1	Trajectories of Charge Clouds	46
4.2.2	Reconstruction of the Space Drift-Time Relation	49
4.2.3	Space Drift-Time Relation for Monte Carlo Data	55
4.2.4	Space Drift-Time Relation for Cosmic-Ray Data	63
5	Track Finding and Detector Performance	76
5.1	Combinatorial Hough Transformation in Coordinate Space	76
5.1.1	Feature Space for the Transformation	76
5.1.2	CHT in the Drift Chamber	78

5.2	Relevant Tracking Parameters	83
5.2.1	Single-Wire Efficiency and Back-Drift Efficiency	83
5.2.2	Single-Wire Efficiency in Cosmic-Ray Data	87
5.2.3	Resolution Measurement	97
5.2.4	Resolution in the Monte Carlo Data	99
5.2.5	Resolution in the Cosmic-Ray Data	105
6	Summary and Perspectives	112
6.1	Goals of the Thesis	112
6.2	Discussion of the Results	113
6.2.1	Space Drift-Time Relation	113
6.2.2	Single-Wire Efficiency	114
6.2.3	Resolution	114
6.3	Perspectives for the Monitoring Software	115
6.3.1	Algorithms	115
6.3.2	Embedding into the PHENIX Software Development Process	115
6.3.3	Interactivity	116
A	Calibration Software Overview	120
A.1	Drift Chamber Object Oriented Monitoring Library	120
A.1.1	Dependencies upon other Software Modules	120
A.1.2	Available Monitor Objects	121

List of Figures

1.1	Illustration of a QCD ground state with and without chiral symmetry	10
1.2	The expectation value of the quark condensate as a function of temperature and density in a strongly interacting system . . .	12
1.3	The PHENIX detector systems	18
1.4	Momentum resolution of the PHENIX tracking detectors . . .	20
2.1	Drift velocity as a function of E/p in the PHENIX drift chamber working gas mixture	28
2.2	Schematic drawing of the PHENIX drift-chamber frame	30
2.3	Radial wire arrangement in the drift chamber	31
2.4	Mutual wire positions in a drift cell	32
2.5	Charge drift lines and isochrones in the drift cell	34
2.6	Equipotential lines in the drift cell	35
2.7	Block diagram of the PHENIX DC front end electronics	38
3.1	Data flow from the detector electronics to the analysis software	41

4.1	Dependence of the drift direction of charge clouds on the z-coordinate for a stereo wire in the drift chamber	48
4.2	Intersection of tracks with the x axis at different inclination angles	50
4.3	Predicted space drift-time relation for tracks crossing the x axis at an angle of 70°	51
4.4	Spatial reference distribution of hits in a drift cell and schematic measured drift-time distribution	55
4.5	Simulation of the drift-time distribution in Monte Carlo events	56
4.6	Reconstructed drift-time distribution from Monte Carlo simulations for the X1 and the UV1 wires	57
4.7	Cell-crossing tracks in the Monte Carlo simulation software . .	59
4.8	Integrated space drift-time relation for the X1 and the U1 wires for Monte Carlo data	60
4.9	Setup for the cosmic-ray test	64
4.10	Number of hits in the channels of one keystone for 1800 cosmic ray events	65
4.11	Drift-time distribution obtained with all wires in the acceptance of the cosmic-ray test enabled.	66
4.12	Noise corrected drift-time distribution for the X wires in the cosmic ray test	67
4.13	Noise corrected drift-time distribution for the U wires in the cosmic-ray test.	68

4.14	Noise corrected drift-time distribution for the V wires in the cosmic-ray test	69
4.15	Effective width of the back-drift region	70
4.16	Effects of field line bending in the back-drift region upon the drift-time distribution	71
4.17	Space drift-time relation reconstructed from cosmic-ray data for the X wires	72
4.18	Space drift-time relation reconstructed from cosmic-ray data for the U wires	73
4.19	Space drift-time relation reconstructed from cosmic-ray data for the V wires	74
5.1	Feature spaces of SHT and CHT	78
5.2	Feature-space coordinates for the X wire Hough transformation.	79
5.3	X wire hits in the DC for a central HIJING Au+Au collision and a typical feature space distribution	80
5.4	Feature space coordinates for the stereo wire Hough transformation	82
5.5	Distance of track and sense wire in drift direction	85
5.6	Determination of the z coordinate of a track's passing point along the sense wire	86
5.7	Azimuthal distribution of registered tracks in the cosmic-ray test	89
5.8	Distribution of the inclination angle of tracks in the cosmic-ray test	90

5.9	Distribution of the polar angle of tracks in the cosmic ray test	91
5.10	Distribution of the drift length of hits associated to reconstructed tracks	92
5.11	Number of stereo-wire hits associated to tracks	93
5.12	Efficiency and back-efficiency versus radial distance of the wires in a cosmic-ray data set	94
5.13	Efficiencies of the different wire types in the drift chamber and efficiency as a function of drift distance in a cosmic-ray data set	95
5.14	Back-drift efficiency of the X wires as a function of the ratio U_{back}/U_{pot}	97
5.15	Distance of hit and track in the local drift plane (residual) . .	98
5.16	Residuals in the X1 wires for Monte Carlo events	100
5.17	Residuals in the UV1 wires for Monte Carlo events	101
5.18	Resolution in X1 and UV1 wires versus drift length for simulated events	103
5.19	Mean residual in X1 and UV1 wires versus drift length for simulated events	104
5.20	Resolution in X1 and UV1 wires versus drift length without magnetic field	105
5.21	Mean residual in X1 and UV1 wires versus drift length without magnetic field	106
5.22	Resolution in X1 and UV1 wires versus drift length for cosmic-ray data	107

5.23	Mean residual in X1 and UV1 wires versus drift length for cosmic-ray data	108
5.24	Corrected resolution in all X and stereo wires versus drift length for cosmic-ray data	109
5.25	Corrected mean residual in all X and stereo wires versus drift length for cosmic-ray data	110

List of Tables

2.1	Wire characteristics in the drift chamber	33
4.1	Linear and non-linear coefficients of the space drift-time relation	53
4.2	Fit parameters and uncertainties of the reconstructed Monte Carlo space drift-time relation	61
4.3	Fit parameters and χ^2 values of the cosmic-ray space drift-time relation	75
5.1	Voltage configurations in the different cosmic ray data taking runs with the drift chamber	88
5.2	Efficiencies and back-drift efficiencies for the X wires for different voltage settings	96
5.3	Resolutions for different wire types in the drift chamber	102

Acknowledgements

I would like to thank my advisor Professor Axel Drees for his always patient and clear explanations that enabled me to work in a field of physics that was completely new but very fascinating for me. His advice and guidance during all stages of my work helped me focusing on important aspects and setting clear tasks. He is hereby recommended to younger graduate students as a competent and attentive advisor with a sense of humor.

I would like to thank my colleagues in Stony Brook and Brookhaven National Laboratory for their great support. Without the help of the members of the heavy-ion group in Stony Brook and the scientific personnel at Brookhaven this thesis could not have been written.

I especially thank Tom Hemmick for several really instructive ‘core dumps’, Federica and Matthias Messer for lots of buttons, for making a PHOOL of me, for numerous excellent dinners, and for moral support when it was bloody necessary, Steve Johnson for pointing me in the right direction when I needed it, Julia Velkovska for so many fruitful discussions about bugs in my software and between my ears, Martin Purschke for teaching a greenhorn programming and most of all Ralf and Nicole Averbeck for taking the nontrivial task of predigesting this thesis for the rest of the world, for invaluable support in the

final stages of the work, and for hosting me in the end. I thank you all for your advice and your support. The good atmosphere and the team spirit in the Stony Brook heavy-ion group will always be remembered. Special thanks goes across the Atlantic to the most patient girlfriend of the world and to my parents for shoulder tapping and believing that it would happen.

Chapter 1

The PHENIX Experiment

1.1 Ultra-Relativistic Heavy-Ion Collisions

Only heavy-ion accelerator experiments can investigate the processes that occur when nuclei of heavy atoms collide on different scales of kinetic energy. The interactions of the involved hadrons and partons can be divided into so called 'soft' and 'hard' processes. At low collision energies (\sqrt{s} up to 10 $A\text{GeV}$) soft processes dominate. These are governed by the exchange of low-energy gluons or mesons in "effective" theories which describe interactions on hadronic scales. At higher collision energies hard processes become important. Those occur on the partonic level and involve high-energy gluon exchange between single partons on distances less than the size of the nucleons. As at high energies the two colliding nuclei are not only very fast, but also Lorentz contracted, the interactions of the hadrons and partons take place in close spatial and temporal proximity. Thus, in the region where the two colliding nuclei overlap, a zone of highly excited strongly interacting matter is formed. Whether this

matter is hadronic or partonic depends on the energy density reached in the collision. The initial kinetic energy of the incoming nuclei is transformed into chaotic and collective motion of the constituents of the system and into the production of new particles. After the colliding nuclei have receded from the interaction zone expansive development of the system takes place. Thereby thermal equilibrium may be reached before the particles hadronize if the life time of the system is long enough to allow for multiple collisions between the constituents. Typical lifetime estimates of the hot system are of the order of $7 - 10 fm/c$. In past fixed target experiments, e.g. at the AGS (Alternating Gradient Synchrotron) at BNL and the SPS (Super Proton Synchrotron) at CERN, the beam energy and therefore the maximum energy density reached in the interaction zone of central heavy-ion collisions has been increased more and more. If the energy density becomes high enough, sub-nucleonic effects become important. Quarks and gluons eventually become the new degrees of freedom and therefore a phase transition from hadronic matter to a *Quark Gluon Plasma (QGP)* consisting of free moving partons is predicted. Whether this phase transition has been observed already at SPS is unclear! Another phenomenon expected in this regime is the restoration of the symmetry of strong interactions with respect to chiral transformations. In collider experiments like the *Relativistic Heavy Ion Collider (RHIC)* which is going to start operation in late spring 2000 and the Large Hadron Collider (LHC) currently under construction at CERN the available energy in the center of mass system is even higher than in fixed target experiments and the described phenomena should become unambiguously observable there. To investigate them in detail

four colliding beam experiments *PHENIX*, *STAR*, *PHOBOS* and *BRAHMS* have been set up at RHIC. RHIC will accelerate fully ionized Gold nuclei to kinetic energies up to 100 GeV per nucleon, whereas for protons up to 250 GeV can be reached. The energy density in the interaction region of a central Au+Au collision is estimated to reach about $5\text{ GeV}/\text{fm}^3$ which is more than one order of magnitude larger than in nuclear matter in its ground state [1].

1.2 Physical Phenomena

1.2.1 Deconfinement and Quark Gluon Plasma

To understand what one can learn from high-energy heavy-ion collisions one has to recall some facts known from quantum chromodynamics (QCD), which is the theory of strong interactions. It is known that quarks and gluons do not exist as free particles and that only objects that are neutral with respect to "color" (the charge of strong interaction) are observed as free entities. This phenomenon is called confinement and is ascribed to the nature of the coupling between two colored elementary particles in QCD [2]. The coupling does not decrease as the distance between the two interacting objects increases but behaves the opposite way. As the partons created in the center of mass system in relativistic heavy-ion collisions are located very close to each other they interact on distance scales shorter than or comparable to the mean distance of confined objects. The systems high initial energy and parton density together with its large spatial extension create an environment in which a single quark

does not experience a net force which confines it to a single partner (mesonic state) or a pair of quarks (baryonic state) to form a color singlet. The partons are free to move over a much larger region of space *without being tied to a specific colorless hadron*. Nevertheless, the system as a whole remains color neutral. This deconfined state of matter is called Quark Gluon Plasma.

Theoretical methods like lattice gauge theory, which is a commonly used technique in nonperturbative QCD, also yield the confining property of the interaction between colored objects and furthermore indicate a phase transition to deconfined matter at energy densities of the order of $\approx 3 \text{ GeV}/\text{fm}^3$ [3] [4] [5]. To estimate the energy density threshold for deconfinement several phenomenological methods exist, which do not require extensive field theoretical computations. The intuitive "hadron bag model" assumes that an inwardly directed pressure which represents the confining force of QCD holds the partons together in hadronic matter. Thermodynamic motion of the partons balances this bag pressure. This line of arguments allows one to show that above a certain temperature and/or density of partons the confining forces are overwhelmed. As discussed in detail in [6], one can estimate the threshold temperature and parton density:

Representing the hadron by a bag requires an estimate of the maximum pressure this bag can compensate. To obtain a value for this threshold one treats the quarks in a hadron as massless fermions, which is a good approximation for the u and d quarks in light hadrons, and starts from the Dirac equation

for the spinor wave function for a 4-component spinor:

$$\begin{pmatrix} p^0 & -\vec{\sigma} * \vec{p} \\ \vec{\sigma} * \vec{p} & p^0 \end{pmatrix} \begin{pmatrix} \Psi_+ \\ \Psi_- \end{pmatrix} = 0 \quad (1.1)$$

Here (p^0, \vec{p}) is the four momentum of the particle and Ψ_+ and Ψ_- are two component spinors describing the behavior of different components of the fermion wave function under $SU(2)$ transformations. The components of the matrix vector $\vec{\sigma}$ are the usual Pauli spin matrices which generate the $SU(2)$ transformations. The resulting system of equations is solved after replacing energy and momentum with their respective position space operators. The solutions with the lowest energy are spherical Bessel functions with oscillatory time dependence:

$$\Psi_+(\mathbf{r}, t) = N e^{-ip^0 t} j_0(p^0 r) \chi_+ \quad (1.2)$$

$$\Psi_-(\mathbf{r}, t) = N e^{-ip^0 t} \vec{\sigma} * \mathbf{r} j_1(p^0 r) \chi_- \quad (1.3)$$

Here Ψ_+ and Ψ_- are the usual two component fermion spinors. If the quarks are confined within a sphere of radius R , then the scalar quark density $\bar{\Psi}\Psi$ must vanish at this radius. From equations 1.2 and 1.3 one therefore obtains:

$$\bar{\Psi}\Psi \Big|_{r=R} = 0 \longrightarrow [j_0(p^0 R)]^2 - [j_1(p^0 R)]^2 = 0 \quad (1.4)$$

Using tabulated values for the Bessel functions this yields for the quark energy p^0 :

$$p^0 = \frac{2.04}{R} \quad (1.5)$$

where natural units are used ($\hbar = c = 1$). The total energy E of the N -quark system is composed of the kinetic part described above and the contribution from the bag pressure B , which is to be understood as the difference between the energy density of the QCD vacuum inside and outside the bag.

$$E = \frac{2.04 N}{R} + \frac{4\pi}{3} R^3 B \quad (1.6)$$

To account for the long range interaction of the quarks, which has been neglected here completely, the energy density has to be bigger inside the bag than outside. This can be understood intuitively when one recalls that the interaction energy of the parton system is stored in their strong binding. The system is forced to an equilibrium radius defined by $dE/dR = 0$ which is true when:

$$B = \frac{2.04 N}{4\pi R^4} \quad (1.7)$$

The confining forces have thus been substituted by a phenomenological difference in energy density inside and outside the hadron bag. For a 3-quark hadron of radius 0.8 fm one obtains a value of $(206 \text{ MeV})^4$ for B . To establish the deconfined phase this bag pressure is to be overwhelmed by thermal motion of the quarks and gluons. When calculating the pressure that arises from this motion in the zero-mass approximation of noninteracting partons one adds up the contributions of quarks, antiquarks, and gluons. The momentum distribution of quarks and antiquarks is governed by Fermi-Dirac statistics, whereas gluons are bosons and their momentum distribution is calculated from Bose-Einstein statistics. The energy density ϵ of a noninteracting parton gas can be calculated by integrating these distributions over the complete momentum

range and taking into account the degeneracy of the phase-space states due to color, flavor, and spin multiplicities. For a detailed calculation see [6]. To obtain the pressure P arising from this density, one uses a result from statistical physics that relates pressure and energy density of a system of noninteracting fermions and bosons [7]:

$$P = \frac{1}{3}\epsilon \quad (1.8)$$

The resulting pressure P is given by:

$$P = g_{total} 37 \frac{\pi^2}{90} T^4 \quad (1.9)$$

where g_{total} is the number of the degeneracies of all parton phase-space cells with respect to the quantum numbers mentioned above. Since at the phase transition P is equal to the bag pressure B , the temperature T of the system needs to surpass 144 MeV to reach deconfinement. The corresponding energy density is about $2.5 \text{ GeV}/\text{fm}^3$ which is well within the predictions of other models. At RHIC energy densities up to $5 \text{ GeV}/\text{fm}^3$ are expected to be reached in nucleus-nucleus collisions.

1.2.2 Chiral Symmetry Restoration

The restoration of chiral symmetry in strongly interacting matter is another important physical phenomenon to be investigated at RHIC. Lattice calculations indicate that the formation of the QGP and the restoration of chiral symmetry occur together as the energy density in the interacting matter is increasing [5]. It is, however, not understood from first principles, why

these phenomena should coincide!

A very simple model used to illuminate the concept of chiral symmetry and to distinguish its spontaneous and explicit breaking is outlined in [8]. Its most important aspects shall be described here briefly:

Neglecting the small masses of the QCD fermion fields of u and d quarks the Lagrangian of the system is given by:

$$\mathcal{L} = i\bar{\Psi}_j \gamma^\mu \partial_\mu \Psi_j \quad (1.10)$$

where Ψ is composed of each a u and d 2-component spinor and γ^μ is the four vector of the Dirac matrices. Two unitary transformations, that mix the quark fields with each other, are given by:

$$\Lambda_V : \Psi \longrightarrow e^{-i\frac{\vec{\tau}}{2}\vec{\Theta}} \Psi \approx \left(1 - i\frac{\vec{\tau}}{2}\vec{\Theta}\right) \Psi \quad (1.11)$$

$$\Lambda_A : \Psi \longrightarrow e^{-i\gamma_5 \frac{\vec{\tau}}{2}\vec{\Theta}} \Psi \approx \left(1 - i\gamma_5 \frac{\vec{\tau}}{2}\vec{\Theta}\right) \Psi \quad (1.12)$$

where the exponential has been expanded to first order in the *small* components of the parameter vector $\vec{\Theta}$. In these transformations, the isospin matrices τ act on the spinors and the matrix operation $\partial^\mu \gamma_\mu$ acts on Ψ as a whole. The Lagrangian remains unchanged under the transformations. The invariance under both transformations is meant when one refers to chiral symmetry of the Lagrangian.

This is true for massless fermions. In the case of quarks with mass m , the Lagrangian is

$$\mathcal{L} = i\bar{\Psi}_j (\gamma^\mu \partial_\mu - m) \Psi_j \quad (1.13)$$

and the symmetry of the transformation with respect to Λ_A is no longer an *exact* symmetry. An additional term proportional to the quark mass arises when \mathcal{L} is transformed.

$$m\bar{\Psi}\Psi \longrightarrow m\bar{\Psi}\Psi - 2im\vec{\Theta}\left(\bar{\Psi}\frac{\vec{\tau}}{2}\gamma_5\Psi\right) \quad (1.14)$$

This is called *explicit* breaking of chiral symmetry. Nevertheless, as the quark masses are small on the scale of QCD, the symmetry is *approximately* conserved.

According to [8], meson fields like the π , ρ and α_1 field can be represented as combinations of quark spinor fields. Under the transformation Λ_V these are transformed into one another. Therefore - if the Lagrangian is chirally symmetric - the mesons should have the same mass. This is obviously not true and the small explicit symmetry breaking can not account for the huge mass differences of e.g. the π_0 (135 MeV) and the α_1 meson (1260 MeV). The mechanism mainly responsible for the observed differences in meson masses is the so called *spontaneous symmetry breaking*. Its reversion is the *restoration of chiral symmetry*, mentioned above. The term “spontaneous breaking” refers to a situation, where the Hamilton operator of a system has a certain symmetry, but the ground state does not. A very intuitive way to understand this situation is displayed in Fig. 1.1. The potential displayed in Fig. 1.1a is symmetric with respect to arbitrary rotations around the z axis. So is the ground state of the system with the ball lying in the potential shell. In Fig. 1.1b the minimum of the potential is shifted away from the origin and there are now many positions of the ball in which it has the lowest possible energy (ground

state energy). By choosing one particular ground state out of infinitely many the symmetry is broken. The system displayed in Fig. 1.1b is, as a whole, no longer invariant with respect to rotations around the middle axis.

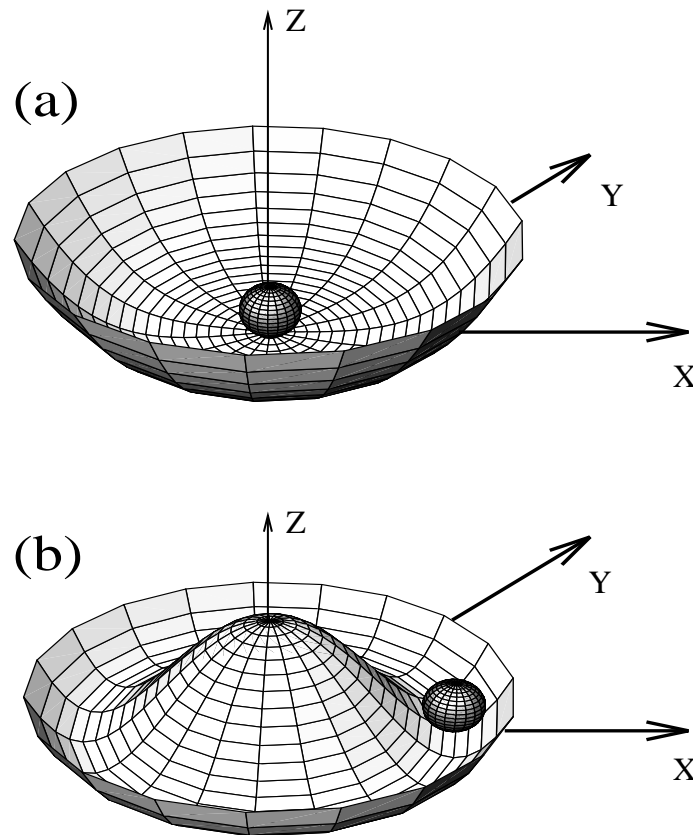


Figure 1.1: a) The system shown on the top (potential and ball) is in its ground state which is symmetric with respect to arbitrary rotations around the z axis.

b) The system on the bottom has picked one out of infinitely many ground states. Because of this, the symmetry with respect to rotations around the z axis is *broken*.

To use this picture in order to understand the spontaneous breaking of chiral symmetry in QCD one replaces the spatial coordinates in the $z = 0$ plane with excitations of the meson fields. In Figure 1.1a both fields have the value zero in the ground state, whereas in Figure 1.1b one meson field - the one associated with the x axis - has a nonzero expectation value $\langle q\bar{q} \rangle$. Rotations around the z axis transform one field into the other. If we associate rotational excitations of the ball (which need no energy) with light mesons and radial excitations (which need energy) with heavy mesons, the origin of the mass difference becomes obvious. It needs energy to excite the system radially!

At high densities and temperatures of the hadronic system one expects that the finite expectation value $\langle q\bar{q} \rangle$ of the quark-antiquark field, the so called “quark condensate” vanishes and that chiral symmetry is restored. This mechanism is outlined in [8]. The expected dependence of the quark condensate on temperature and density is shown in Fig. 1.2 which is taken from [9]. With increasing temperature and hadron density the condensate decreases. Experimental observables which are expected to be sensitive to $\langle q\bar{q} \rangle$ are the masses and the widths of certain mesons.

The restoration of chiral symmetry is not a phenomenon that appears abruptly. As seen in Fig. 1.2, already in nuclear matter in its ground state precursor phenomena should be observable. RHIC is going to explore the parts of the phase diagram with high temperature and vanishing baryon density. Other heavy-ion experiments that are supposed to explore the behavior of the quark condensate at lower temperatures and high matter density like the *HADES* experiment at the *Gesellschaft fuer Schwerionenforschung* in Darm-

stadt, Germany, are under construction [10].

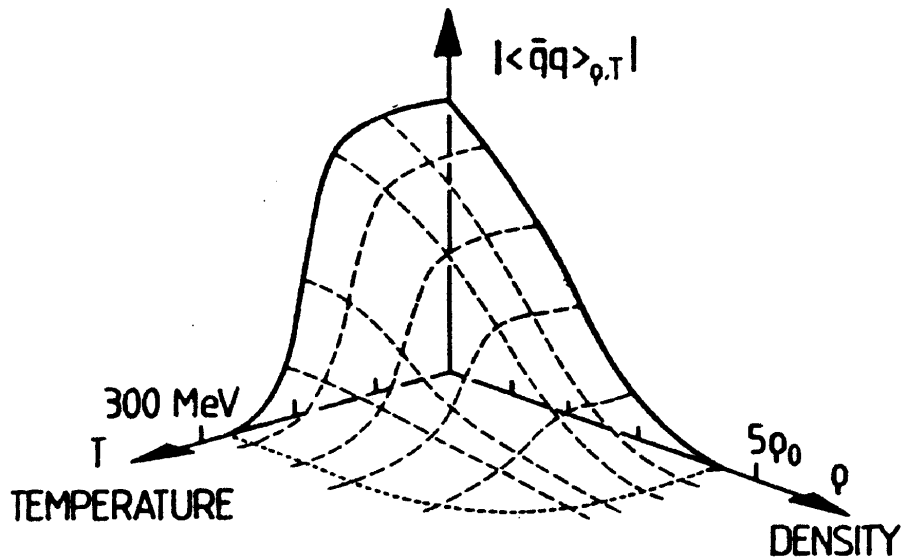


Figure 1.2: The $\langle q\bar{q} \rangle$ expectation value as a function of temperature and density of the strongly interacting system. (Figure taken from [9])

1.3 The Physics Goals of PHENIX

1.3.1 Physical Observables

Whereas the formation of a QGP is not directly observable by an experiment, the restoration of chiral symmetry directly affects masses, widths and branching ratios of mesons. These parameters are nevertheless also affected by other mechanisms. Thus both phenomena are difficult and not unambiguous to measure and all types of interaction products have to be investigated to obtain as much information about the development of the system as possi-

ble. Special emphasis has to be put on probes that do not interact strongly. These carry information about early stages of the development of the system which is not washed out by interaction with remnants of the collision at later times. Multiplicities and spectra of escaping hadrons, leptons, and photons carry a variety of signatures from all stages of the collision. A subtle change of a single observable is neither a convincing evidence for the occurrence of the expected phenomena nor sufficient to describe them. Therefore the PHENIX detectors have been designed to look for a variety of signals indicating QGP formation or chiral symmetry restoration. These include the reduced yield in the production of certain particle species (e.g. J/Ψ mesons) and the change in distributions of particle properties like their four momenta, their resonance widths, and their masses. A brief overview of some interesting signatures is given below. For a complete and detailed description and a review of the available data the reader is referred to [11].

J/Ψ Suppression

If the deconfinement phase transition occurs, the interaction potential of two partons in the QGP is “screened” by the presence of other quarks and gluons around them and thus the confining force between them is reduced. This can be understood as the QCD analogy to Debye screening which refers to the phenomenon that in nuclei with multiple electron shells the full nuclear charge is screened by the inner electrons and thus the outer shells only see a reduced nuclear charge. One consequence of this - already indicative in a previous experiment at the SPS [12] [5] - is that a charmed quark - antiquark

pair ($c\bar{c}$) can not form a bound state if the length scale on which this screening takes place is smaller than the binding radius of the pair. Therefore the production of charmonia, like the J/Ψ particle and its resonance Ψ' , is suppressed. A systematic investigation of J/Ψ suppression at high energies is one of the central parts in the PHENIX program.

Spectrum of Direct and Virtual Photons

Temperature and energy density in the interaction region are highest directly after the colliding nuclei have traversed each other. If the system is large and exists long enough to reach equilibrium it acts as a thermal radiation source. The spectrum of the emitted photons carries information about the initial temperature and thus the early stage of the collision. As photons do not interact strongly, they escape from the interaction zone undisturbed and reveal details of the thermal development of the system [11]. There are other sources of photons, mainly decays of produced particles (e.g. the main decay channel of the π^0 into a photon pair), which by far dominate the overall photon yield. These have to be known precisely and subtracted from the measured photon distributions, before the remaining direct spectrum can be used to investigate the thermal development of the collision. Whereas real photons escape from the interaction zone and reach the detectors, virtual photons decay into lepton pairs. The average transverse momentum $\langle p_t \rangle$ of these is also a measure of the temperature reached in the interaction. Investigating the dependency of $\langle p_t \rangle$ on the energy density of the hot system one can draw conclusions about the order of the phase transition. A first order transition

from confined hadrons to the QGP would go along with a jump in the number of degrees of freedom in the system. In that case a measurement of the system's temperature T as a function of the energy density ϵ should display a rise before the phase transition. A measure for the reached energy density is the overall number of particles produced in the collision. Once the critical point is reached, T should remain constant as ϵ continues to increase, until the phase transition is completed. After that the new degrees of freedom in the partonic system can be thermally excited and T should rise again [13].

Strangeness Enhancement

Because the amount of energy required for the production of strange mesons is higher than for mesons containing only u and d quarks one observes a strong suppression of strangeness production in proton-proton collisions [14]. In the case of the formation of a QGP with much higher energy density additional $s\bar{s}$ quark pairs can be produced by the interaction of two gluons. Therefore, one expects the number of strange particles to be enhanced in a QGP relative to a scenario with lower energy density in which only confined hadrons are present. A similar enhancement is expected for charm quarks.

Jet Quenching

In high-energy particle collisions pairs of particle jets leaving the vertex back to back have been observed. These are produced, when partons, quarks or gluons, scatter with high momentum transfer. As the partons separate, new particles are produced and form color neutral objects. The same happens

to subsequent generations of $q\bar{q}$ pairs and the decay products are registered as a jet of particles in the detector. If the system size is small, like in e^+e^- collisions, the jets do not interact with the matter in the interaction zone. In a QGP, however, the initial quark-antiquark pair has to travel through a region of dense matter. In this, it undergoes scattering with surrounding partons and loses energy. Therefore, the fastest or “leading” particles of the jet should be lower in energy compared to jet production in smaller systems. This phenomenon is known as “jet quenching” and is discussed as one signature of the QGP. [15] [16]

Decay Channels of the Φ

The mass of the Φ is just 33 MeV larger than twice the mass of the kaon and a distortion of the masses of these mesons, which is expected as one consequence of chiral symmetry restoration, is expected to alter the branching ratios between the hadronic decay $\Phi \rightarrow K^+K^-$ ($49.1 \pm 0.8\%$) and the leptonic decay $\Phi \rightarrow e^+e^-$ ($2.99 \pm 0.08 \times 10^{-4}\%$) [17]. Furthermore, a broadening of the invariant-mass spectrum of the Φ meson is expected. PHENIX therefore is going to measure the decay amplitudes and the distribution of the Φ mass with high accuracy to trace these effects.

1.3.2 Experimental Setup

The Goal of the PHENIX experiment is to measure simultaneously the phase-space distributions of leptons, photons and hadrons that leave the interaction region. Thereby particular emphasis is put on the spectroscopy of

lepton pairs as these carry many signatures of the phenomena one hopes to observe. To accomplish this task PHENIX is instrumented with 11 specialized detector subsystems and a magnet system. Several steps in the analysis of an event are necessary. First the event has to be characterized according to its centrality which is a measure of the energy density reached in the collision. The tracks of the particles leaving the interaction zone have to be reconstructed and the particles have to be identified. The calorimetry of emerging particles contributes both to the particle identification and to the global characterization of the collision. The separation of muons from pions for the lepton analysis requires that they traverse many hadronic interaction lengths in matter. Thus the muon detection system has to be separated in order not to distort the spectroscopy of electrons and hadrons. PHENIX is subdivided into two central spectrometer arms with a pseudorapidity coverage of $|\eta| < 0.35$ and an azimuthal coverage of $2 \times 90^\circ$ and two muon spectrometers covering the full rapidity and the full azimuthal distribution of all produced particles. The central arms measure photons, dielectrons and hadrons, whereas the muon arms are exclusively devoted to the measurement of muon properties. Figure 1.3 shows the different PHENIX subdetectors. A detailed discussion of the PHENIX experimental setup is given in [18]. How the different subsystems contribute to the analysis is briefly described in the following.

Event Characterization and Trigger Decision

To determine whether the detector systems have to be read out for a particular event, three PHENIX detectors perform the event characterization and

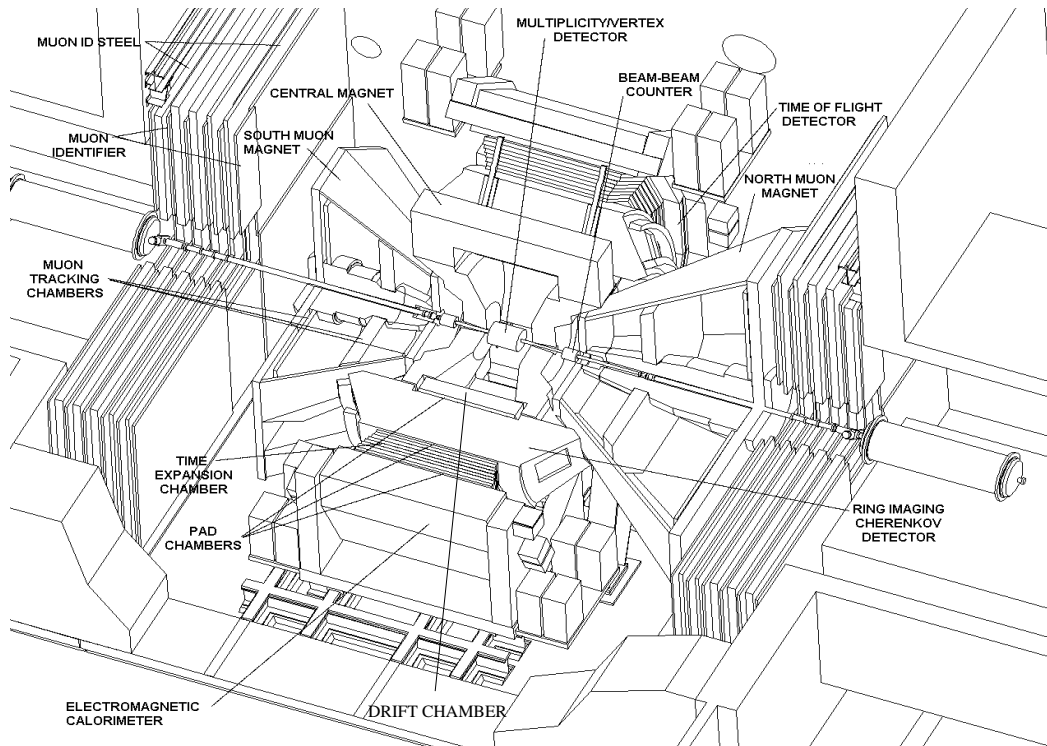


Figure 1.3: The PHENIX detector subsystems are separated into two pairs of arms: The *central arms* (here in front of and behind the beam axis) and the *muon arms* (here left and right of the vertex).

decide whether a readout is necessary or not. The Multiplicity Vertex Detector (MVD) consists of two concentric barrels of silicon strip detectors around the beam pipe and two end caps of silicon pad detectors. It uses the number of produced particles to characterize an event according to the energy density reached in the collision. The Beam-Beam Counter (BBC), composed of arrays of quartz Čerenkov detectors on either side of the vertex, the Zero Degree Calorimeter (ZDC) which measures energy deposition of neutral particles, and

the MVD trigger the data readout for the detector subsystems if the amount of deposited energy and the number of created particles indicate an event. Together the MVD and the BBC reconstruct the vertex position along the beam direction with an accuracy of approximately $100 - 200 \mu\text{m}$. They also set the reference time for the Time OF Flight detector (TOF).

Tracking in the Central Arms

To reconstruct the momentum of charged particles the PHENIX experimental setup is located in a magnetic field, which is created by three magnets. The central magnet is an axial field magnet, i.e. its field lines are almost parallel to the beam axis except for small deviations at the pole faces. It covers the rapidity interval of the central arm. Its pole faces serve as the primary absorber of hadrons for the Muon arm spectrometers. Muon magnets are mounted in front of the muon spectrometers. To measure momenta and invariant masses with high accuracy, particle tracks are reconstructed with information from the Drift Chambers (DC), Pad Chambers (PC) and the Time Expansion Chamber (TEC). The drift chamber is the most important detector for the track reconstruction. Its design is reviewed in detail in section 2.2. The PC is composed of three layers of pixel detectors that provide three dimensional space-point information for charged particle hits. It helps to resolve remaining ambiguities from the DC tracking and to separate hits from photons and other neutral particles from charged ones in the EMCal because the former do not have corresponding hits in the PC in front of the calorimeter. The TEC measures the differential energy loss of a traversing particle and reconstructs

tracks similar as the drift chamber from the drift times of the ionization products in a gas mixture. With the track reconstruction from these subsystems the resolution of the Φ meson mass in the e^+e^- channel is better than 0.5 % up to a transverse momentum of $2\text{ GeV}/c$. The transverse-momentum resolution $\Delta p_t/p_t$ of the track reconstruction is about $0.3\% \times p_t$ in the high momentum limit as shown in Figure 1.4.

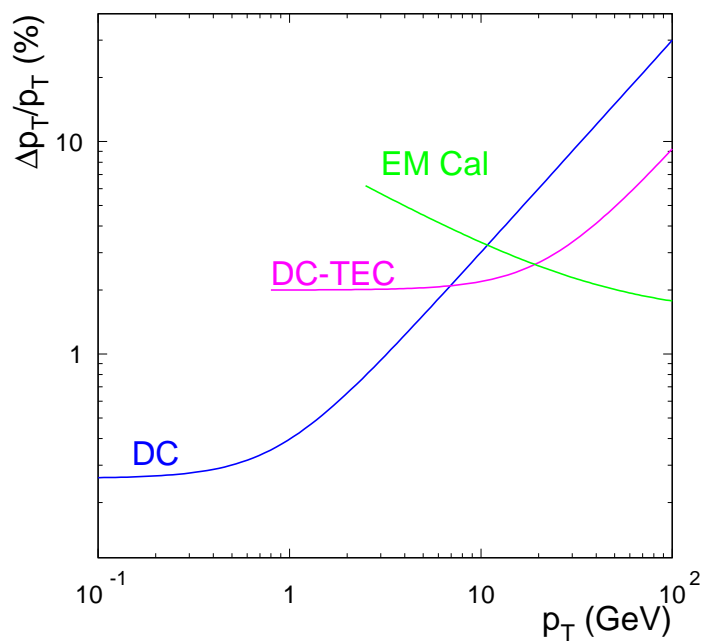


Figure 1.4: The transverse momentum resolution of the PHENIX tracking system as a function of p_t .

Muon Tracking

In the forward and backward rapidity region muon identification and tracking systems are installed, which consist of a magnet yoke and copper nose cones

as primary absorbers, strip tracking chambers, and five layers of streamer tubes alternating with iron absorbers. The muon magnets create a radially directed field in this region. They cover a rapidity interval of 1.1 to 2.4 units in the north and 1.1 to 2.2 units in the south. As in the central arms the pion contamination in the muon sample is expected to be below one part in 10^4 . The muon arms have a mass resolution of about 85 MeV for the J/Ψ in the $\mu^+\mu^-$ channel, which is modest compared to the central arm resolution for the $\mu^+\mu^-$ channel (18 MeV) but sufficient to separate the J/Ψ from the Ψ' resonance. Thus the two charmonium states can be investigated for relative suppression.

Particle Identification in the Central arm

The Ring Imaging Čerenkov Detector (RICH), the TEC and the Electromagnetic Calorimeter (EMCal) are used for the identification of charged particles. The RICH signal is read out via photo multiplier tubes. It is sensitive to the velocity of the particles. Electrons cross the Čerenkov threshold at lower momenta than pions which produce no signal at all up to a momentum of $\approx 4 \text{ GeV}/c$ and thus can be separated from them once the momentum of the particles has been reconstructed from the tracking detectors. The EMCal measures the deposition of energy by electromagnetic showers using two technologies: Lead scintillator arrays with a good timing resolution are combined with lead glass blocks to provide better energy measurements. The TEC distinguishes electrons from pions by the higher ionization power of the former for a given particle momentum. The PHENIX design goal is to reject pions in the electron sample by a factor of 10^4 .

Meson Separation in Particle Identification

To separate different mesons the EMCal and the Time Of Flight detector (TOF) are used. The lead scintillators of the EMCal can discriminate pions from kaons up to a momentum of approximately $1.4 \text{ GeV}/c$. The readout of the scintillators with photo diodes is too slow to use time differences of signals from faster particles for meson identification. The TOF covers only a small part of the azimuthal acceptance of the experiment. It consists of plastic scintillation counters with photo multiplier tube readout. The time resolution of 80 ps allows the separation of pions and kaons up to a momentum of $2.5 \text{ GeV}/c$.

Chapter 2

The PHENIX Drift Chamber Detectors

2.1 Operational Principles of Drift Chambers

2.1.1 Primary Ionization in the Working Gas

As elementary particles are not directly observable, one has to use their interaction with matter to identify them and to reconstruct their tracks. In drift chambers, the principle of interaction is the ionization of a gas mixture in the detector by charged particles and electromagnetic radiation. The mechanisms of ionization are well understood and a detailed review of them is given in [19]. The ionization power of the traversing charged particles is governed by the Bethe Bloch formula [20] given by:

$$-\frac{dE}{dx} = 4\pi N_A r_e^2 m_e c^2 z^2 \frac{Z}{A} \frac{1}{\beta^2} \left[\frac{1}{2} \ln \left(\frac{2m_e c^2 \beta^2 \gamma^2 T_{max}}{I^2} \right) - \beta^2 - \frac{\delta}{2} \right] \quad (2.1)$$

It describes what amount dE of kinetic energy of the particles is used to create electron-ion pairs along the differential track element dx . The symbols have the following meaning:

- N_A : Avogadro's number
- m_e, r_e : Electron mass and classical electron radius
- z : Charge number of the incident particle
- Z, A : Nuclear charge number and mass number of the gas
- βc : Velocity of the incident particle
- γ : Lorentz factor of the incident particle
- T_{max} : Maximum amount of kinetic energy that can be transferred from an ionizing particle to a hull electron of a molecule in the collision.
- I : Ionization constant of the material
- δ : Density modification due to the screening of the incident particle's electric field by the charge density of the hull electrons

The energy loss of the particle in matter is usually measured as a function of the product $\beta\gamma = p/m$, where p and m are the particle momentum and mass. The minimum of the ionization power and therefore the energy loss in matter corresponds to a value of $\beta\gamma \approx 3.5$. Therefore, one speaks of a minimum ionizing regime. The suppressing factor $1/\beta^2$ is compensated by the logarithmic term at higher energies. This behavior is called relativistic rise. In PHENIX, most particles traversing the drift chamber are minimum ionizing charged pions. Nevertheless, the primary ionization products of the

interaction between a traversing particle and gas molecules themselves carry enough energy to create additional pairs of electrons and ions.

2.1.2 Charge Drift and Amplification

The Drift Field

The sensitive region of a drift chamber consists of many anode or ‘sense’ wires in an electric drift field. The special feature of drift chambers is their ability to reconstruct the trajectory of a particle by using the time difference of its passing through the detector (the time of primary ionization) and the arrival of the charge signal on the anode wire. To obtain the position of the charge clouds origin, the free electrons created by the traversing particle and the secondary ionization are forced towards the anode wire of the drift cell by the drift field along defined drift trajectories. The drift lines of the charge clouds need to be known very accurate, to reconstruct positions in the drift cell. To adapt the field geometry to the specific needs of the experiment, one has to introduce not only anode and cathode wires in the detector, but also field shaping wires that allow to bend the field lines ¹ to the desired geometry. The choice of voltages on different wire types and the layout of drift cells allow to shape the drift lines so that isochrone surfaces in the detector are well determined. Together with a relation between distance and drift time, the shape of the isochrones is the basis for the position reconstruction. A detailed description of the drift cells, the drift-field geometry, and the purpose of the

¹(the field lines are the drift lines of the electric charge)

different wire types in the PHENIX drift chamber is given in chapter 2.2.

The Region of Constant Drift Velocity

In the largest part of the drift cells in the PHENIX drift chamber a homogeneous electric field is generated. In such a field a constant drift velocity v_{Drift} is reached once the loss of energy through collisions of the electrons with gas molecules is in equilibrium with the gain of energy in the drift field. A compact relation for v_{Drift} in homogeneous fields is given in [19]:

$$v_{drift} = \frac{e}{m_e} E \frac{kT}{p} \left\langle \frac{1}{\sigma(\epsilon)\nu(\epsilon)} \right\rangle \quad (2.2)$$

Here the symbols are:

- e, m : charge and mass of the electron
- T, p : Temperature and pressure of the gas
- E : Strength of the electric field
- ϵ : Total energy of the electron. (Sum of thermal energy $\frac{3}{2}kT$ and kinetic energy ϵ_{kin} due to acceleration in the field.)
- $\sigma(\epsilon)$: Overall cross section of momentum transfer between electrons and gas as a function of ϵ
- $\nu(\epsilon)$: Statistical velocity of the electrons

The drift velocity depends on the temperature, pressure, and composition of the gas. The ions created in the drift region are not used to reconstruct

positions. They drift opposite to the electrons with a much lower velocity and are neutralized when they reach the cathode wires. Equation 2.2 shows that v_{Drift} depends on the ratio E/p . To avoid large variations of the electron drift velocity due to changes in pressure or variations of the field one tries to tune the working point of the chamber in such a way, that a change in this ratio does not strongly affect v_{Drift} . Figure 2.1 shows the dependence of v_{Drift} on the ratio E/p for a gas mixture of Argon/Ethane at a ratio of 1:1 as it is used in the PHENIX drift chamber. The nominal working point of the PHENIX drift chamber is chosen on the relatively flat part of the function at $E/p \approx 3V/(cmTorr)$, to reduce nonlinearities in the relation between position and drift time and make the chamber less sensitive to variations of the gas pressure.

The Amplification or “Avalanche” Region

Closer to the anode wire, the electric field is becoming much stronger because the $1/r$ contribution from the cylindrical symmetric potential dominates. Thus, the electrons gain more energy than they lose by collisions, and can ionize more gas atoms. This effect is self amplifying and the number of electrons rises several orders of magnitude. The electrons travel to the wire and together with the drift of the positive ions create a signal on the sense wires if the amount of ionization is large enough to surpass the sensitivity threshold of the electronics. In the avalanche region, the ions are attracted by the potential wires. They contribute much more to the signal than the electrons do, because their motion is much slower and thus they induce mirror charges on the sense

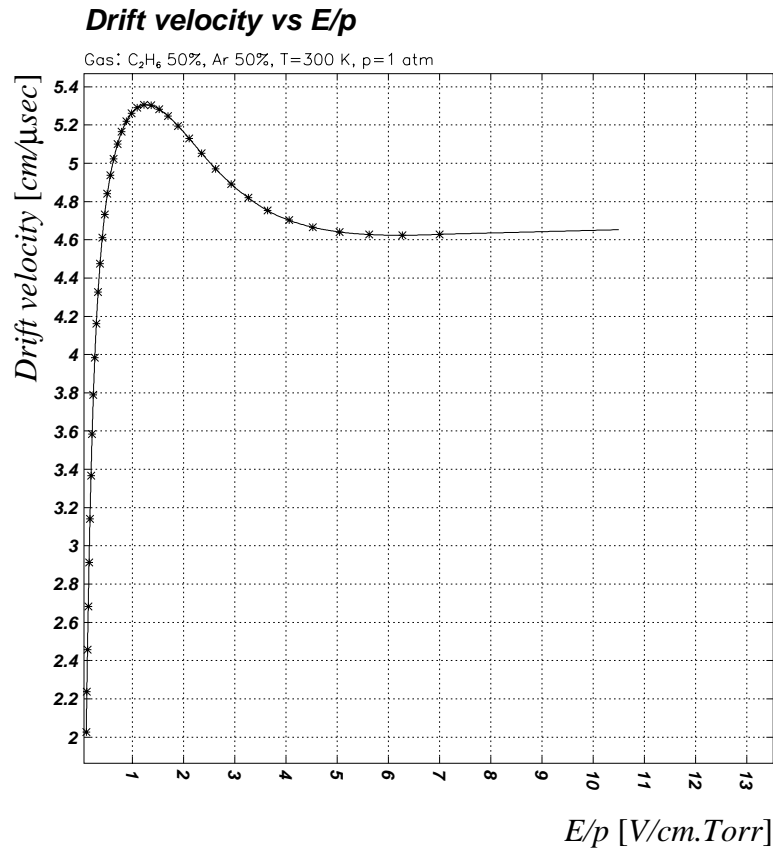


Figure 2.1: Drift velocity as a function of E/p in the PHENIX drift chamber working gas mixture. (Taken from GARFIELD calculations, tuned to the measurements of A. Vorobyov [21].

wires long after the electrons have been registered. The signal form on the sense wire is not trivial and, after its amplification, undergoes a shaping stage in the electronics before a time value can be determined from it.

In the avalanche region, the drift velocity is no longer exactly constant, but depends nontrivially on the specific field geometry and gas composition.

Therefore, nonlinear corrections to the relation between the distance of the charge cloud's origin from the wire and the time required for the electrons to reach the wire may be necessary. Chapter 4.2.2 describes how this space drift-time relation is obtained for the PHENIX drift chambers.

2.2 Design of the PHENIX Drift Chambers

2.2.1 Mechanical Construction

In the PHENIX experimental setup the two drift chambers cover the full acceptance of the two central arms. They extend from 2.03 to 2.47 meters in the radial direction. In azimuth, each arm covers an angle of 90° . The arms are set up in such a way that they display mirror symmetry with respect to a vertical plane containing the beam axis. The length of the drift chamber in beam direction (z) is 240 *cm*. In z , the chamber is centered around the vertex. In Φ , both arms are tilted upward by 11.25° with respect to the vertical axis to match the azimuthal coverage of the experiment. Figure 1.3 shows the position of the drift chamber in the experimental setup and Fig. 2.2 illustrates the shape and the dimensions of a drift chamber frame. The frame is made of titanium. This material has two advantages. It provides good mechanical stability, whereas its small nuclear charge number reduces the rate of secondary particle production. These particles contribute to the signal registered by the chamber and by other detectors and thus have to be suppressed as much as possible. To avoid a deformation of the frame due to the wire tension, it is supported by a carbon fiber strut parallel to the beam axis in the center of each

arm. The chambers are azimuthally subdivided into 20 so called keystones, each of which covers 4.5° in Φ . Each keystone holds six wire cages of different types (see below) with growing radial distance from the beam axis.

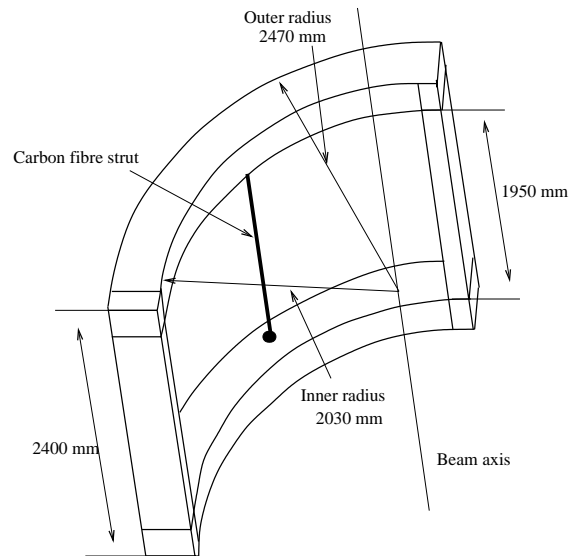


Figure 2.2: Schematic drawing of the PHENIX drift chamber frame.

2.2.2 Drift Cell Design

Wire Arrangement

There are six different types of wire cages in the drift chamber. They are labeled according to the type of anode wire they carry (with growing radial distance from the center): $X1, U1, V1, X2, U2, V2$ as shown in Fig. 2.3. All X wires run along the z - direction. Therefore, using only the X wire information one can reconstruct a two dimensional projection of a track in the $x - y$ plane. To obtain z - information, the U and V wires are tilted at an angle of $\approx \pm 4.5^\circ$

with respect to the z - direction. They begin in one keystone on one side of the chamber, but end in the neighboring keystone on the other side. Thus the tilt angle increases with R . This arrangement allows a stereo picture of a particle track. How the three dimensional track is reconstructed from the stereo information is described in chapter 5. In Φ , each cage is subdivided into four sense-wire layers. Each layer contains 12 $X1$ and $X2$ and 4 $U1, U2, V1$, and $V2$ wires. Figure 2.3 displays the wire arrangement for all 40 wires along the radial direction. One keystone consists of four such arrangements that are adjacent to each other and are mutually shifted by 1.125 degrees in Φ .

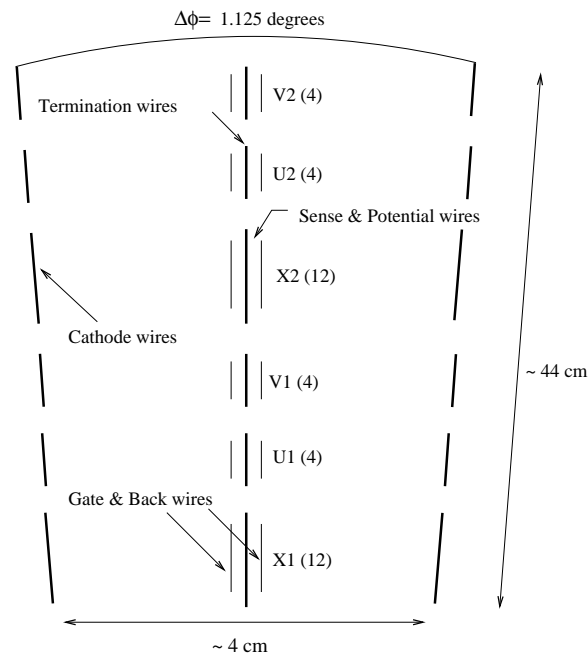


Figure 2.3: The arrangement of wires along the radial coordinate of the chamber. One layer with the six different wire cages is shown

A drift cell is approximately 4 centimeters wide in azimuthal direction and 6 mm high in radial direction. The maximum drift length in a drift cell is therefore roughly 2 cm. Due to the increasing radial distance the outer wires have a slightly larger maximum drift length. Figure 2.4 shows the geometry of the wires within one cell. Besides the sense wires, a drift cell also contains cathode wire planes and four other types of wires whose purpose is to shape the electric field. The *back drift wires* are mounted alternating with *gate wire* pairs at an azimuthal distance of 2 mm from the anode wires. The region between the gate and back wire planes is from now on referred to as the back-drift region. The wire arrangement makes the drift cell fully efficient within the back-drift region to both sides and inefficient beyond that region on the back-wire side. The charge coming from the inefficient region is collected on the back wire. Thereby a left-right ambiguity in the hit reconstruction is avoided.

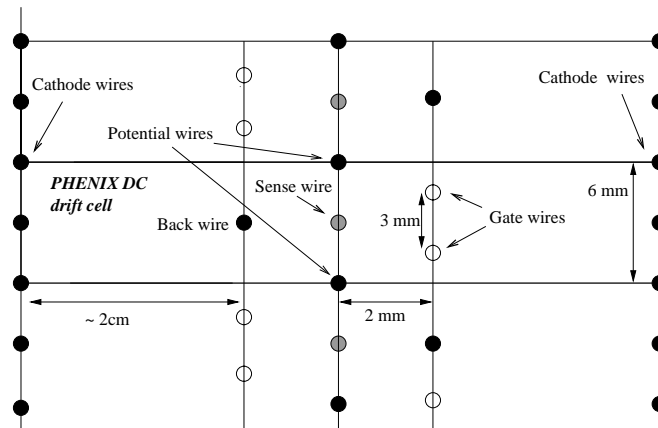


Figure 2.4: Mutual wire positions in a drift cell

In the back-drift region, the drift field is nonlinear close to the anode wires. Here the amplification of charge clouds, described above, takes place. The purpose of the *potential wires* is to shape the field such that the charge passing the gate is amplified and collected on the corresponding anode wire. On the top and bottom of each cage's anode wire plane *termination wires* are mounted to provide a clean border of the field lines within the cage. In table 2.1 the materials, diameters, and a range of possible operating voltages of the different wire types are given.

Wire type	diameter [μm]	material	Operating potential [V]
Sense (Anode)	25	W (Au layered)	$U_A = 0$
Gate	90	Cu (Be layered)	$U_G = -1500$ to -1600
Potential	90	Cu (Be layered)	$U_P = -2300$ to -2650
Back drift	90	Cu (Be layered)	$U_B = -800$ to -900
Cathode	90	Cu (Be layered)	$U_C = -4000$ to -4700

Table 2.1: Wire characteristics in the drift chamber

Field Geometry in the Drift Cells

The field geometry in the drift cells is determined by the wire geometry and the voltages the wires are supplied with. Simulations with the wire-chamber

simulation package GARFIELD [22] have been used to determine an optimized voltage configuration for the PHENIX drift chamber. The goal thereby is to obtain a large single-wire efficiency and to optimize the gas gain for all anode wires. Fig. 2.5 shows the drift lines that end on the sense wire and the isochrones along these drift lines in one drift cell for a typical voltage setting. In Fig. 2.6 the contours of the corresponding equipotential surfaces in the drift cell are displayed.

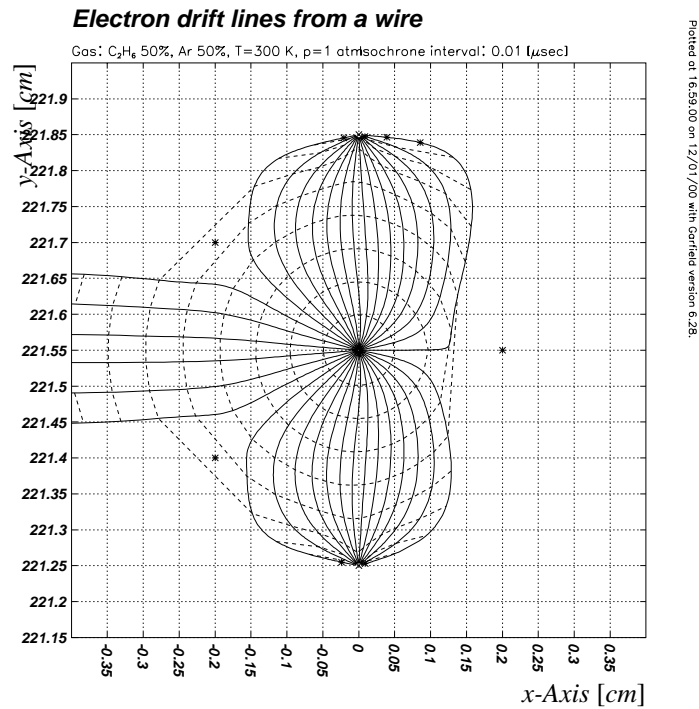


Figure 2.5: The drift lines and isochrones in the drift cell of a stereo wire with voltage settings:

$$U_B = -900V, U_P = -2650V, U_C = -4500V, U_G = -1560V, U_A = 0V$$

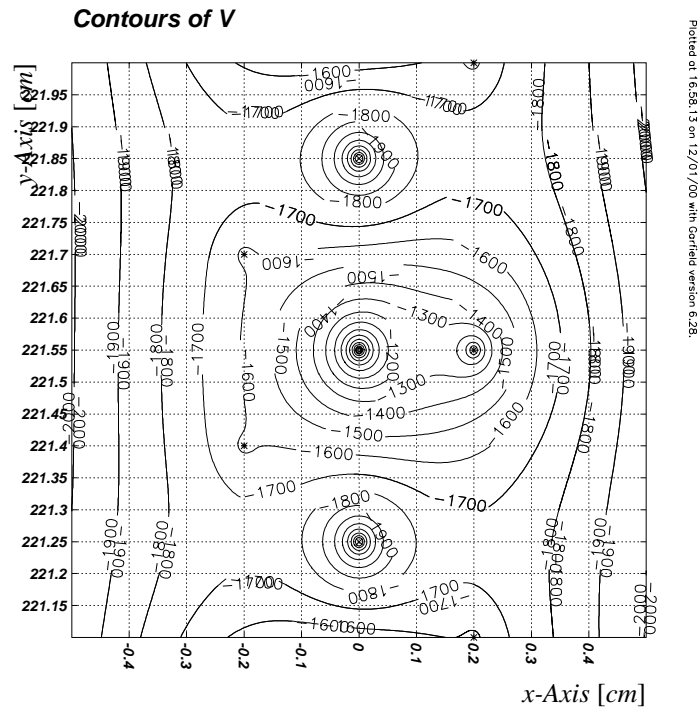


Figure 2.6: The equipotential lines in the PHENIX drift cell. The voltages are the same as given in Fig. 2.5

The charge drift lines from one side of the cell are shielded by the back-drift wire. The isochrones are equidistant along the x axis. One therefore expects a linear relation between position along the x axis and drift time. Due to the bending of the field lines between the back and the sense wire plane not the whole back-drift region is sensitive to both sides. The resulting drift-time distribution and the reconstruction of the space drift-time relation will be discussed in chapter 4.2.2.

The Working Gas Mixture

In the PHENIX drift chamber a mixture of Argon (50%) and Ethane (50%) is used as working gas. With the field configuration described above, the maximum drift time in the chamber is approximately 450 ns , whereas the electronics can digitize drift times up to 630 ns . This guarantees that all signals from all drift cells fall into the readout interval belonging to one event. The choice of the gas mixture allows to operate the chamber in the so called ‘region of saturated drift velocity’, where small changes in the ratio E/p only weakly affect the drift velocity as shown in Fig. 2.1. The quenching gas Ethane has many oscillation modes which can be excited by drifting electrons. Due to the energy loss in the interaction with the ethane molecules the electrons get shifted towards the minimum of the cross section of momentum transfer which accelerates their drift. The high drift velocity of $\approx 5\text{ cm}/\mu\text{s}$ in turn requires a good time resolution of the readout electronics to achieve adequate position reconstruction. The purity of the chamber gas is monitored and maintained by a purging device in the gas system.

2.3 Data Readout and Data Handling in PHENIX

2.3.1 Trigger for Data Readout

All PHENIX detector systems are connected via timing to the RHIC clock which provides a common reference frequency of 38 MHz to the subsystems. When a trigger decision is made, the data from all subsystems are assembled for

the respective event and are written to tape. The trigger decision in PHENIX is based upon multiplicity measurements in the MVD and the response in the calorimeter and the BBC. The drift chamber can not contribute to the trigger, as its reconstruction time is too long to make a decision immediately. Recorded data are stored in a local buffer in the drift chamber electronics for a certain time, so that after a positive trigger decision they can be read out from the memory that corresponds to the event to be recorded. The trigger is supplied to the drift chamber electronics via an optical fiber called “GLink” (*Gigabyte Link*). The GLink also supplies the clock and the readout command to the electronics.

2.3.2 Front End Electronics

The front end electronics handles the digitization of signals, the temporary storage of the data in a buffer, and the transmission to the data acquisition system if a trigger is supplied. Figure 2.7 shows a scheme of the most important electronics components. Each keystone contains four ASD/TMC boards. The ASD (*Amplifier Shaper Discriminator*) chips are connected to the sense wires of the chamber. They receive and amplify pulses from the wires and according to a predetermined calibration they decide, whether the pulse is above a certain signal threshold. If so, a TMC (*Time Memory Cell*) digitizes the times at which the pulse surpassed that threshold value and at which it falls below it. The width of the TMC time bins is 0.82 ns at a clock frequency of 38 MHz. As there is no immediate decision whether a piece of data is used or not the TMC holds an amount of data in memory that corresponds to a time interval of $6.4\ \mu\text{s}$.

Older data are overwritten with newer ones when no trigger demands readout.

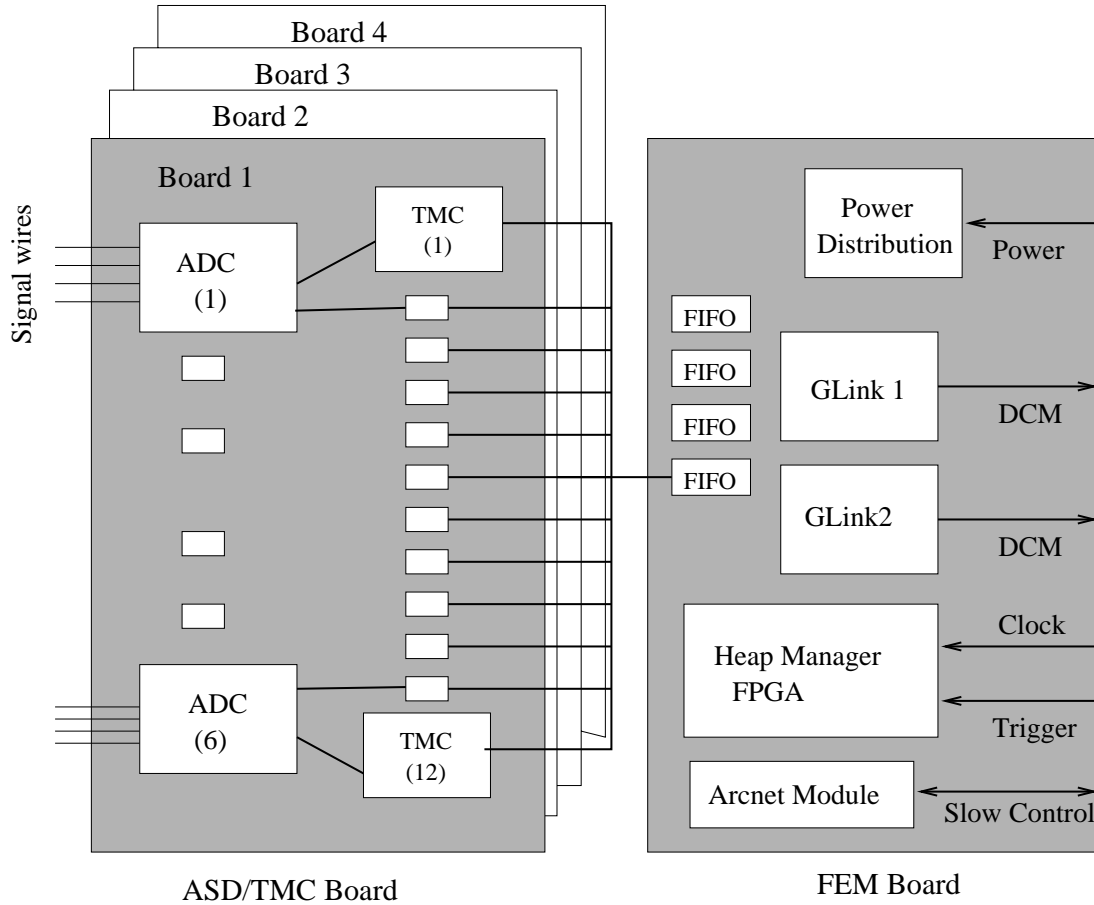


Figure 2.7: Schematics of the PHENIX front end electronics

If a trigger is received, the starting point of the readout in memory has to be chosen such that it compensates for signal traveling and trigger decision time. From the starting point, a time interval of 630 ns is read out once the respective signals are given by the timing module via the GLink. One drift chamber FEM (*Front End Module*) is in charge of the data traffic of four ASD/TMC boards. The FEM carries the GLink modules for trigger and clock

signals and for serial data output. It provides a connection to the slow control system via a microcontroller card. The data management is done by the Heap Manager, which consists of two FPGAs (*Field Programmable Gate Arrays*) whose program can be stored on the FEM. It buffers and formats the data from the TMCs into packets before it supplies them to the Data Collection Modules (DCM) via GLink. The DCM enlarges the data words to classify them according to their origin in the drift chamber. The format they have then is referred to as PHENIX Raw Data Format (PRDF). It is the input format of the data to the online/offline analysis chain and is discussed in chapter 4.1. After the packets are processed by the DCM they are combined with data packets of other detectors in the Event Builder and are written to tape.

Chapter 3

Calibration Software Structure

3.1 The Data Analysis Framework

3.1.1 Data Stream to the Monitoring Processes

The monitoring algorithms analyze one event at a time. These are read in form of event packages assembled by the detector electronics. Event packages for analysis can be retrieved one by one upon demand from a data pool or from a file. For this purpose, interface classes are provided in the PHENIX online/offline environment. The so called event iterators open a queue to an event source that can be specified by the user and deliver events to a particular process upon request. The event demand usually happens within a loop. Figure 3.1 schematically shows the data flow from the event builder (online), or from a disk or tape-robot file (offline) to the analysis chain. The Data-Distribution pool shown in Fig. 3.1a is a buffer between the event source and the analysis processes. It is used if several processes need access to the same data source at the same time. It manages the data traffic and makes

sure that different processes do not slow down or even halt one another. Data-Distribution pools can be used both for offline analysis of recorded events and for online event delivery e.g. to monitoring routines. They hide the source from the process that pulls events out of the pool. To analyze a single file it is also possible to attach an event iterator directly to it, without piping the data through a data pool (See Fig. 3.1b).

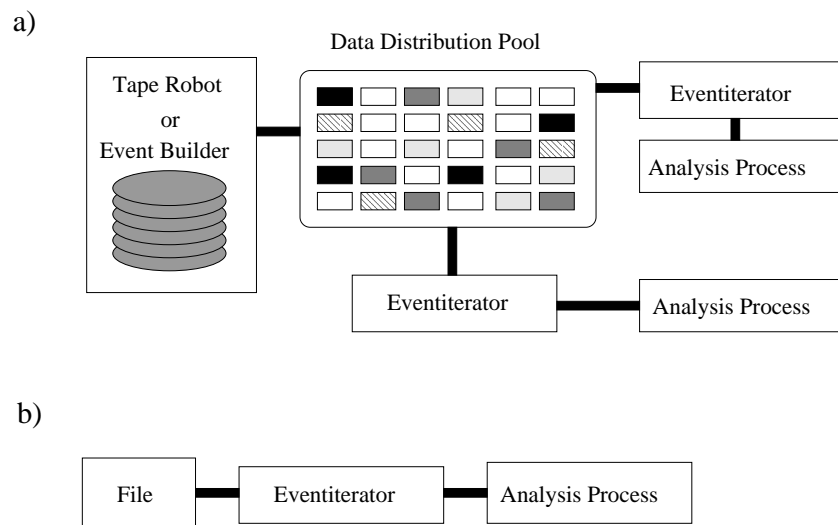


Figure 3.1: Schematic picture of the data flow from data storage or acquisition systems to the analysis modules.

The DD-Pool in a) is used when several processes want to use the same source of data.

In b) the flow for a single process reading from a source is illustrated.

3.1.2 Data Management with PHOOL

After the data have been retrieved from the iterator, they need to be kept in well defined locations in memory for unpacking and reconstruction. In PHENIX, a container structure for the data objects has been designed. It is named PHOOL (*PHENIX Object Oriented Library*) and is coded in C++. It provides a tree structure for proper storage of all subsystem data objects in PHENIX. Basic classes are contained for the design of individual analysis packages. Navigation methods for searching and retrieving data in the tree are implemented and convenient methods for resetting and restructuring the tree exist. The invocation of analysis modules like the DC unpacking, calibration, and tracking packages is standardized and the details of their operation are hidden from the user. The modules are written to find their input data and to operate on them by themselves and to add new branches to the tree with their respective output. This guarantees that all subsystems can run the complete analysis chain, without having to know about the way data input and output is handled by software packages of other subdetectors.

3.1.3 Data Visualization with ROOT

After the data have gone through different stages of analysis, as described in chapter 4 and 5.1, and have automatically been stored in the PHOOL tree, they can be sorted and searched according to different criteria and can be used to determine the performance parameters described in chapter 5.2. This is the essential task of online-monitoring processes. The information contained in

the data is to be extracted and displayed in a convenient form. Specialized graphics software packages for the purpose of data visualization in particle-physics experiments have been developed for a long time. PHENIX uses ROOT as offline and online graphics environment. ROOT is an object oriented data acquisition and analysis application, which was developed at CERN and is written mainly in C++. A detailed introduction to the ROOT framework is given on the CERN web pages [23]. It provides histogram, graphics, and ntuple classes with a variety of display modes as well as versatile tools to fit and evaluate functions. User interface classes allow the customization of applications and the control of analysis processes. ROOT has many additional features that allow to use it for the simulation of experimental setups and it also includes generator packages for physics simulations. Event handling and data acquisition are also among its capabilities. In PHENIX, ROOT is used for offline data visualization, for event display purposes, and for online monitoring of detector subsystems.

3.2 Calibration and Monitoring Software

3.2.1 Concept and Environment

The drift chamber software package DOOM (Drift chamber Object Oriented Monitor) is coded in C++ and is written to be run on the CINT (*C++ Interpreter*) interpreter which is part of the ROOT analysis framework. On the CINT prompt, C++ commands can be executed one at a time or in groups in form of macros. To speed up the analysis, compiled code can be loaded into

the interpreter environment via shared object libraries. The calibration software for the analysis of the cosmic-ray data consists of several macros which at runtime load compiled analysis code and instantiate the monitoring objects. The macros then call member functions of the monitoring classes to set up the environment for a particular process and analyze events one-by-one in a loop.

3.2.2 Calibration Code Library

A main calibration library has been created which after compilation is linked to appropriate libraries containing information about the PHOOL environment, the unpacking, calibration, and tracking code and the iterator and event classes of PHENIX. The calibration classes themselves are compiled in a way that allows to instantiate the objects on the CINT interpreter and to call their member functions from the command line. The classes are written to perform the calibration tasks described in chapters 4.2.2 and 5.2. Their interactive use is limited in so far as no multithreading capability exists yet. This means that as long as the iterator feeds data to a monitor in a loop without explicit break points, there is no possibility to interfere with the process, e.g. to call a display or reset function. A multithreaded version of ROOT that allows truly interactive data display and flexible handling of processes is under development at BNL. The parameter extraction from cosmic-ray data has been performed by analyzing a given number of events and then handing control back to the user. Adaptions to the monitoring classes have to be implemented, once a multithreaded interpreter environment exists. The class library for the monitoring objects and the classes therein are explained in Appendix A.

Chapter 4

Processing of Raw Data

4.1 Unpacking the Data Stream

The aim of the drift chamber analysis chain is to reconstruct tracks of charged particles. As the digital data created by the electronics from the analog signal can not be used directly for that, they need to be unpacked and translated into useful physical information. The format of the bit pattern in which hits in the drift chamber are encoded is described here briefly.

During the readout of one event each TMC chip delivers twenty four data words sequentially for each of its channels. Subsequent time intervals of 26.4 ns each are represented by subsequent 10-bit data words corresponding to the signals recorded on one individual anode wire in the interval. A word is subdivided into two 5-bit blocks. Each block can hold one time value for a leading edge or for a trailing edge of a signal. If the most significant bit of a block is set to 1 the block contains the time of a leading edge which is encoded in the remaining 4 bits. Trailing edges are identified by 0 and 1 in the two most

significant bits of a block and consequently their time is digitized with 3-bit resolution only. In total, the 24 data words per channel cover a time interval of $24 \times 26.4 = 633.6 \text{ ns}$ and may contain up to 48 leading or trailing edges of signals recorded on one wire. The heap manager on the FEM puts data from 2 TMC boards (80 channels) into one data packet and adds several header and trailer words before it sends the data to the DCM. In the header, the detector identification, the event number, the FEM address, and the clock counter of the trigger signal are encoded. The trailing words contain information about eventual error flags generated by the electronics and a parity word created from the packet data to ensure the integrity. The DCM adds twelve bits of higher significance to each word to identify it according to its type (header, trailer or data word) and its corresponding channel in the chamber. The drift chamber unpacking routine reads the data words and extracts the information stored in the bit pattern. The output is a list of drift times that are stored together with the information about the sense wire they come from.

4.2 Calibration of Hits in the Drift Chamber

4.2.1 Trajectories of Charge Clouds

Drift-chamber tracks are reconstructed from three-dimensional information about the points at which free electrons were created by traversing particles. The times of the leading and trailing edges of signal pulses thus have to be converted into spatial information about the position of primary ionization. This task is accomplished by a calibration module which is part of the DC

reconstruction code. As input the module needs information about the drift lines along which a cloud of electrons moves and a space drift-time relation (SDTR) to reconstruct the hits.

Drift Lines of X and Stereo Wires

The drifting charge follows the field lines of the electric field. Far away from the avalanche region and from the cathode wires the electrons drift in a uniform field directed from the sense wire plane to the cathode plane. For the X wires the geometry is easily visualized. Figures 4.1a and b project the wire planes and the drift direction into the transverse plane. It is clear that for the stereo wires a unique drift direction can not be identified, because the end points of the wires have different Φ coordinates. The drift direction changes linearly with the z -coordinate between its values at the wire end points.

As the charge collected on a sense wire comes from primary ionization points along a finite track element which have different distances from the wire it has a finite width. The drifting charge is also subject to diffusion along the drift lines. Therefore the signal on the wire has a finite width. In the hit calibration, the time at which the signal pulse first crosses the threshold set in the electronics is used as an input to the algorithm for position reconstruction. In that algorithm, the charge cloud is assumed to have passed the point centered between the gate wires when the space drift-time relation is used to reconstruct its origin. In the back-drift region, the direction of the charge cloud's motion is taken to be the same as in the drift region as shown in Fig. 4.1a. This assumption is a strong simplification for hits inside the back-

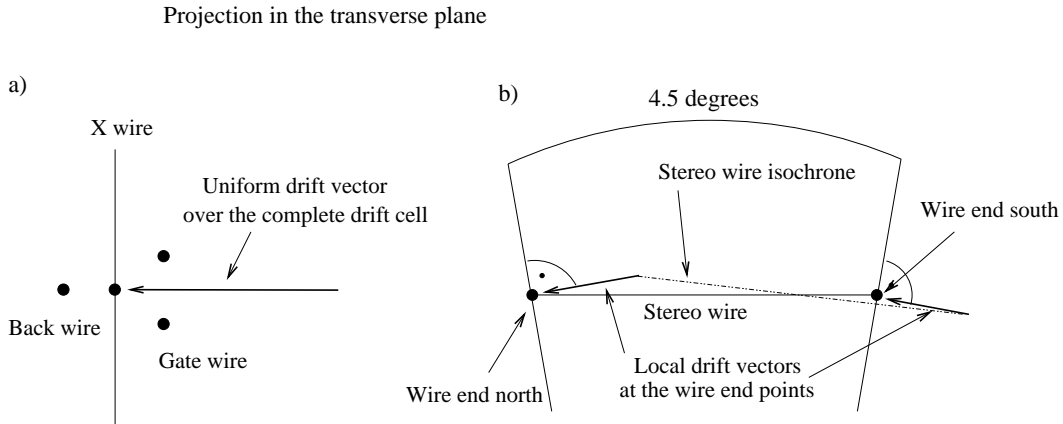


Figure 4.1: Figure a) illustrates the drift direction for the X wires. It is constant in the whole drift cell. From Figure b) one sees that the drift direction varies for the stereo wires from the north to the south end of the chamber. The wire, the isochrone and the drift vectors at the end points are projected into the transverse plane. For reconstruction purposes the drift direction of a charge cloud *at a particular z-coordinate* is assumed to be the same throughout the entire drift cell.

drift region as the drift lines there are not perpendicular to the sense wire plane any longer (see Fig. 2.5). Nevertheless this simplification is necessary as otherwise hits become ambiguous because a priori the inclination of the track is not known. Thus, the exact position at which the tracks touched an isochrone can not be determined. As a consequence of these assumptions, all reconstructed points of primary ionization with a fixed drift time to a particular X wire lie on a line parallel to the wire. The stereo-wire isochrones, in principle, are not straight lines. Nevertheless, for all practical purposes they

can be approximated by straight lines whose end points lie on the connecting lines between sense and cathode wire end points. They are therefore not parallel to the sense wires!

4.2.2 Reconstruction of the Space Drift-Time Relation

The side from which a charge cloud drifts towards a sense wire and the drift direction are known from the geometry of the wire arrangement. Therefore a signal can be identified with a straight line in three dimensional space at a distance from the wire that corresponds uniquely to the time at which it was received. The input to this mapping is the space drift-time relation. The determination of the space drift-time relation and its parameterization is one of the tasks of the calibration stage. The parameters need to be monitored and updated in the PHENIX calibration database in regular intervals for offline reconstruction of events and for the use in other monitoring routines. The software for this is described in chapter 3.2 and in appendix A.

Theoretical Predictions from GARFIELD

The drift-chamber simulation program GARFIELD was used to estimate the functional form of the space drift-time relation in the PHENIX drift chamber. The input parameters to the simulation were chosen in accordance with the nominal operating voltages and the gas mixture of the chamber. The shape of the space drift-time relation which is the Garfield output is the basis of the estimate. Garfield calculates the arrival time of the signal on the wire for charge clouds originating from a track that crosses the x axis at a given

distance at a given angle as illustrated in Fig. 4.2. It then associates the x coordinate of this intersection with the computed minimum drift time. In other words, the first charge clouds to reach the sense wire define the *drift time* while the *drift length* is defined by the x coordinate at which the track crosses the x axis in Fig 4.2.

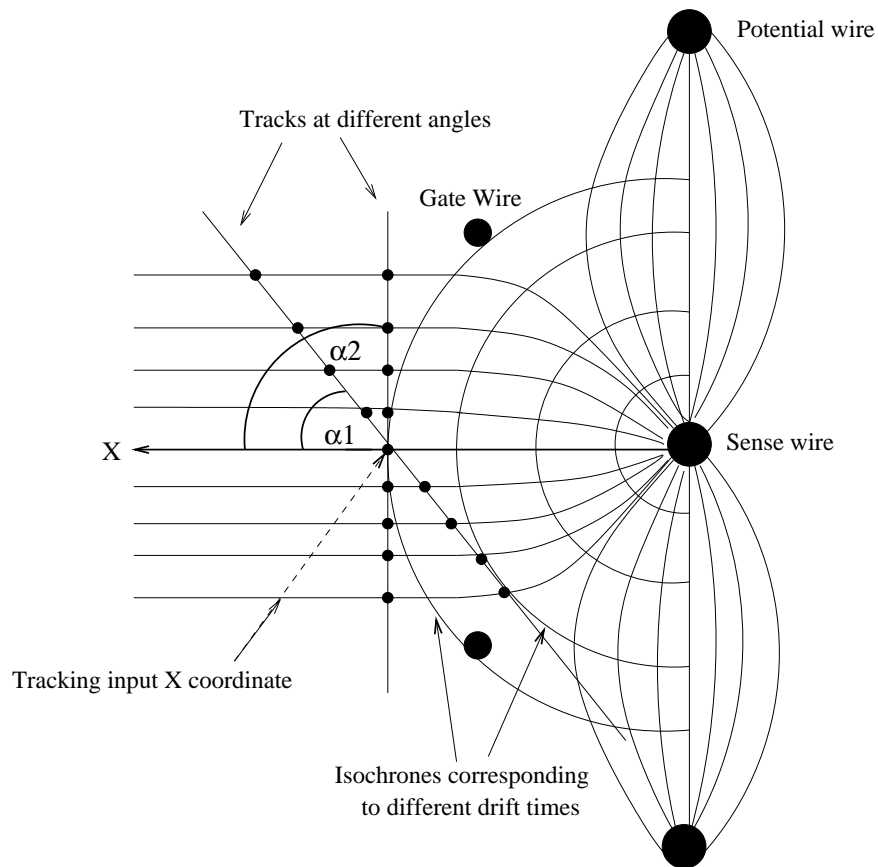


Figure 4.2: Tracks crossing the x axis at the same x-coordinate at different inclination angles α .

In Fig. 4.3 the resulting dependence of drift-time and x coordinate is plotted for tracks passing a sense wire at an angle of 70° . The voltages on the wires

are chosen to match the setting in the cosmic-ray test with the best available statistics.

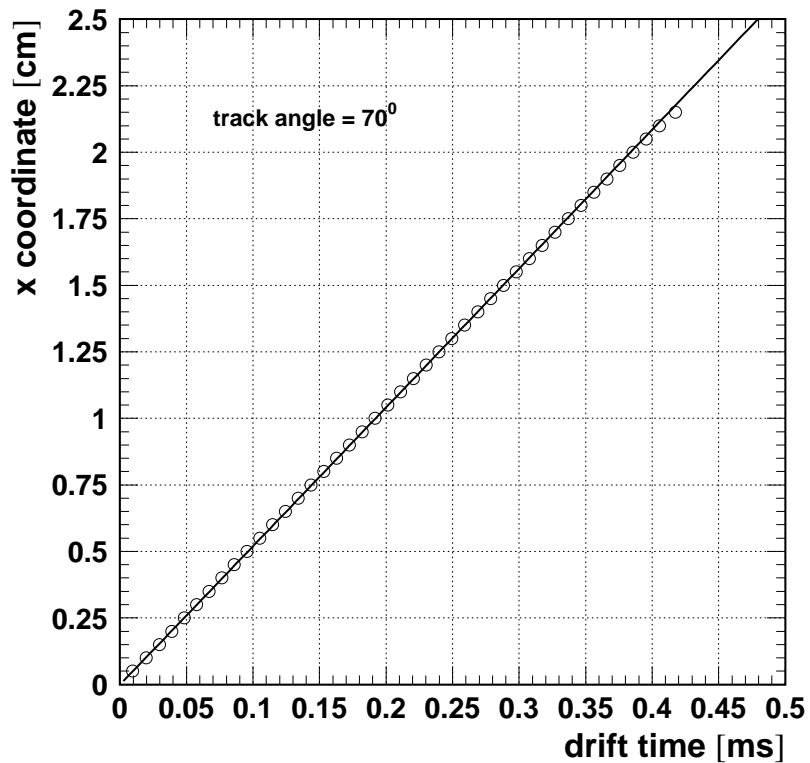


Figure 4.3: Space drift time relation for tracks crossing the x axis at an angle of 70°

Voltages: $U_{cath} = 4700V$, $U_{back} = 900V$, $U_{pot} = 2300V$, $U_{gate} = 1550V$

The datasets are fitted to a model function that assumes a contribution linear in the drift time and a contribution proportional to the square root of the drift time.

$$x = p_1 \times t + p_2 \times \sqrt{t} \quad (4.1)$$

For angles that are larger than 70° with respect to the x axis negative coefficients p_2 are calculated. At smaller angles p_2 becomes positive. For angles smaller than 60° GARFIELD fails to calculate the optimum drift lines and predictions are therefore not attempted. The minimum angle of traversing particles in the drift chamber is expected to be 45° . The mean angle is roughly 70° . For this angle the nonlinear contribution to the space drift-time relation becomes minimal. The values obtained for p_1 and p_2 are summarized in table 4.1. The maximum contribution to the drift length of the non-linear part at both 90° and at 60° is $\approx 500\mu m$ at large drift lengths which is more than three times the nominal drift chamber resolution. If one applies a linear space drift-time relation as a first approximation in the calibration procedure, one has to keep this deviation in mind and should not expect to reach the design resolution.

Experimental Determination of the SDTR from the Drift-Time Spectrum

A first estimate of the space drift-time relation for tracks that pass the chamber can be obtained by an integration of the drift-time spectrum as described in the following. The method was tested with Monte-Carlo data and was also used for the data from the cosmic-ray test. The assumptions that are necessary for it's validity are described in the following:

- Larger drift times correspond to larger drift distances. The space drift-time relation is monotonously rising. A distance of zero from the wire

angle	$p_1[cm/ms]$	$p_2[cm/\sqrt{ms}]$
90°	5.411	-0.168
80°	5.358	-0.125
70°	5.232	-0.013
60°	5.044	0.142

Table 4.1: Linear (p_1) and non-linear (p_2) coefficients of the space drift-time relation according to equation 4.1.

corresponds to drift time zero. The longest measured drift times correspond to the maximum drift length within a cell.

- The acceptance of the detector and the illumination with tracks is uniform in Φ over the complete drift cell. These assumptions are made in the generation of Monte Carlo data and should also be true for real data when edge effects in the trigger setup are excluded from the analysis.
- As the detector is not efficient in the drift region on one side, the number of hits registered inside the back-drift region is twice as high as outside. For this assumption to be valid, the back wires need to provide good shielding of the sense wires (See chapter 5.2.1).
- The arrival time corresponds to the drift length of charge clouds that

drifted along the x axis. This means that the measured distance can be directly used as input to the tracking algorithm. This assumption is valid in good approximation only if the drift lines are parallel to the x axis. Therefore deviations for tracks passing the back-drift region are expected.

Assumptions 2 and 3 together suggest a spatial reference distribution of hits dN/dx along the drift direction as shown in Fig. 4.4. As the maximum drift length increases within one cage from the inner to the outer wires, one needs to correct the reference distribution for this effect if one wants to determine the space drift-time relation for all wires of one type together. The resulting dN/dx has a step like structure at the end, because less wires contribute at larger drift lengths. Given the reference distribution dN/dx and a measured distribution of drift times dN/dt , one can integrate both from zero up to equal fractions f of their overall area. If the space drift-time relation shows monotonous behavior, hits that fall into this fraction f of the integrated spatial hit density also must fall into the same fraction f of the integrated drift time spectrum. Figure 4.4 illustrates the mapping of x coordinate and drift time.

The values of x and t which correspond to the same fractions of the normalized total integrals of dN/dx and dN/dt respectively, define the functional dependence $x(t)$ between the hit distance from the wire and the drift time. The results of the algorithm outlined here when applied to Monte Carlo data and to cosmic-ray data are presented in the following sections.

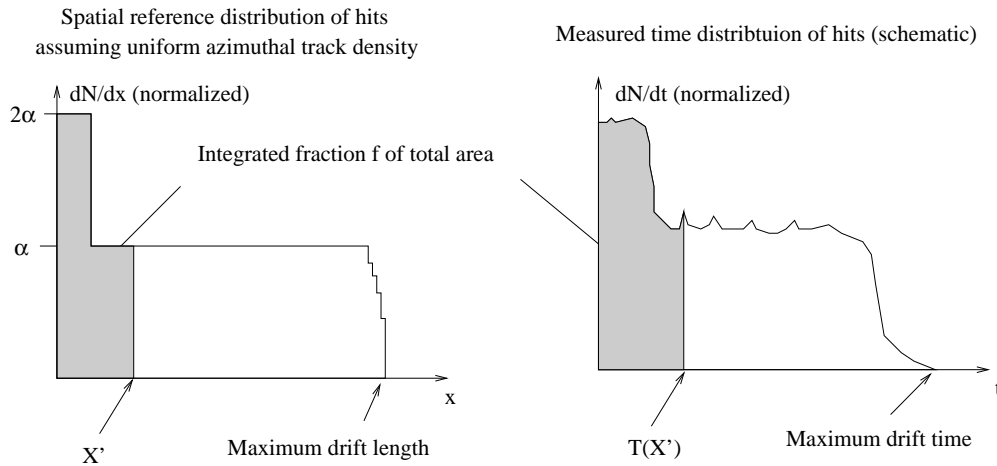


Figure 4.4: The spatial reference distribution (shown left) and the measured drift-time distribution (shown right) are integrated up to equal fractions of their total area. The points X' and $T(X')$ at which the integrals have the same fraction f of the total area correspond to a point on the function describing the space drift-time relation.

4.2.3 Space Drift-Time Relation for Monte Carlo Data Generation of Data

The PHENIX Monte Carlo software PISA (PHENIX Integrated Simulation Application) propagates the particles “created” by physics event generators through the different detectors. It determines which sensitive region in a subsystem is hit by a particle and simulates the detector response. The resulting signals are coded in the same format as the output of the data acquisition system used in the experiment. Thus the offline reconstruction software and the online monitor can be checked with simulated data where the results to be

expected are known beforehand. The drift chamber response to a traversing particle is generated in the following way:

The simulation software determines all drift cells crossed by a charged particle and checks whether the sense wire was supposed to see or ignore the hit, depending on the orientation of gate and back wires. It then calculates the entry and exit x coordinates of the track in the drift cell and uses the mean value for evaluating the drift distance. The process is illustrated in Fig. 4.5. The drift direction is assumed to be uniform over the whole drift cell and a constant drift velocity is used. From the x coordinate the drift time is computed and is added to the raw data information together with the cell coordinates. PISA also simulates the signal width distribution, multiple scattering of charged particles, and it can be run with a defined single-wire efficiency.

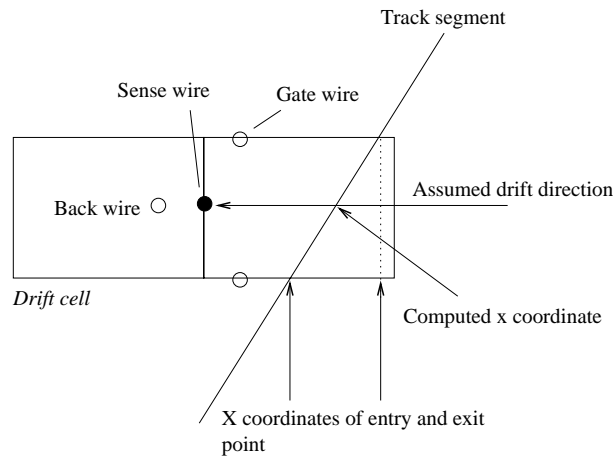


Figure 4.5: Simulation of the drift-time distribution in Monte Carlo events. The mean x value between entry and exit point of the track in the drift cell is taken to be the x coordinate for the hit reconstruction.

Reconstruction of the SDTR with the Online Software

To apply the method described above an input distribution dN/dx and a simulated drift-time spectrum dN/dT are needed. In Fig. 4.6 the simulated drift-time spectra for Monte Carlo data in X and stereo wires are shown. The reference distributions dN/dx are created with geometry information used in the Monte Carlo software. The fact that the maximum drift lengths for the wires are changing with their radial coordinate has been taken into account.

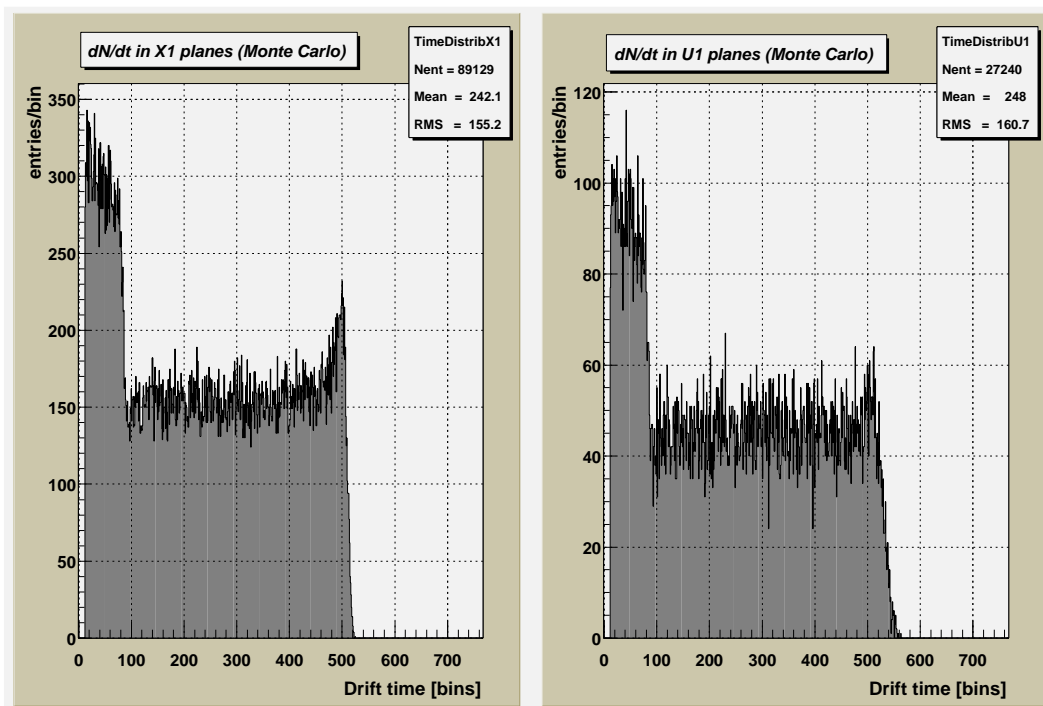


Figure 4.6: Reconstructed drift time distribution from Monte Carlo simulations for the X1 and the U1 wires. One time bin corresponds to $\approx 0.82ns$.

The figures show some interesting features:

- From the width of the back-drift region of 2 mm one would expect that the region of double hit density at small drift times extends to about one tenth of the maximum drift time. The measured peak is broader. This is because in the simulation software this region is assumed to be 3 mm wide. It does not affect the algorithm at all because the reference distribution can easily be corrected.
- For the X wires a pronounced rise in the number of hits is observed for large drift times corresponding to hits close to the end of the drift cell. This is due to the fact that tracks crossing the boundary between two drift cells are consistently assumed to cause ionization in both. They are ignored in one drift cell because they cross it on the blind side of the sense wire. The part of the trajectory which lies in the other cell is responsible for the pile up. It is explained by the fact that in the Monte Carlo software for inclined tracks crossing the cell boundaries the mean x value is computed from their entry point and the boundary of the drift cell. Figure 4.7 illustrates this. This approach affects the spatial distribution of x coordinates in the sense that larger x coordinates are enhanced. Their intersection with the x axis lies in the blind region of one of the drift cells but they *are* registered in the neighboring one. The detailed shape of the discussed enhancement is difficult to model and is beyond the scope of this work. However, one may expect similar effects in real data, as the principle assumption that primary ionization occurs

in both cells is true. For stereo wires this pile up is less pronounced. The distribution also falls off less steeply at large drift times than for the case of X wires. The reason for these differences is not clear.

- The peak of the distribution at small drift times has no constant height, but decreases as the drift time gets larger. The reason for this has to be inherent in the generation algorithm.

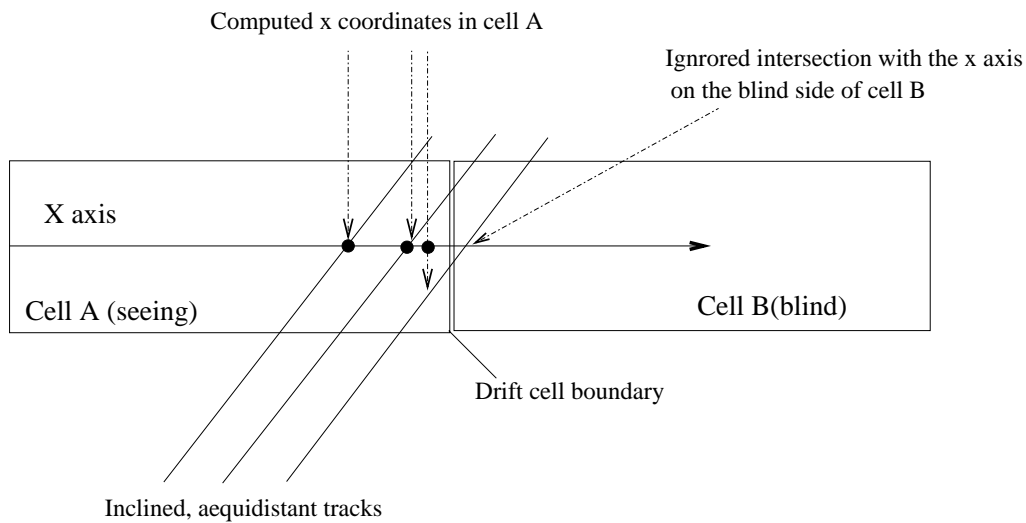


Figure 4.7: Tracks crossing the cell boundary are mapped to large x coordinates inside the seeing drift cell, whereas they are ignored on the blind side of the neighboring one. The Monte Carlo software therefore does not create a uniform distribution of hits throughout the drift cell.

The resulting distributions for the other wire types are similar to the ones shown in Figure 4.6. They are mapped to the reference distributions dN/dx as explained in section 4.2.2. Figure 4.8 show the resulting space drift-time

relations. As time unit in the reconstruction the width of the electronics time bin was chosen. As the width of these bins is slightly different for Monte Carlo simulation ($\Delta t = 0.82 \text{ ns}$) and cosmic-ray data ($\Delta t = 0.78 \text{ ns}$) the resulting drift velocity has to be scaled with the respective inverse bin width.

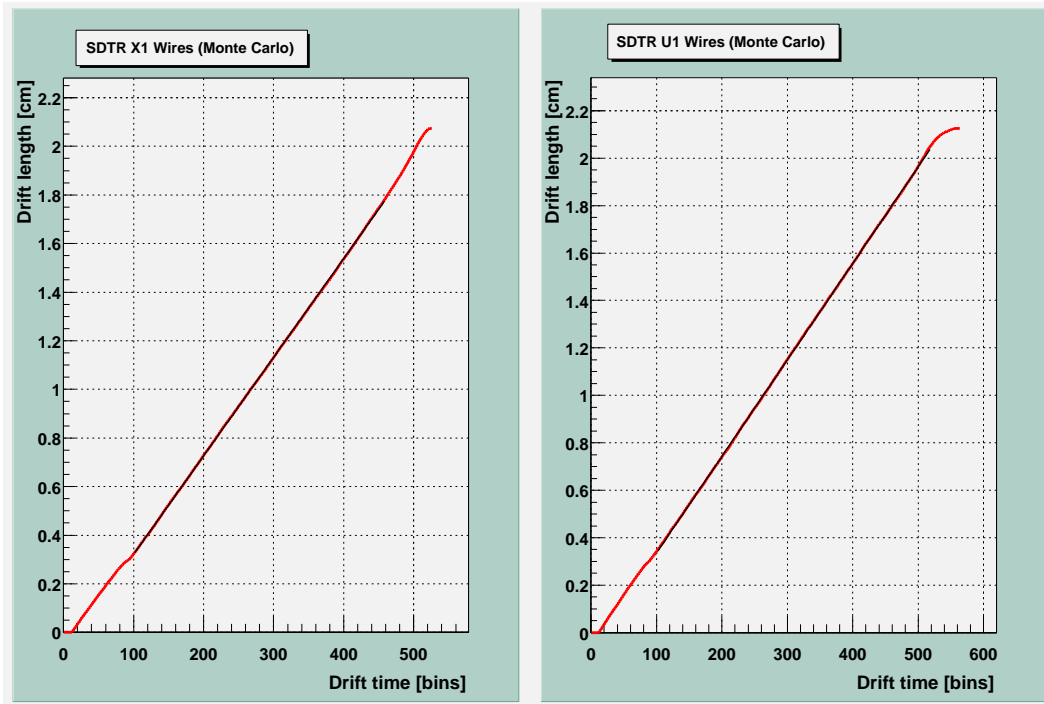


Figure 4.8: Integrated Monte Carlo space drift-time relation for the X1 and the U1 wires.

The deviation from a straight line at $\approx 1/7$ of the maximum drift length in the reconstructed space drift-time relation and the different slope for x coordinates smaller than the back wire distance is a consequence of the systematic change in height in the distribution dN/dt within the back-drift region. To obtain the drift-velocity the reconstructed relations have been fit to a linear func-

tion. The fit has been restricted to the linear part of the integrated spectrum in the drift region. One thereby avoids distortion of the drift-velocity fit by the discussed edge effects. In table 4.2 the reconstructed drift velocities and time offsets are compared with the values used as input for the Monte Carlo generation.

Wire type	drift velocity [$cm/\mu s$]	$t_0[ns]$
X1	(4.96 ± 0.01)	17.6 ± 0.7
U1	(4.95 ± 0.01)	16.2 ± 0.4
V1	(4.96 ± 0.01)	17.0 ± 0.6
X2	(4.99 ± 0.02)	16.9 ± 0.7
U2	(4.98 ± 0.01)	16.2 ± 0.4
V2	(4.96 ± 0.02)	14.1 ± 1.1
MC input	5.00	10

Table 4.2: Fit parameters and errors of the reconstructed Monte Carlo space drift-time relation

The reconstructed drift velocities deviate by less than 1% from the input value of $5 \times 10^{-3} cm/ns$ for all wires. The found t_0 parameters are clearly larger

than the input value of 10 ns in the simulation software. This is due to the restriction of the fit range. A straight line fitting the data points in the drift region clearly crosses the x axis at a too large t_0 compared to the data points at small drift times.

Obviously the reconstruction method can be improved in two aspects:

- The mean reconstructed drift velocity $\langle v_{Drift} \rangle = 4.97 + 0.01\text{ cm}/\mu\text{s}$ is slightly too small ($\approx 0.5\%$). The reason for the deviation is most likely the assumption of a uniform spatial distribution of hits in the drift chamber. The reference distribution dN/dx of hits should be generated in a way that takes into account cell crossing tracks. One possibility would be to take the output of the Monte Carlo generator directly as the spatial reference distribution.
- The simulation software needs to be investigated for possible reasons of the decline in the drift time distribution at small drift times that is obvious in the data and has to be checked for consistency with the offline software.

Although there is still room for improvement, the constant drift-velocity corresponding to a linear space drift-time relation can be reconstructed from the simulated data with less than 1% deviation. It remains to be investigated in which aspects the real drift-time and reference distributions deviate from the simulated ones.

4.2.4 Space Drift-Time Relation for Cosmic-Ray Data

Experimental Test Setup

To apply the discussed method to real data a cosmic ray test has been performed. The data analyzed in this and the subsequent chapters have been taken in mid December 1999. The experimental setup is schematically shown in Fig. 4.9. This setup should register mainly tracks at not too large angles against the radial direction ($|\alpha| < 10^\circ$) and thus a fairly linear space drift-time relation is expected. Cosmic rays, mainly muons, penetrated the chamber, ionized the gas along their track and were registered in two plastic scintillation counters which were coupled to photo multiplier tubes. A coincidence of the signals from both scintillators indicated a cosmic ray event and triggered the readout of the electronics. Furthermore, the coincidence requirement together with the geometrical setup of the scintillators with respect to each other and to the drift chamber defined the acceptance for cosmic-ray tracks. The geometrical acceptance was limited to about three kestones close to the center of the chamber.

The count rate during the data taking was slightly larger than 1 event per second. Several runs with typical voltage configurations for the drift chamber have been performed. The voltages on the back and potential wires have been varied systematically to find the configuration for the optimum single-wire efficiency and back-drift efficiency. The configurations are given in chapter 5.2.1 together with a discussion of the results.

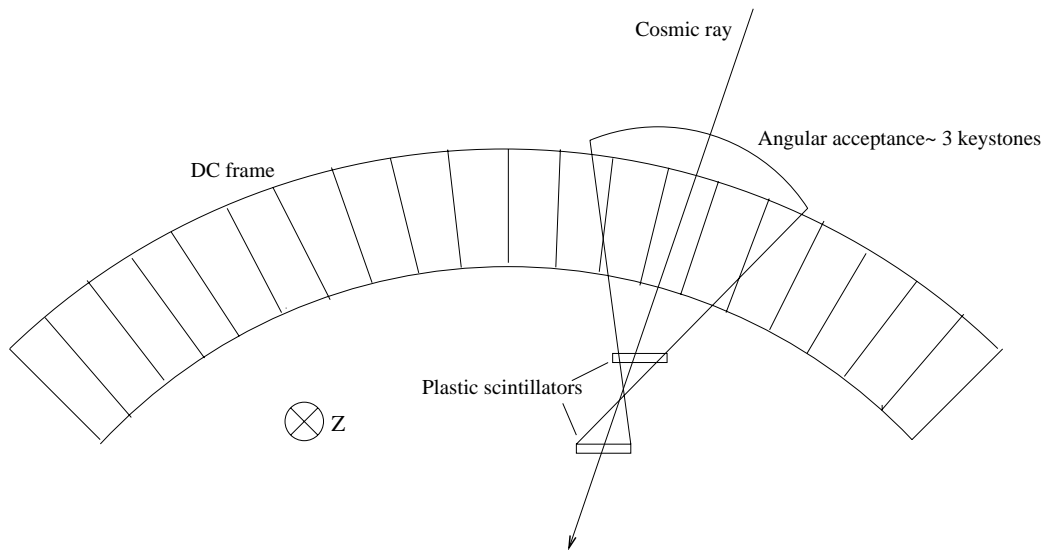


Figure 4.9: Cross section of the experimental setup for taking calibration data using cosmic rays. In the z direction the setup covers about half the depth of the chamber

Determination of the Space Drift Time Relation

Figure 4.10 shows the number of hits registered per channel in the four wire layers of one keystone in the geometrical acceptance of the cosmic-ray measurement. For this analysis 1800 events have been recorded. Clearly noisy channels are visible in the spectrum. Dead channels have to be found after the noisy wires have been excluded. They have to be tagged as unusable for the analysis of the single-wire efficiency.

The corresponding drift time spectrum for the X channels is shown in Fig. 4.11. The hits registered after the nominal trailing edge of the time distribution can be attributed to noisy channels. Since these distort the real

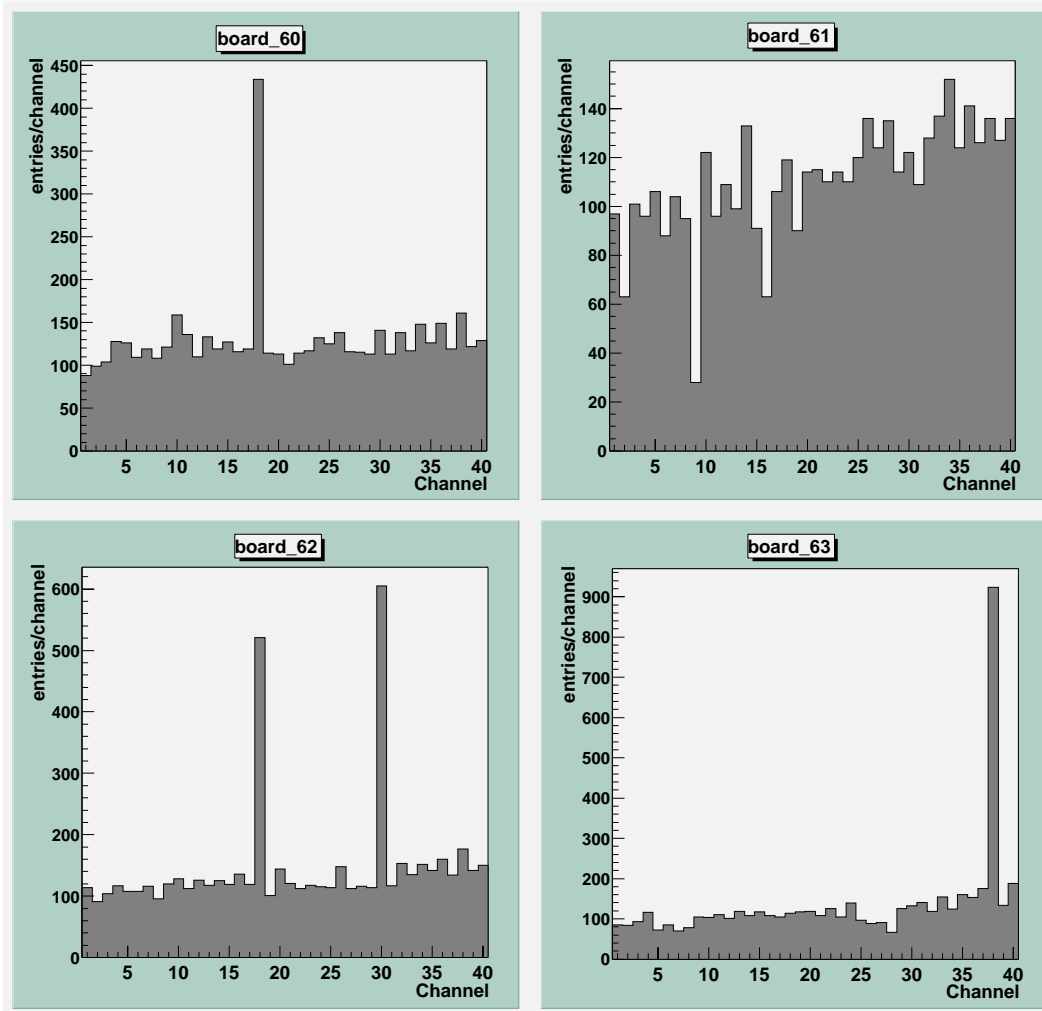


Figure 4.10: The number of hits in the channels of one keystone for 1800 cosmic-ray events. The noisy wires (visible as spikes in the distribution) need to be tagged as unusable in the analysis.

drift-time distribution a reconstruction of the space drift-time relation from the spectra shown in Fig.4.11 is not possible. To mark found noisy and dead channels and remove them from the analysis, a configuration tool has

been created for the online monitoring software. It allows the user to disable or enable sense wires in the current analysis in groups or one-by-one.

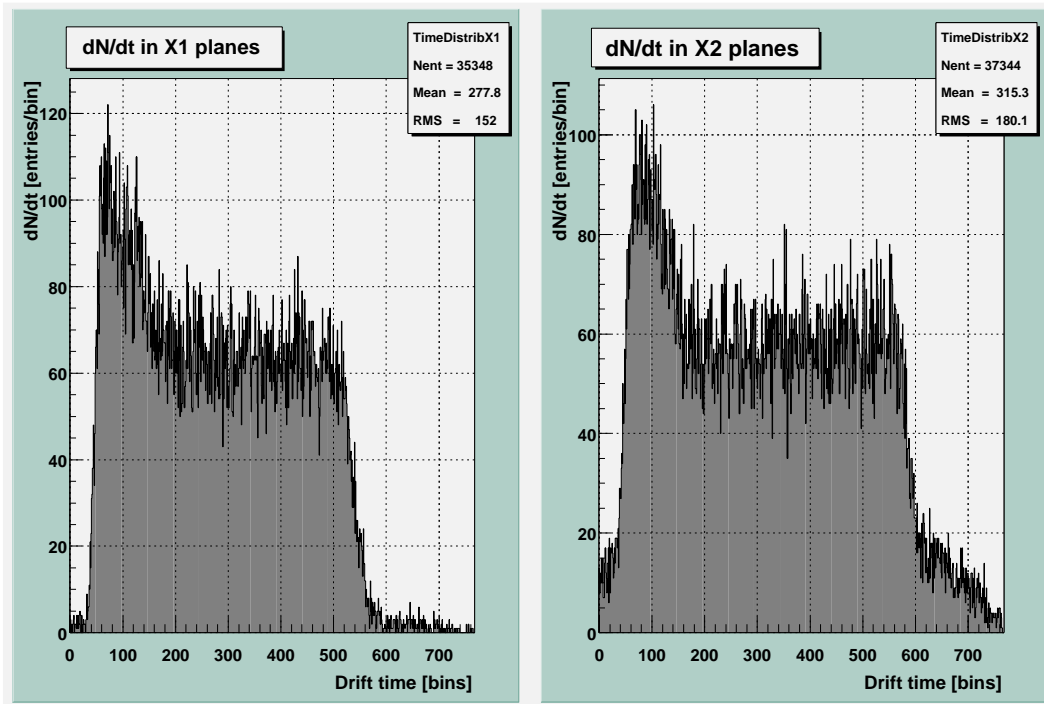


Figure 4.11: The drift-time distribution obtained from the cosmic-ray test with all wires enabled. A small noise tail for the X1 wires (left) and a huge noise contribution for the X2 wires (right) is visible at drift times beyond the leading and trailing edges of the distribution. One time bin corresponds to ≈ 0.78 ns.

After switching off all noisy channels, the drift-time spectra are closer to the expected shape. Figures 4.12 to 4.14 show the “cleaned” drift-time distributions for X, U, and V wires. These show interesting features which need to be understood:

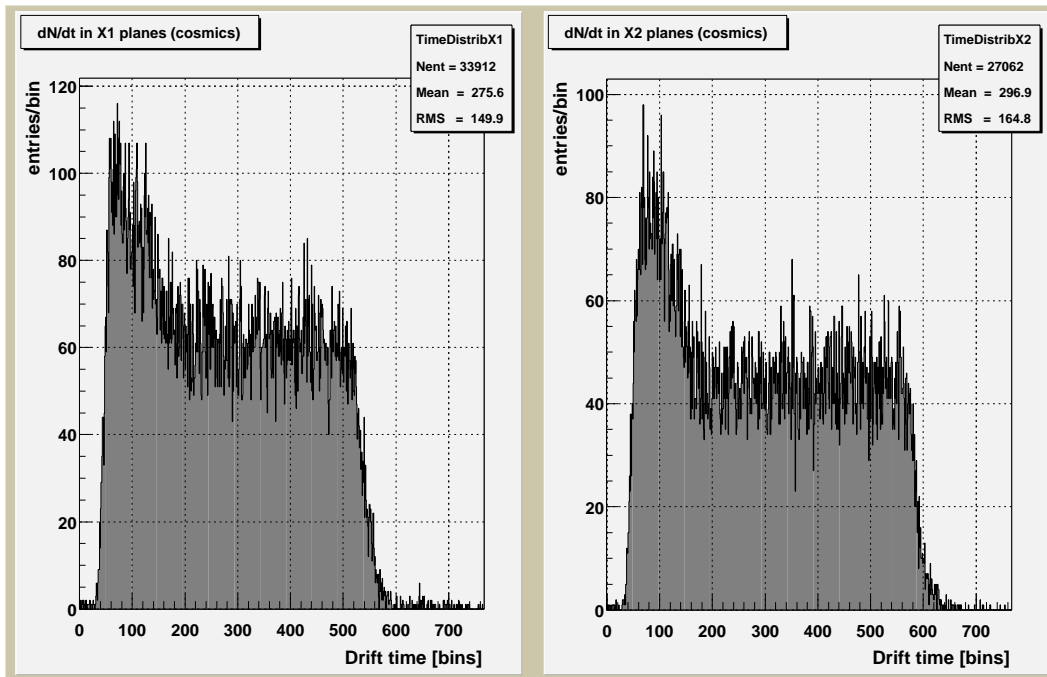


Figure 4.12: Drift-time distribution for the X wires in the cosmic-ray test after switching off all noisy channels. The bin width corresponds to ≈ 0.78 ns.

- The region of double hit density at small drift times corresponds to more than the geometrical width of the back-drift region. Assuming a linear space drift-time relation, the “effective width” of the back-drift region is about 3 mm. A possible explanation for this observation is illustrated in Fig. 4.15. Shown is an inclined track crossing the x axis outside the back-drift region. Nevertheless, it creates primary ionization inside that region which gives rise to a signal on the sense wire. The drift length of these ionization products can be up to 3 – 3.5 mm, which corresponds to roughly one seventh of the maximum geometrical drift length. This is in

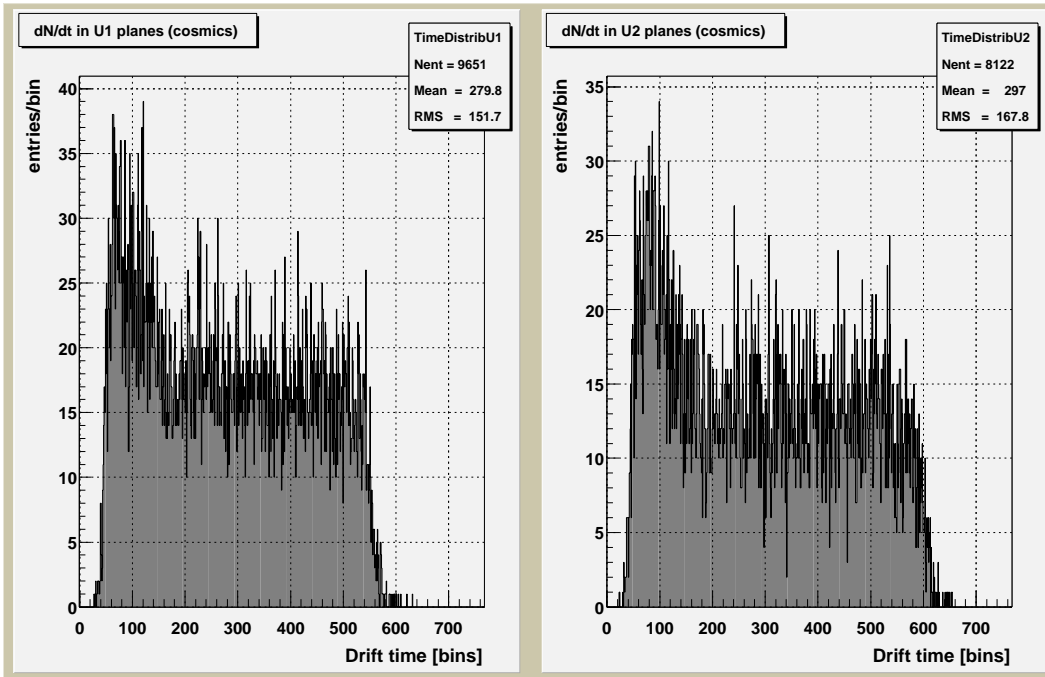


Figure 4.13: Drift-time distribution for the U wires in the cosmic ray test after switching off all noisy channels. The bin width corresponds to ≈ 0.78 ns.

fact in much better accordance with the measured spectra. Therefore, an effective width has to be used for the reconstruction of the space drift-time relation.

- The back-drift region is not uniformly filled with hits, but the hit density decreases with increasing drift time. In Fig. 4.16 the reason is illustrated. According to GARFIELD simulations the field lines are bent so strongly, that charge created close to a sense wire by a traversing particle does not necessarily reach the sense wire but is drifting towards the back wire instead. Charge from an isochrone further away is measured on the

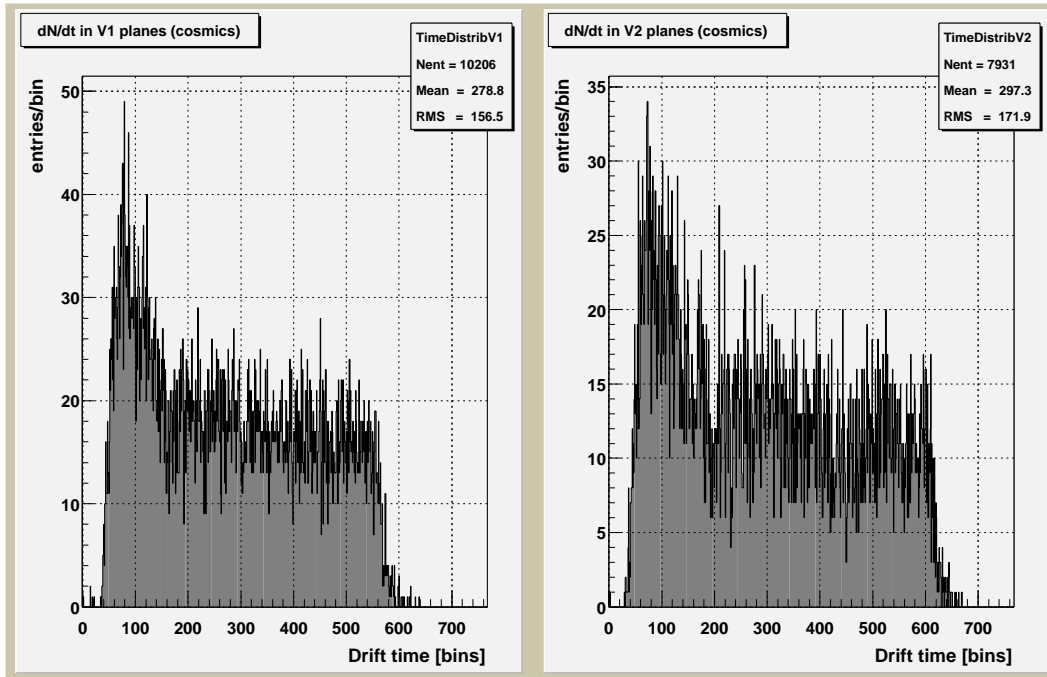


Figure 4.14: Drift-time distribution for the V wires in the cosmic-ray test after switching of all noisy channels. The bin width corresponds to $\approx 0.78 \text{ ns}$.

sense wire. The drift-time distribution in the back-drift region is biased, as signals from strongly inclined tracks are shifted to larger drift-times.

These effects are difficult to anticipate quantitatively. For a first analysis, they are best taken into account by the use of an effective width in the reconstruction of the space drift-time relation and by excluding inclined tracks from estimates of the single-wire efficiency.

To proceed with the space drift-time algorithm, one has to choose the drift times which define the lower and upper boundaries of the measure dN/dt to be used for the mapping procedure. Outside these boundaries, hits are at-

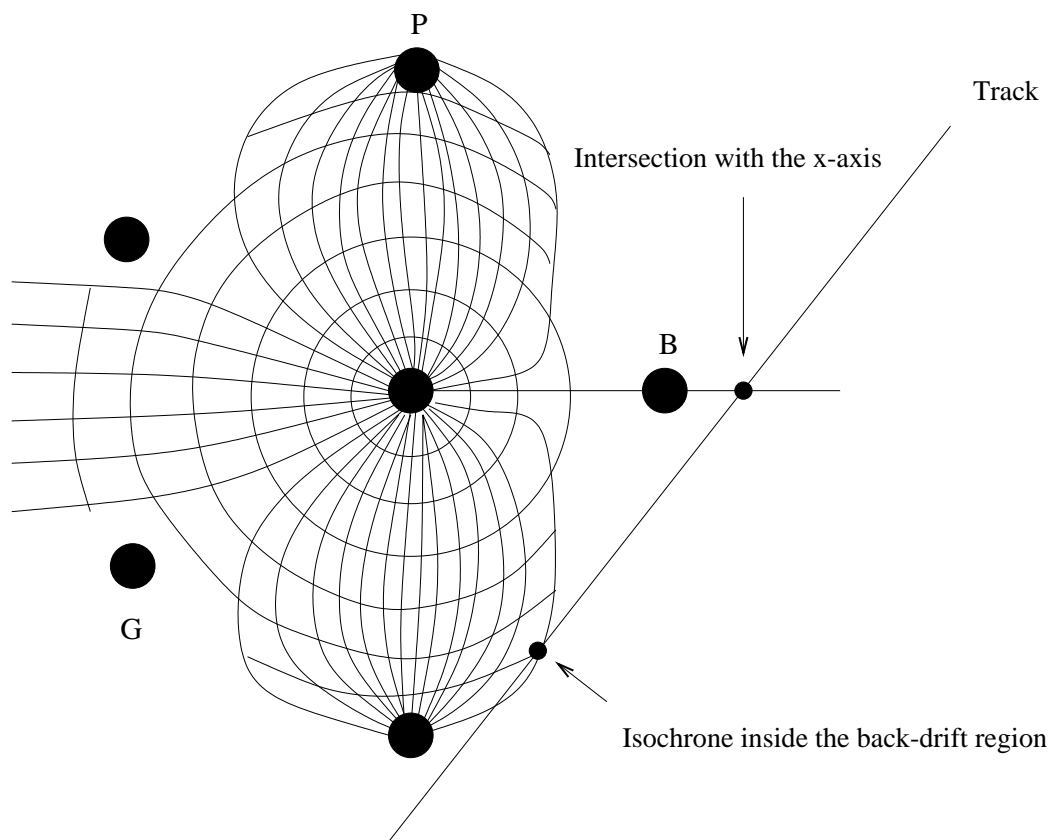


Figure 4.15: An inclined track crossing a drift cell. Although the track passes the x axis outside the back-drift region it creates primary ionization inside.

tributed to noise and are therefore ignored. Currently as boundaries the drift times found at the half heights of the leading and trailing edge, respectively, are selected. The distributions are then mapped to the spatial reference distributions dN/dx in the same way as the Monte Carlo data. The resulting space drift-time relations are shown in Fig. 4.17 to 4.19 for X, U, and V wires.

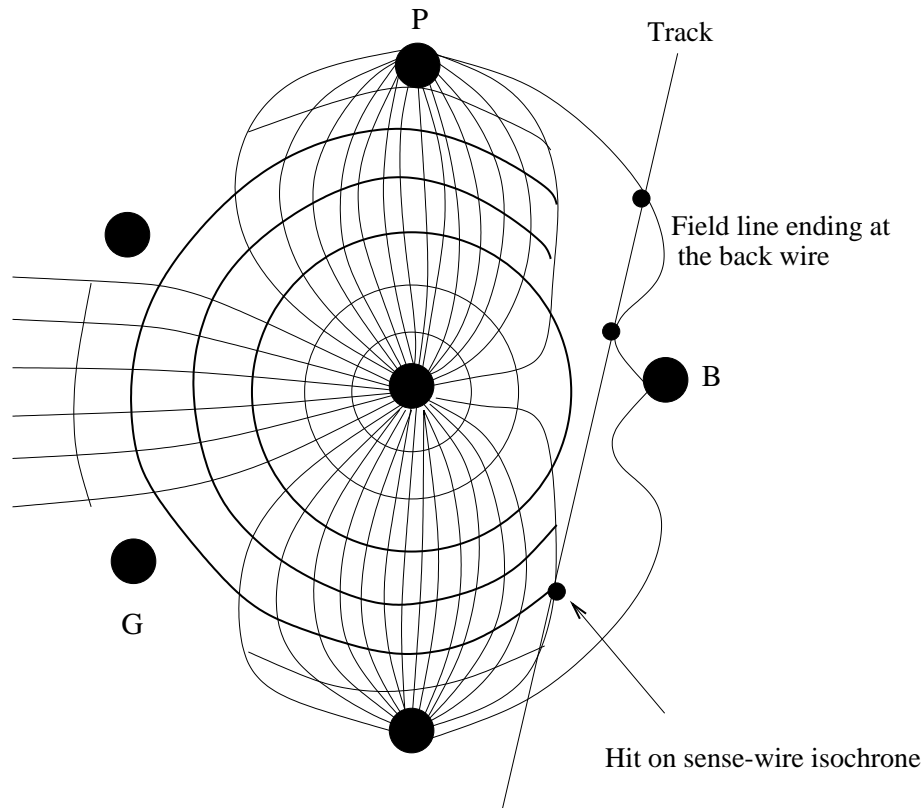


Figure 4.16: A track passing the x axis between sense and back wire. Although it comes relatively close to the wire, charges reaching the sense wire earliest have a long drift way. The reason is that in the back-drift region some field lines end on the back wire and charges created on them do not reach the sense wire.

Discussion of the Results

A linear function has been fit to the data points that were obtained from the mapping procedure. In table 4.3 the resulting values for the χ^2 fit of the drift velocity are listed. The fit range has been restricted to the drift region,

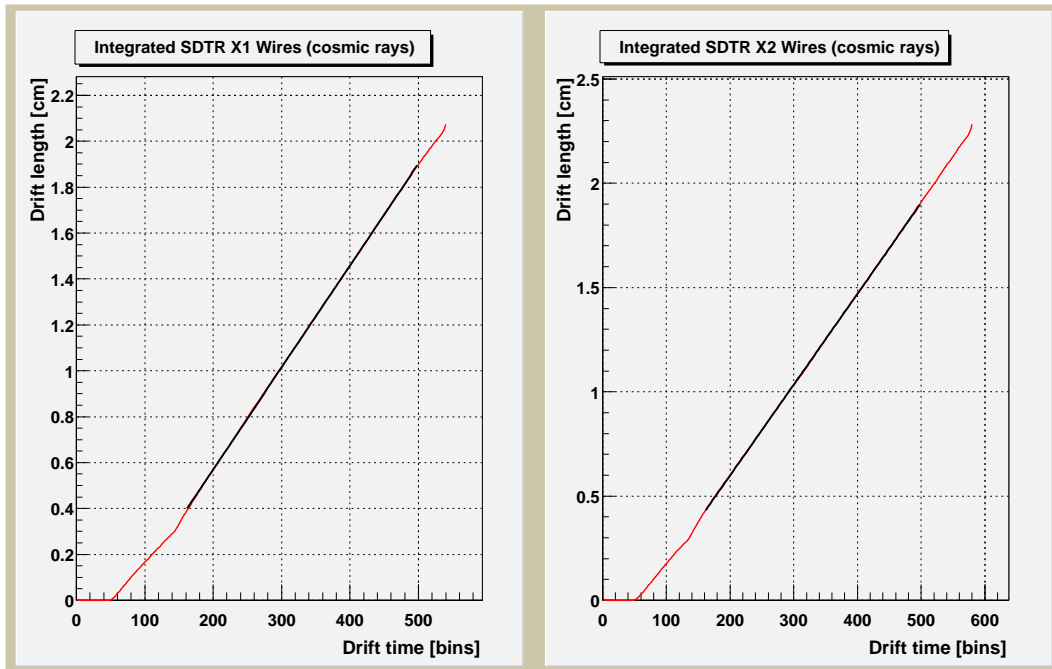


Figure 4.17: Space drift-time relation reconstructed from cosmic-ray data for the X wires.

i.e. to a range of time bins from 180 to 500. The time offset t_0 therefore cannot be determined correctly from the limited fit. The found drift velocities are too large. One expects drift velocities on the order of $5\text{cm}/\mu\text{s}$. This indicates, that the boundaries for the cut off in the drift-time distribution need to be adjusted more carefully. In the reconstruction t_0 has been chosen at the half height of the leading edge of the drift-time distribution in accordance with the boundary that has been applied to the drift-time distribution before the mapping to the reference distribution was performed. A linear dependence of x coordinate and drift time is apparent outside the back-drift region, i.e. for drift times larger than 180 time bins. The different behavior inside the back-drift

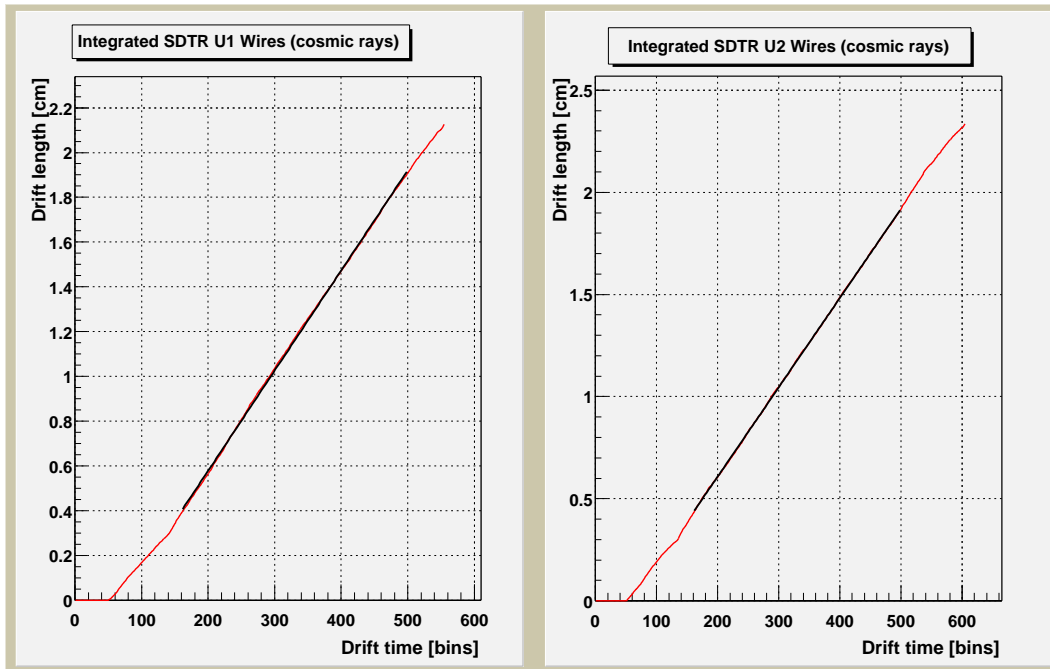


Figure 4.18: Space drift-time relation reconstructed from cosmic-ray data for the U wires.

region is due to the deviations of the drift-time distribution from a uniform plateau as discussed above. The reconstruction has been done assuming an effective width of the back-drift region of 3 mm . The change in slope of the space drift-time relation at the boundary of drift region and back-drift region is most pronounced for the X1 wires. It decreases gradually if one looks at the different wire cages in the order X1, U1, V1, X2, U2, V2, i.e. with growing radial coordinate the distributions approach linearity. This is probably due to a smaller acceptance for tracks with large angles for wires at larger radial distance. The fit parameters for the drift-velocity vary up to $\approx 3\%$ but within the errors they all agree. Therefore, for the reconstruction of tracks a constant

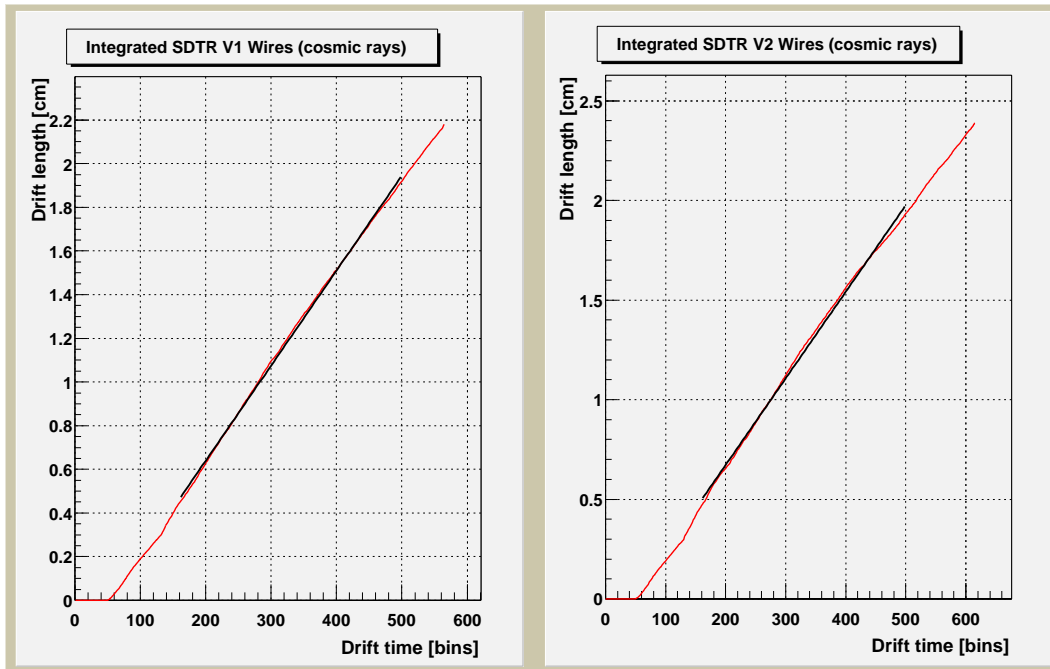


Figure 4.19: Space drift-time relation reconstructed from cosmic-ray data for the V wires.

drift velocity is chosen for all wire types in the chamber. To improve the reconstruction of the space drift-time relation a more sophisticated spatial reference distribution is needed that is corrected for the effects caused by inclined tracks. To obtain an accurate reference, one would have to model the broadening quantitatively. Furthermore, the reconstruction of the correct x coordinates for tracks crossing the back-drift region is ambiguous, since a priori the track direction which is related to the true x coordinate is not known. For the time being an approximate space drift-time relation is used as input to the tracking routine. The tracking algorithm and relevant performance parameters are discussed in chapter 5.

Wire type	drift velocity in [$cm/\mu s$]	χ^2
X1	(5.68 ± 0.256)	0.017
U1	(5.73 ± 0.268)	0.016
V1	(5.57 ± 0.271)	0.041
X2	(5.58 ± 0.270)	0.014
U2	(5.59 ± 0.271)	0.028
V2	(5.57 ± 0.273)	0.094

Table 4.3: Fit parameters and χ^2 values of the fit of the cosmic-ray space drift-time relation to a linear function.

Chapter 5

Track Finding and Detector Performance

5.1 Combinatorial Hough Transformation in Coordinate Space

5.1.1 Feature Space for the Transformation

The hit information from the calibration stage is used to reconstruct three dimensional particle tracks in the DC via a two-fold Combinatorial Hough Transformation (CHT). The algorithm is outlined in the following:

The magnetic field of PHENIX, which bends the tracks of charged particles to allow for the reconstruction of their four momenta is so small inside the drift chamber that, except for tracks with a very small transverse momentum ($p_t < 200 \text{ MeV}/c$), the deflection of the traversing particles is less than 1° on their path through the chamber volume. In good approximation, the task of reconstructing tracks is thus reduced to finding hits which follow straight lines through the chamber. A well established technique for this purpose is

the Simple Hough Transformation (SHT) [24]. In the SHT, a point in real space is identified with a line in the Hough space or feature space. This is a two-dimensional space in which the coordinates are chosen to be the slope and the intercept value of a line through the point in position space which is to be mapped into the feature space. Each point in the two-dimensional position space is thus mapped onto a line in feature space that corresponds to all possible combinations of slope and intercept describing lines through the point. This is illustrated in Figure 5.1a. Hits that belong to the same track in real space have feature-space lines intersecting at one particular point in Hough space, which corresponds to the slope and the intercept of the straight line representing the track. In PHENIX, however, the SHT is not a suitable method, as, because of the high track density in the chambers, many so called ghost tracks are found when hits from different tracks are combined to a track that does not actually exist. To overcome this problem, the CHT uses *pairs* of points to determine the feature-space distribution. Two points are assumed to belong to the same track and the Hough coordinates (slope and intercept) of the line which is thereby defined are determined. The two physical points are thus mapped into one point in feature space representing the Hough line. The number of feature-space lines crossing in one point for an actual track in the SHT is the number of hits n contributing to it. In the CHT, the relevant number is the number of hit pairs $n \times (n-1)/2$. Thus the signal-to-background ratio is much better and the tracking problem due to the large hit density in the chamber is reduced. Figure 5.1b illustrates the differences between the two Hough transformations.

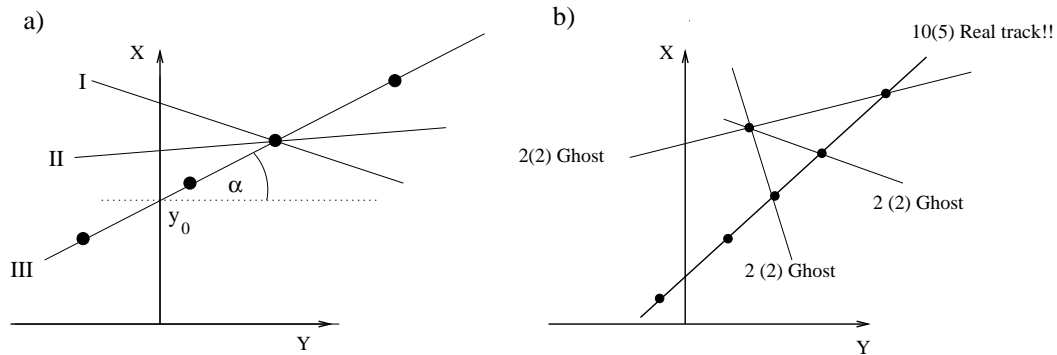


Figure 5.1: a) In SHT each hit corresponds to infinitely many possibilities of slope and intercept represented by a line in Hough space (Lines I, II, and III e.g. all cross at the same point.). The four hits lying on line III have the same *true* values for the feature space variables, so their Hough-space lines intersect *in one point*. In CHT line III can be constructed from any two hits on the track which results in $(4 * 3)/2 = 6$ entries in the Hough-space bin corresponding to the angle α and the intercept y_0 .

b) For each shown track *candidate* the number of entries in the feature space distribution is given for CHT and for SHT (in brackets). The ratio of the number of entries for true and ghost tracks is clearly improved using CHT.

5.1.2 CHT in the Drift Chamber

Track Reconstruction in Two Dimensions

The DC tracker performs one Hough transform to obtain a track projection into the plane perpendicular to the z axis. In this projection the feature-space variables are the azimuthal angle Φ of the intersection of the Hough line with a reference circle of radius R in the chamber and the angle

α at which the line crosses this circle with respect to the radial direction. The feature space variables for the first CHT are illustrated in Figure 5.2.

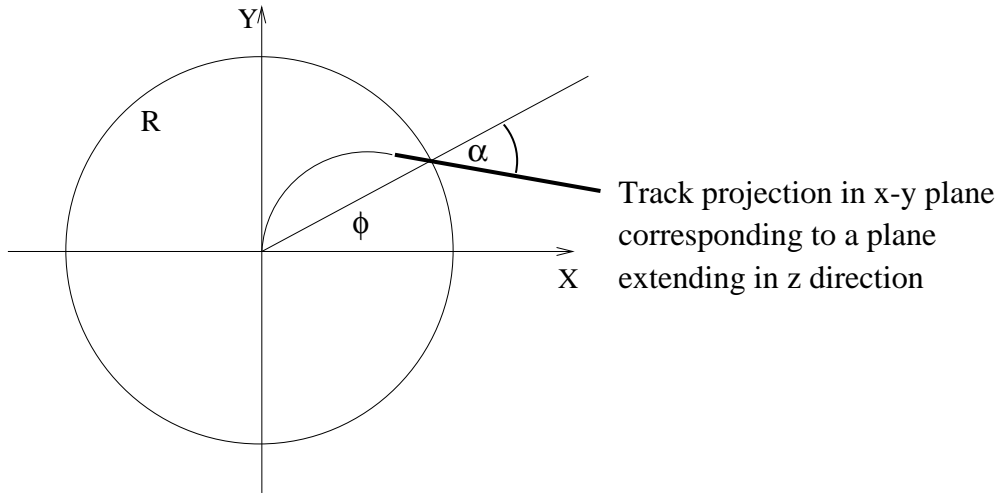


Figure 5.2: Feature-space coordinates for the X wire Hough transformation.

The advantage of these variables is that they are limited to finite range, whereas slope and intercept of the Hough line are not. For this stage of the track reconstruction only the X wire information can be used since only these wires are parallel to the z axis. To minimize peak width in feature space and thereby reduce the uncertainty in the angular reconstruction of the track and to optimize the signal-to-background ratio, only combinations of X1 and X2 wires are used to populate the Hough space. Figure 5.3 shows parts of a simulated hit distribution in a central Au+Au collision and part of a typical feature-space distribution. The tracks are clearly visible by eye. The peaks in the feature-space plane correspond to possible track candidates. The tracking algorithm applies a cut on the minimal number of entries in a Hough bin (i.e. the number of point pairs for this bin) to decide whether a track has been found. The

threshold for track reconstruction in the simulation has been set so that at least 4 wires in each X1 and X2 cage or at least 3 in one cage and 6 in the other cage must contribute to a track.

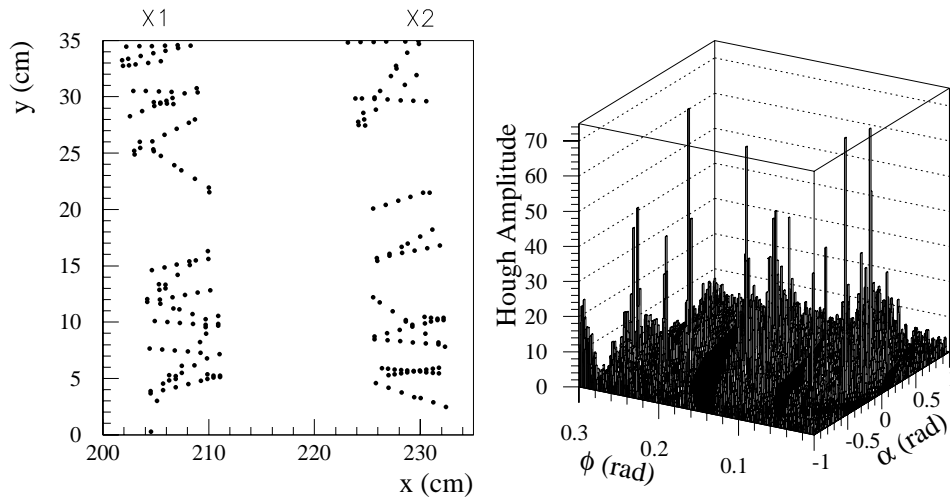


Figure 5.3: X wire hits in the DC for a central collision and typical feature-space distribution.

Tracking with the UV Wires

As a single sense wire that registers a signal can not give any information about the z coordinate at which a track passed it, a hit on a sense wire in the drift chamber corresponds to all points on a line in space. The position of this line in space is determined by the extent of the chamber, the end points of the sense wire and the drift direction. As no z information can be obtained from the X-wire hits, the result of the first Hough transform is a projection of

the track into the plane perpendicular to the beam axis. In three dimensions this corresponds to a plane extending in the z direction as can be seen from Figure 5.2. To reconstruct the path of the particle in this plane a second Hough transform is performed. Therefore, the information from the U and V wires is used. The straight lines reconstructed from signals recorded on U and V wires are very good approximations of the actual isochrones and can therefore be used for track reconstruction. The lines given by the stereo-wire hits cross the plane resulting from the first Hough transformation. The intersection points of UV-hit lines with the plane line up along the trajectory if they belong to a real track. These intersection points are the input to the second Hough transformation. The feature-space variables are now zed and β . Here zed is the z -coordinate at which the track candidate intersects the reference radius that has been introduced in the first CHT to define the variable α and β is the angle of the intersection as illustrated in Figure 5.4. For stereo wires also only combinations of UV1 and UV2 hits are used.

After the hits on the wires have been combined to populate the hough space the tracks have to be fit to the contributing hits. For the fit to the points one has to use a function which depends on the magnitude and shape of the magnetic field. Without field the tracks are straight lines. If the field is switched on, the tracking software needs to fit the trajectory to a track model which takes into account the small bending of the track inside the chamber. For the time being the track model is under development and as a first order approximation straight lines are used. The fit to the points is a two step procedure using an analytical fit routine. In the first step, the projection of the

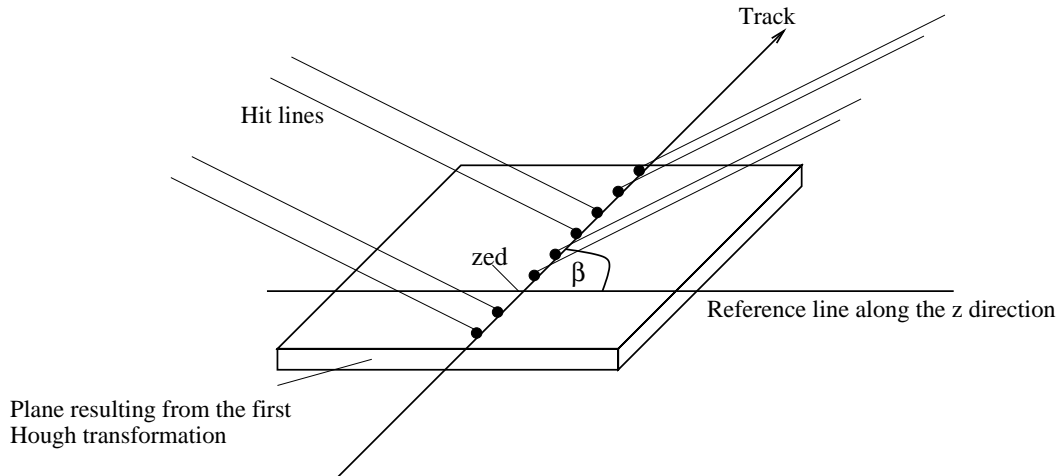


Figure 5.4: Feature-space coordinates for the stereo-wire Hough transformation.

track in the transverse plane is fit to the X-wire hits, which in this projection are points. In the second step the track is fit to the intersection points of stereo-wire hit lines with the plane defined by the first hough transformation.

Performance and Track Reconstruction

The C++ program package for the CHT was written by members of the Stony Brook heavy-ion group [25]. Convenient objects and manipulation methods to represent the data and perform geometrical operations on them form the basis of the PHENIX drift-chamber tracker. The method proves very robust at the high track densities expected in PHENIX and allows reliable reconstruction of events. The total track-reconstruction time for a central Au+Au event is 5 to 10 seconds in the current version of the software. Using Monte-Carlo simulations as input, the track-finding efficiency in two dimensions has been

determined to be 98% at a ghost-track rate below 1% for the expected multiplicities. In three dimensions, the track-finding efficiency is 92 %, whereas the ghost-track rate remains below 1 %. This efficiency is maintained above a momentum threshold of $200\text{MeV}/c$. Below that, the residual magnetic field bends the tracks significantly and the assumption that tracks follow straight lines is no longer justified. For the cosmic-ray test and for Monte-Carlo simulations that have been generated without taking a magnetic field into account, this model is correct and it provides the basis of the resolution and efficiency measurements presented in chapter 5.2.3 and 5.2.1.

5.2 Relevant Tracking Parameters

5.2.1 Single-Wire Efficiency and Back-Drift Efficiency

Single-Wire Efficiency

The single-wire efficiency is defined as the mean number N_{Hits} of hits registered on a wire divided by the number N_{ideal} of hits that were supposed to be registered on it. The design of the drift chamber aims for a single-wire efficiency above 99 %. To determine whether a hit that was supposed to be registered for a particular track was actually measured, one looks for hits in a fiducial volume around the track element in the corresponding drift cell.

Back-Drift Efficiency

As each wire is blind outside the back-drift region to one side, no charge clouds coming from there should be registered. The back-drift efficiency is defined as the mean number of hits registered by mistake outside the back-drift region on the blind side N_{Back} divided by the total number of possible back efficient hits $N_{BackMax}$ on the wire. The DC design goal is a back-drift efficiency below 1.5 %. It is possible to determine efficiency and back-drift efficiency very easily in low multiplicity events or in the cosmic-ray test using an algorithm described in the following.

Determination of Drift Cell and Sensitive Direction

A search method needs to be developed that finds out whether a given wire was supposed to register a signal from a track. Each track is given as a line in three-dimensional space. Therefore, it is possible to determine the exact drift cell it crossed in each layer of wires from its intersection coordinates with a cylinder defined by the layer's effective radius. The next step is to find out whether the sense wire in this particular cell is blind towards the side on which the track passed it, or whether the track crossed the cell within the back-drift region. This information is obtained from the geometry parameters and wire positions in the drift chamber.

Track Distances in Drift Direction

If the wire was supposed to register a hit from the track, the distance of the expected hit from the wire has to be computed. For that purpose,

one can not simply use the minimum distance of the lines defined by the wire and the track. Figure 5.5 shows that this distance does *not* correspond to the true drift length of a registered hit. The true hit distance is the distance in drift direction between the sense wire and the track.

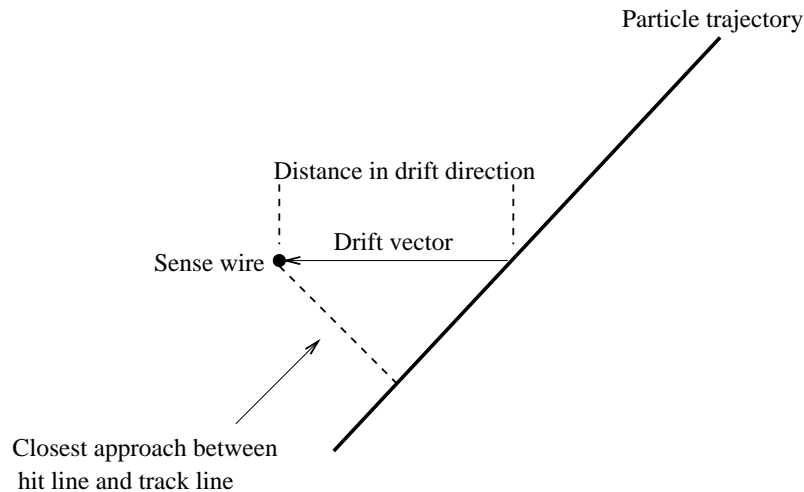


Figure 5.5: The closest approach of the track line and the wire line does not represent the drift length of an ideal hit. What actually needs to be determined is the distance in drift direction.

For the X wires, the drift direction is a constant and is known from the PHENIX geometry database once a hit has been identified by the physical coordinates of its signal wire. The drift direction for the stereo wires varies with the z coordinate of the hit, as illustrated in Figure 4.1. As, a priori, there is no z information for a particular hit, one needs to reconstruct it from the trajectory itself. The track model is parametrized as a mathematical function for which in the straight-line approximation only a base point and a direction vector are required. To obtain z information, the radial distance of a track

point from the beamline is set equal to the radius of the wire on which the hit was measured. For X wires the radius is constant. For stereo wires it varies on the order of $1 - 2\text{ mm}$ from the end points to the center and therefore the mean value is used. This allows to determine the z coordinate by intersecting the track with the cylinder defined by the effective radius. The two points at which the track crosses the cylinder are calculated. This two-fold ambiguity in the punch-through point is resolved by choosing the one closer to the sense wire. Figure 5.6 a illustrates the procedure to find the z position of a hit.

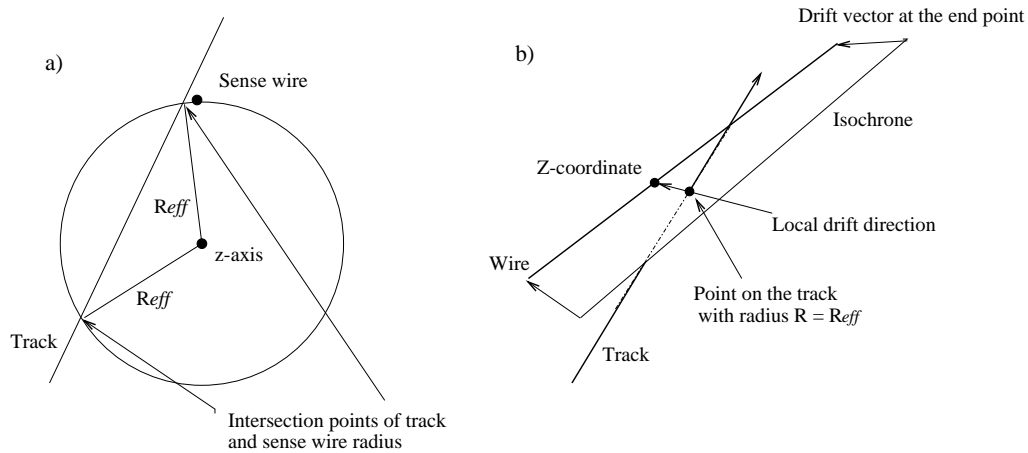


Figure 5.6: a) The z coordinate of a tracks punch-through point through the cylinder defined by the radial distance of the wire from the vertex must be determined to obtain the local drift plane.

b) The track is then intersected with this plane to find the ideal position of the hit.

The obtained z coordinate is used to calculate the local drift direction at the punch-through coordinates by linear interpolation between the values at

the wire end points. The drift vector and the wire direction define a plane, and the punch-through point of the track through this plane can be determined. This is illustrated in Figure 5.6 b. The result defines the nominal position of a hit on a track. If one of the hits recorded on the wire is within a maximum distance 1 mm from this position, the wire is counted to be efficient for this particular track. The width of 1 mm is chosen in accordance with the obtained resolution of the drift chamber of $\approx 330\ \mu\text{m}$ (See chapter 5.2.3. In a window of 1 mm one expects to find 99 % of all hits.

If the wire is supposed to be blind, the same computation is performed and if a hit that occurred *outside* the back-drift region was registered within a distance window of 1 mm the wire is counted to be back efficient for the track. In the next sections the resulting efficiencies for cosmic ray data are presented and discussed.

5.2.2 Single-Wire Efficiency in Cosmic-Ray Data

Fiducial Cuts on the Reconstructed Tracks

For cosmic-ray data, one needs to apply certain restrictions upon the tracks that are used to measure the efficiency. These restrictions are justified and explained in the following. The voltage settings in the cosmic ray runs have been varied systematically within the range of the possible operating regimes. The voltages on the different wires are given in Table 5.1.

Run	$U_{cath}[V]$	$U_{gate}[V]$	$U_{back}[V]$	$U_{pot}[V]$
0	4700	1550	900	2300
1	4500/4600	1550	900	2150
2	4500/4600	1550	900	2250
3	4500/4600	1550	900	2350
4	4500/4600	1550	800	2350
5	4500/4600	1550	900	2400
6	4500/4600	1550	900	2150

Table 5.1: Voltage configurations in the different cosmic ray data taking runs with the drift chamber. (The numbers in the cathode wire column are the voltages in X1 & UV1/ X2 & UV2.)

Figure 5.7 shows the azimuthal distribution of the tracks reconstructed in the cosmic-ray test. To avoid edge effects that arise from the acceptance cutoff at the boundaries, only tracks registered in the region $41^\circ > \Phi < 47^\circ$ are used. In Figure 5.8 the distribution of the inclination angle α of the tracks with respect to the radial direction is plotted. To make sure that only tracks that traversed the chamber almost vertically are analyzed and that no ghost tracks

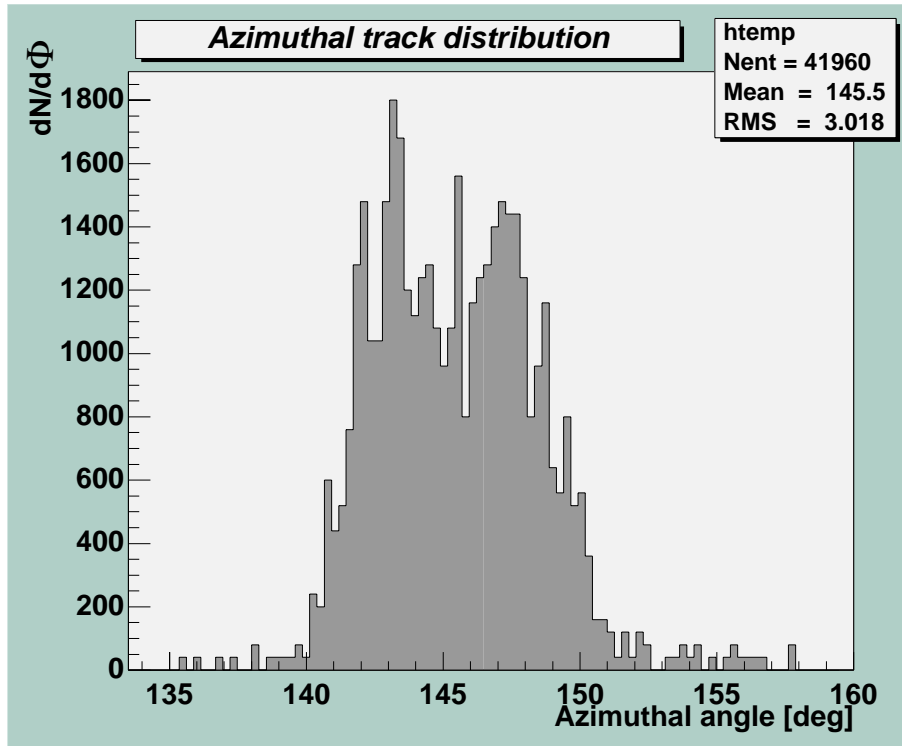


Figure 5.7: Φ distribution of registered tracks in the cosmic-ray test.

reconstructed outside the bulk of the distribution distort the measurement, α is required to lie within an interval of $\pm 5.5^\circ$.

A similar cut is necessary for the angle of the found tracks with respect to the z axis. Figure 5.9 shows the distribution of the polar angle Θ . As tracks traversing the chamber at polar angles far away from 90° deposit more charge on the sense wires, they produce longer signal pulses. Due to this and to diffusion along the charge drift lines their position measurement is less accurate. That influences the probability that they become associated to a track. To avoid this bias and to make sure that only tracks that are well within

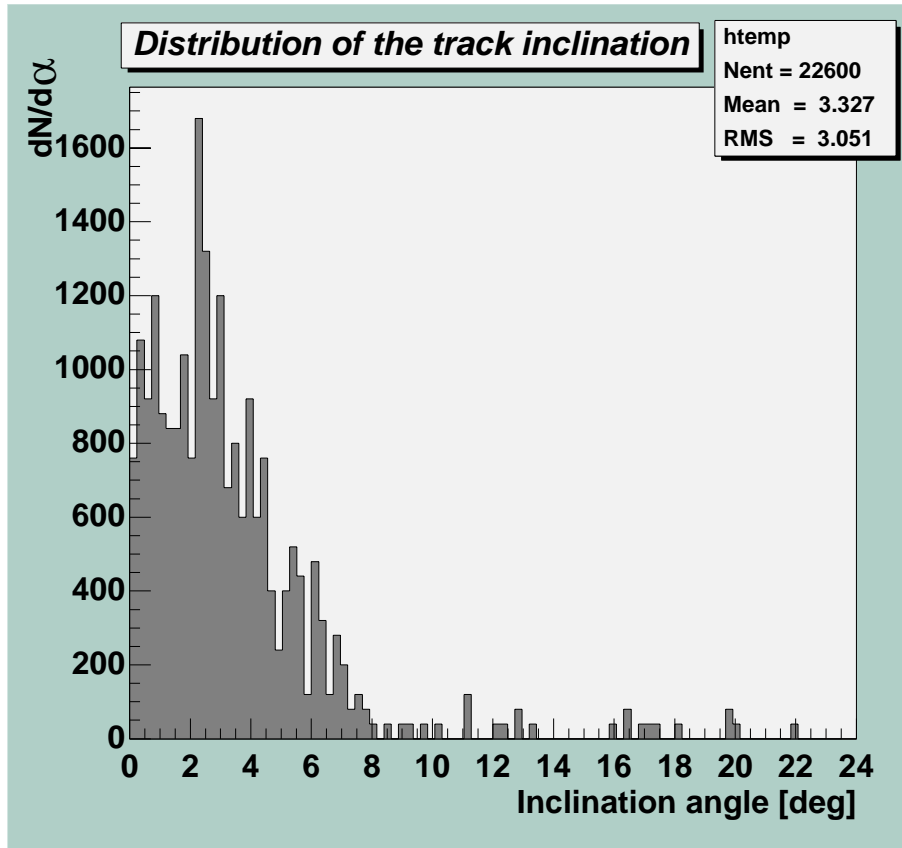


Figure 5.8: Distribution of the inclination angle α for registered tracks in the cosmic-ray test.

the acceptance of the trigger setup are used, a cut on Θ is applied, requiring that $78^\circ > \Theta < 102^\circ$. As the space drift-time relation is not expected to be accurate within the back-drift region and at the end of the drift cell, one also has to cut on the drift length of the hits. Only hits with a drift length between 0.6 cm and 1.7 cm are used. Figure 5.10 shows in white the distribution of hits that have been associated to the track. The distribution plotted in black represents the fraction of all hits that are used in the measurement after all

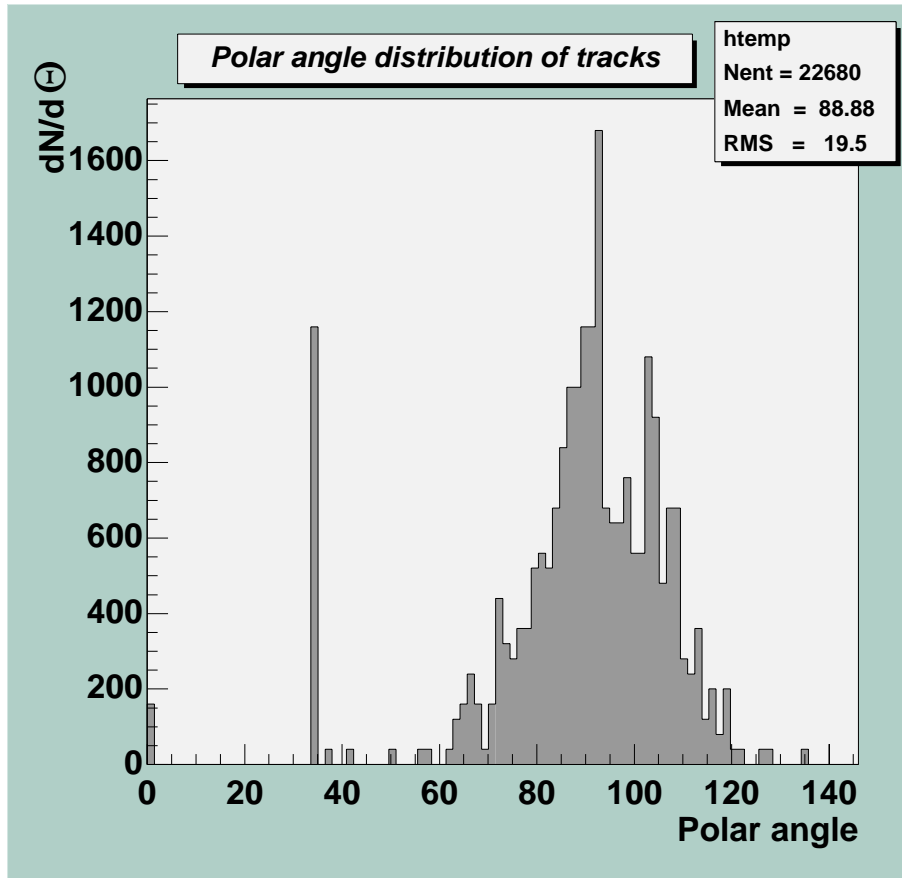


Figure 5.9: Distribution of the polar angle of the tracks. The peak at $\Theta \approx 35$ represents tracks that could not be reconstructed three dimensions and got assigned a default value.

cuts have been applied. In Figure 5.11 the distribution of the number of stereo-wire hits associated to a track is plotted. For this distribution no additional hit association of the monitoring software was used. It is apparent, that the tracking software does not find 8 hits in most of the cases as would be expected for an almost perfect track reconstruction. It is not possible to make a decisive

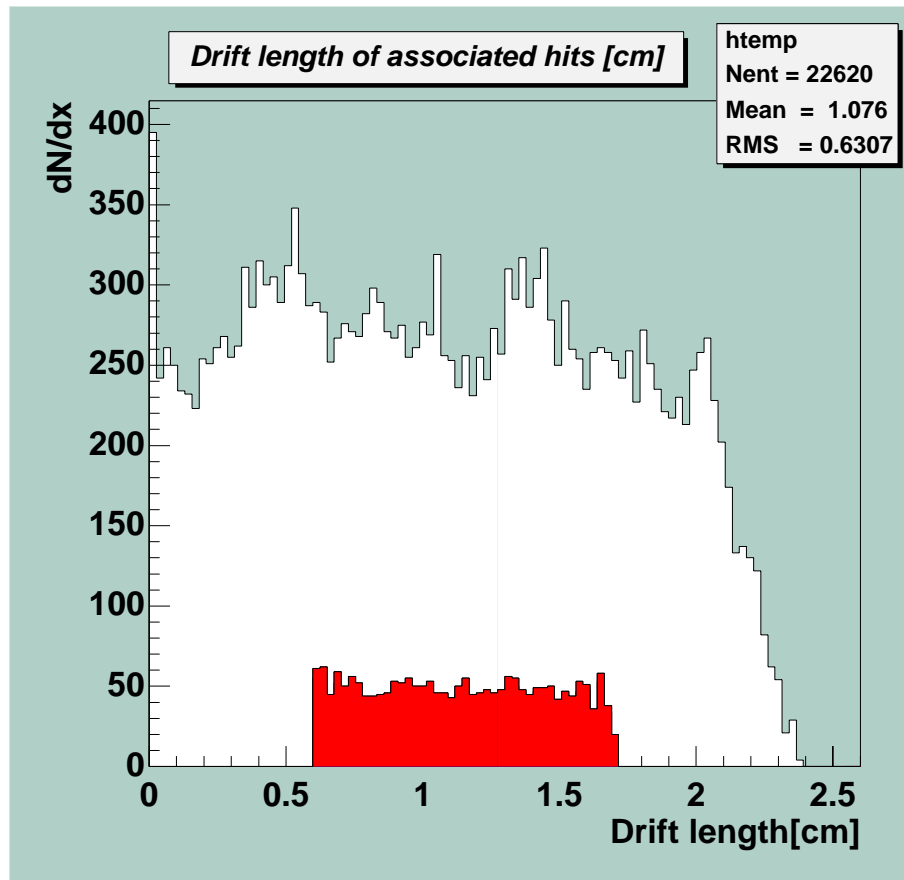


Figure 5.10: Distribution of the drift length of hits associated to reconstructed tracks (white histogram). The histogram plotted in black represents the hits that actually fulfill all requirements imposed by the cuts discussed above.

statement about the stereo wire efficiency, because the hit association is not yet reliable. The small association rate for stereo wires is probably due to the fact that the hits are associated by searching in a fiducial volume around the trajectory after a track candidate has been identified. Even when a hit has contributed to the Hough bin representing the track, it may be missed in

the association stage. Therefore, in the following only X wire efficiencies are discussed.

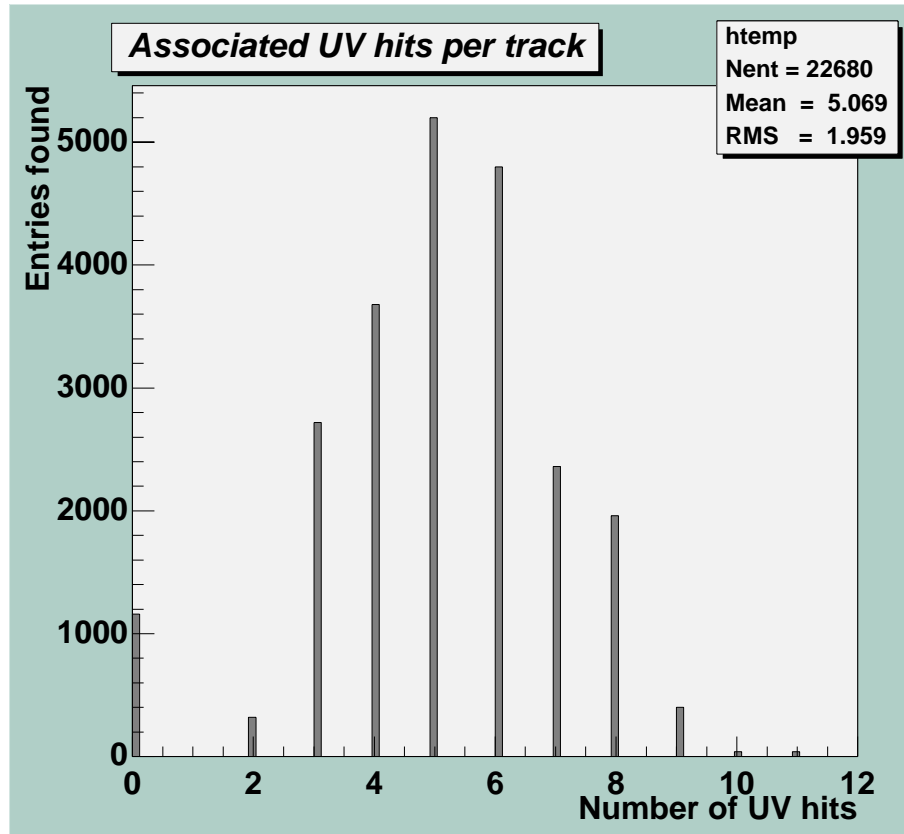


Figure 5.11: Number of stereo-wire hits associated to tracks.

One further restriction has been applied to the measurement. To avoid that cosmic-ray showers that triggered the data acquisition system distort the efficiency because of their higher multiplicity, events with more than one reconstructed track were excluded.

Measured Efficiencies

The single-wire efficiency depends on the voltage settings. Systematic measurements have been performed for the configurations given in Table 5.1. As an example Figures 5.12 and 5.13 show the display output of the efficiency reconstruction for the data set taken in run 3. In Fig. 5.12 the efficiency as a

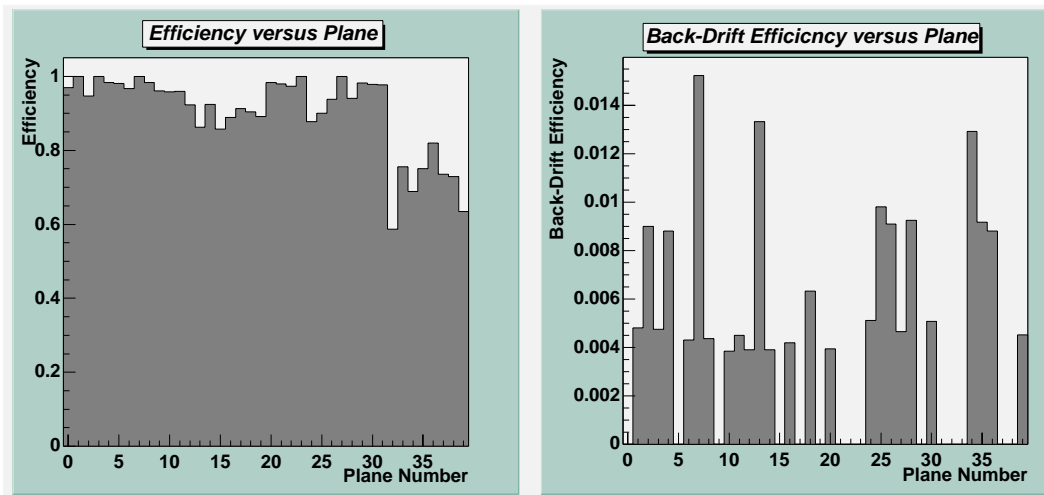


Figure 5.12: Efficiency and Back-Efficiency versus radial distance of the wires in the data set taken in run 3 (see Table 5.2).

function of the plane is shown on the left. A significantly lower efficiency for the outer stereo wires is apparent. The reason is not yet understood. On the right the back-drift efficiency is plotted. A back-drift efficiency of 0 means, that no back efficient wires have been found in a particular plane. Figure 5.13 shows on the left the efficiency as a function of the wire type. On the right side the efficiency of the X wires as a function of the drift distance is shown. Obviously the missing hits are lost in the back-drift region and at large drift

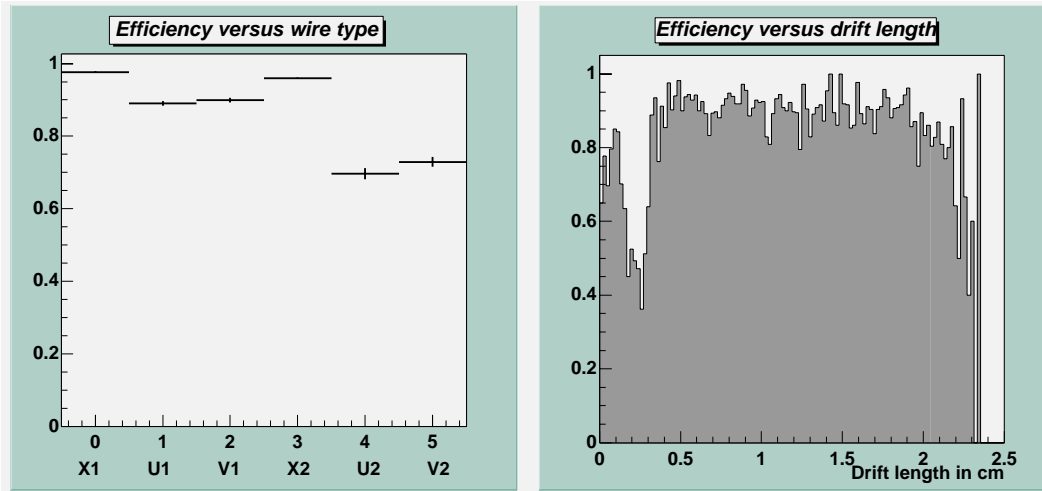


Figure 5.13: Left: Efficiencies of the different wire types in the drift chamber. Right: Efficiency as a function of drift distance (Data set taken in run 3).

lengths. The reason very likely is the inaccurate space drift-time relation. The measured efficiencies and back-drift efficiencies for all configurations are summarized in Table 5.2. The best efficiencies have been obtained in run 5, where both the potential-wire voltage was at its largest chosen value. At large potential voltages even small amounts of charge entering the avalanche region are amplified enough to create a signal. For the operation of the drift chamber one aims for an efficiency of $\approx 99\%$. The measured efficiencies are within reach of the design goal and a more thorough calibration and tuning of the voltage settings should easily bring the efficiency close to the expected values. A back-drift efficiency below 1.5% is already achieved in the chamber.

Run	X1 eff. [%]	X2 eff. [%]	X1 back-eff. [%]	X2 back-eff. [%]
0	98.20 ± 0.05	94.84 ± 0.14	0.32 ± 0.04	0.22 ± 0.03
1	94.78 ± 0.19	91.67 ± 0.31	0.50 ± 0.09	0.31 ± 0.06
2	96.49 ± 0.12	94.63 ± 0.19	0.46 ± 0.09	0.50 ± 0.10
3	97.61 ± 0.09	95.95 ± 0.15	0.35 ± 0.01	0.37 ± 0.01
4	97.01 ± 0.10	94.35 ± 0.21	0.27 ± 0.01	0.04 ± 0.00
5	98.82 ± 0.06	96.42 ± 0.21	0.07 ± 0.00	0.15 ± 0.00
6	95.39 ± 0.16	92.27 ± 0.29	0.21 ± 0.00	0.60 ± 0.01

Table 5.2: Efficiencies and back-drift efficiencies for the X wires for different voltage settings.

The back-drift efficiency of the drift chamber depends on the ratio of potential-wire voltage and back-wire voltage. It is expected, that above a ratio of about 0.34 the back efficiency rises. Figure 5.14 shows that the tendency is visible, although not very pronounced.

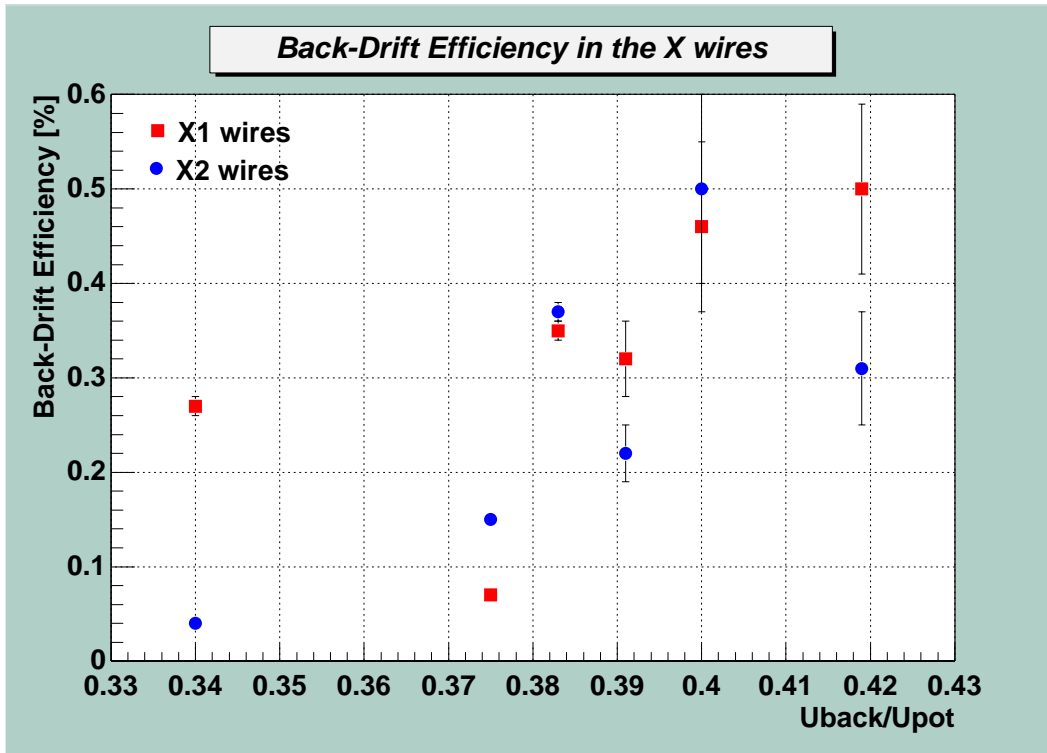


Figure 5.14: Back efficiency of the X wires as a function of the ratio U_{back}/U_{pot} .

5.2.3 Resolution Measurement

The distances between the hits and the trajectory they are associated with are assumed to be distributed according to a Gauss function. The width σ of this distribution is the quantity one refers to as resolution. It is a crucial quantity for accurate momentum measurements and for the proper separation of neighboring tracks. The design goal of the PHENIX DC is a resolution of $150 \mu\text{m}$ in the azimuthal plane. A two-track separation distance below 1.5 mm and a momentum resolution $\Delta p_t/p_t$ of $0.3\% \times p_t(\text{GeV})$ in the high momentum limit should be possible with these specifications. The actual value of the

resolution in the chamber must be monitored for different wire types or even single wires separately. It is a parameter that needs to be updated regularly in the PHENIX database for later event analysis. The online measurement of the resolution is described in this chapter.

Hit Distances in Drift Direction

To evaluate the resolution, one has to calculate the distance of the lines defined by the hit and the track *along the drift vector*. The intersection of the track with the local drift plane is therefore calculated as described in section 5.2.1. The difference between this intersection point and the drift distance of the hit is the residual as illustrated in Fig. 5.15.

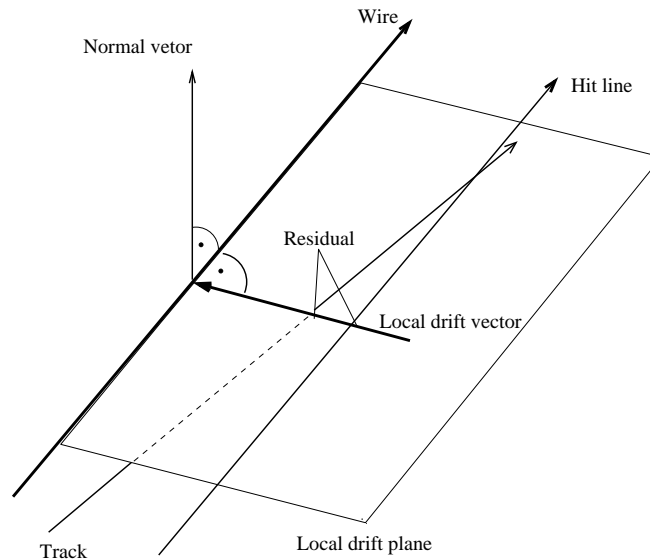


Figure 5.15: The punch-through point of the track through the local drift plane and the hit distance from the wire determine the residual.

Avoiding Autocorrelation Effects

Taking into account a particular hit when the track is fit to the associated hits biases the hits deviation from the reconstructed trajectory to a lower value. To avoid this so-called autocorrelation effect, one must exclude a specific hit and fit the remaining hits, before the distance of the excluded hit is determined. That way, the bias is avoided and the true deviation of the hit from the trajectory can be obtained. The elimination of autocorrelation effects is done by excluding all wires within one plane¹ from the fit. All tracks in the chamber are then reconstructed as if the wires in the excluded plane did not exist and the distances of the excluded hits from the corresponding tracks can be calculated as described above. In the following sections resolutions for Monte Carlo data and the cosmic-ray test are discussed.

5.2.4 Resolution in the Monte Carlo Data

The Monte Carlo data are generated with a realistic magnetic field taken into account. The currently used track model can only parameterize a track as a straight line. One therefore can not expect to reproduce the input resolution of $150\ \mu\text{m}$ exactly. Figures 5.16 and 5.17 show the resulting residual distributions for X1 and UV1 wires from the analysis of 35 central Au+Au events with several hundred tracks each. The distributions are fit to a gauss

¹In the drift chamber the 40 layers of sense wires are labelled by their radial position counted from the innermost wire outward. This number is referred to as the *plane* a particular wire belongs to.

function in a limited range. This range is chosen so that the fit to a Gaussian does not deviate from the measured distribution at large residuals.

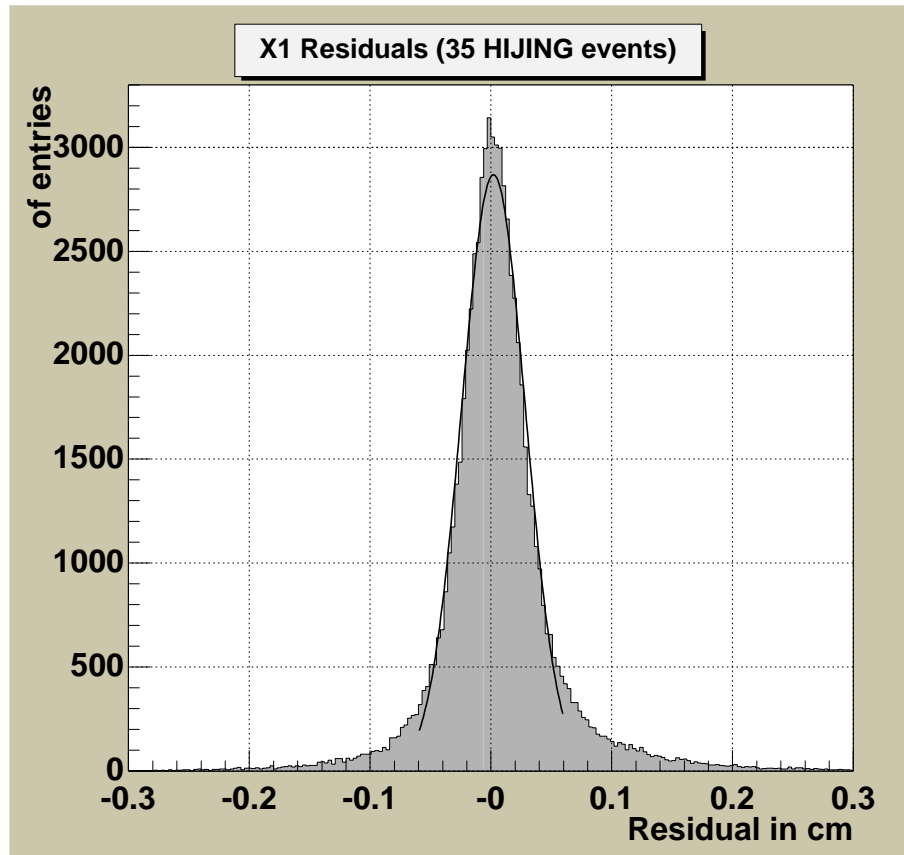


Figure 5.16: Residuals for the X1 wires for 35 central Au+Au events.

The broadening of the residual distribution and its deviation from a Gaussian outside the fit ranges is due to the residual bend of the tracks in the magnetic field and to multiple scattering of low momentum particles which is also simulated in the Monte-Carlo software. The chosen ranges and the resulting fit parameters for all wires are summarized in Table 5.3. For the X wires a resolution which is approximately $100 \mu m$ larger than the input resolution

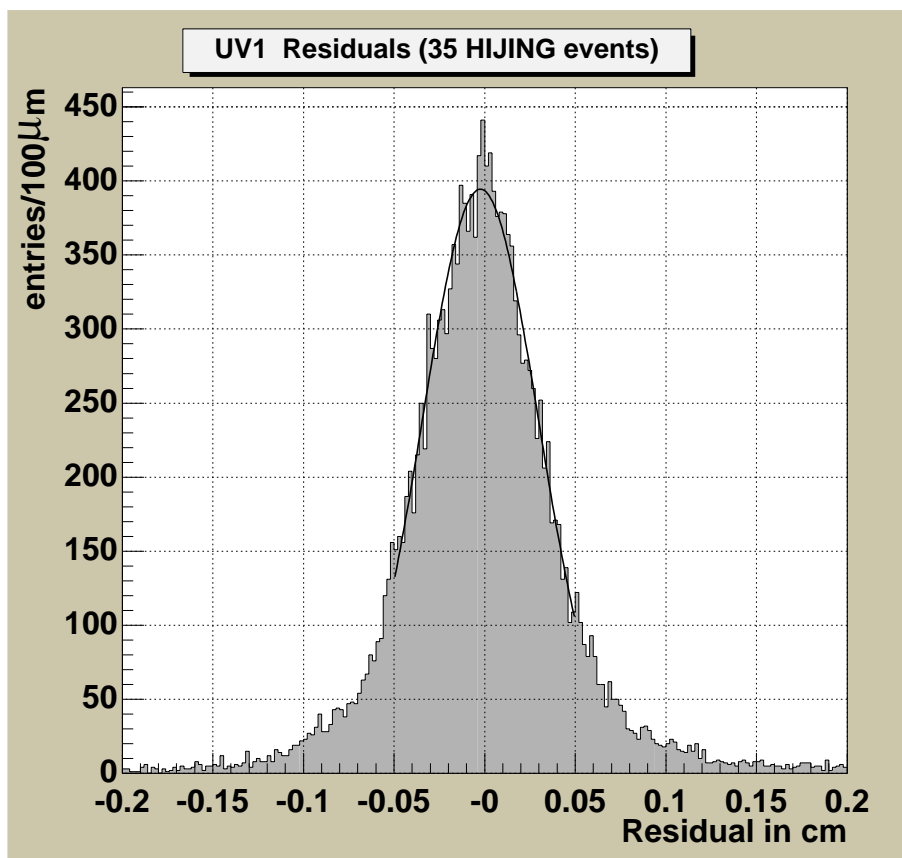


Figure 5.17: Residuals for the U1/V1 wires for 35 central Au+Au events.

has been reconstructed. For the stereo wires the measured resolution is about $200 \mu\text{m}$ larger than the input value.

A sophisticated track model is needed in order to address the bending of tracks in the residual field. The present straight line approximation does not allow for a realistic calculation of the resolution in case of data simulated or measured with magnetic field.

An interesting dependency of the residuals in the Monte Carlo simulation from the drift distance is seen in Figure 5.18. The X wire resolution is not only

Wire type	σ [μm]	fit range [μm]
X1	254	± 500
X2	243	± 600
UV1	342	± 800
UV2	383	± 800

Table 5.3: Resolutions and fit ranges for different wire types in the drift chamber.

better than the UV wire resolution as seen already in Tab. 5.3, but in addition it varies only slightly as a function of the drift length, whereas the UV wire resolution is getting worse with increasing drift length. This suggests, that especially corrections to the stereo wire fit are necessary. Ideally, one would perform a simultaneous fit to all wires at once that minimizes the distance in the corresponding drift directions as explained in chapter 5.2.3. For such a three-dimensional fit and a track model taking into account the magnetic field, the residuals should become identical for X and stereo wires and should reproduce the nominal value. The mean of the residual distribution of the X and stereo wires is shown in Figure 5.19 as a function of the drift distance. In an ideal case the mean should be zero. Instead systematic shifts to values that are slightly too large for X wires ($\approx 20 \mu m$ on the average) and slightly too

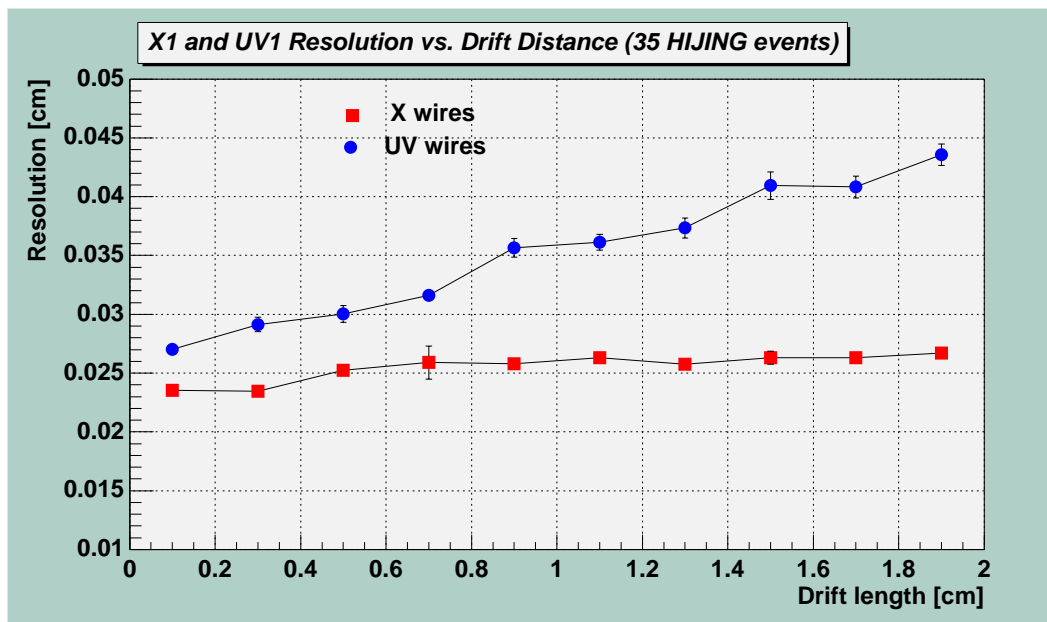


Figure 5.18: Resolution in X1 and UV1 wires versus drift length for simulated events.

small for the UV wires ($\approx 30 \mu m$ on the average) are observed. The deviations are small compared to the resolution of the reconstruction and are most likely due to the separation of the fit procedures in X and stereo wires.

Tracking parameters without field

To find out whether the reconstruction code can reproduce straight tracks a Monte Carlo file generated without magnetic field has been analyzed. The results are shown in Figures 5.20 and 5.21. Although a slightly better resolution is measured in the X wires there is no significant overall improvement. For the stereo wires no effect is observed at all. The main contribution to

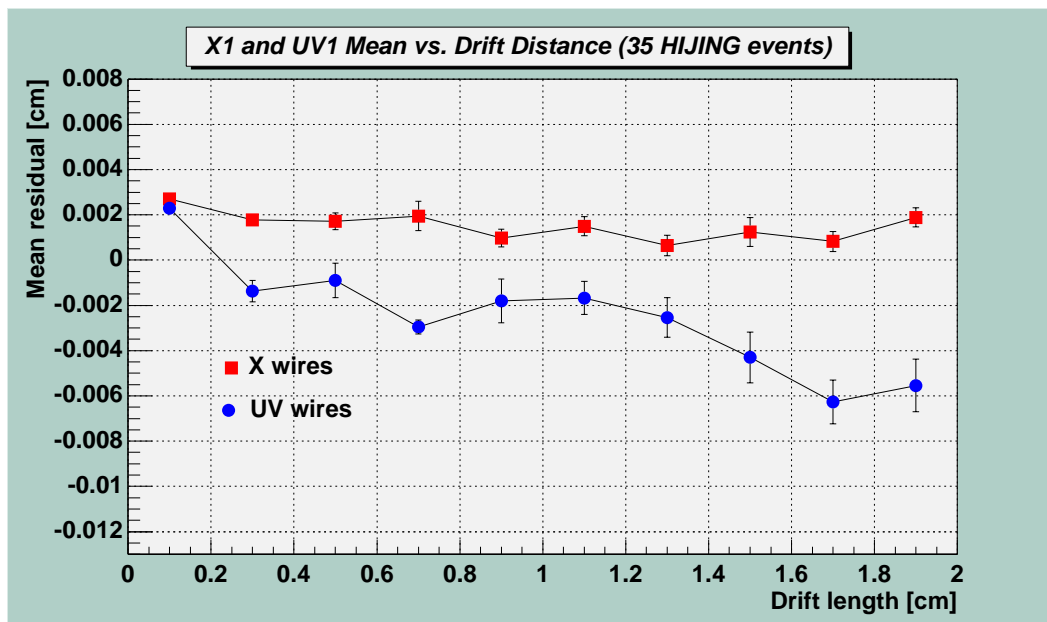


Figure 5.19: Mean residual in X1 and UV1 wires versus drift length for simulated events.

the broadening of the residual distribution therefore must stem from multiple scattering of low momentum particles. The mean deviation of hits from the tracks shows also no significant change. The general trend, that for the UV wires the residual grows towards larger negative values with increasing drift length, suggests that the drift-velocity assumed in the hit calibration is too large. This should not appear in simulated data and therefore consistency checks of simulation, reconstruction, and monitoring code may be necessary before these systematic deviations are eliminated.

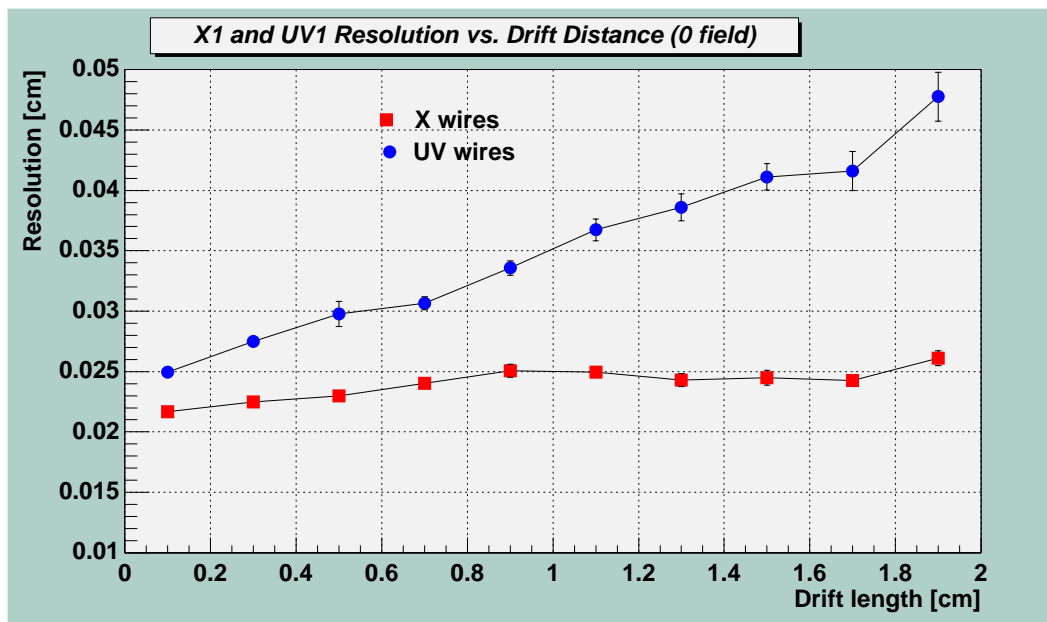


Figure 5.20: Resolution in X1 and UV1 wires versus drift length for zero magnetic field.

5.2.5 Resolution in the Cosmic-Ray Data

The resolution of tracks reconstructed from cosmic-ray data was measured with the same algorithm and with similar cuts as used in the measurement of the efficiencies (see chapter 5.2.1). There was no cut applied to the drift distance as the dependence of position and resolution is to be investigated. The resolution and the mean residual as a function of the drift length are shown in Figures 5.22 and 5.23, respectively *without* any cuts. Figure 5.22 shows that the resolution is clearly best in the middle of the drift cell. The rise at larger drift lengths may be an effect of diffusion of charge clouds along the drift lines towards the sense wire. The rise of the resolution in the back-drift region is

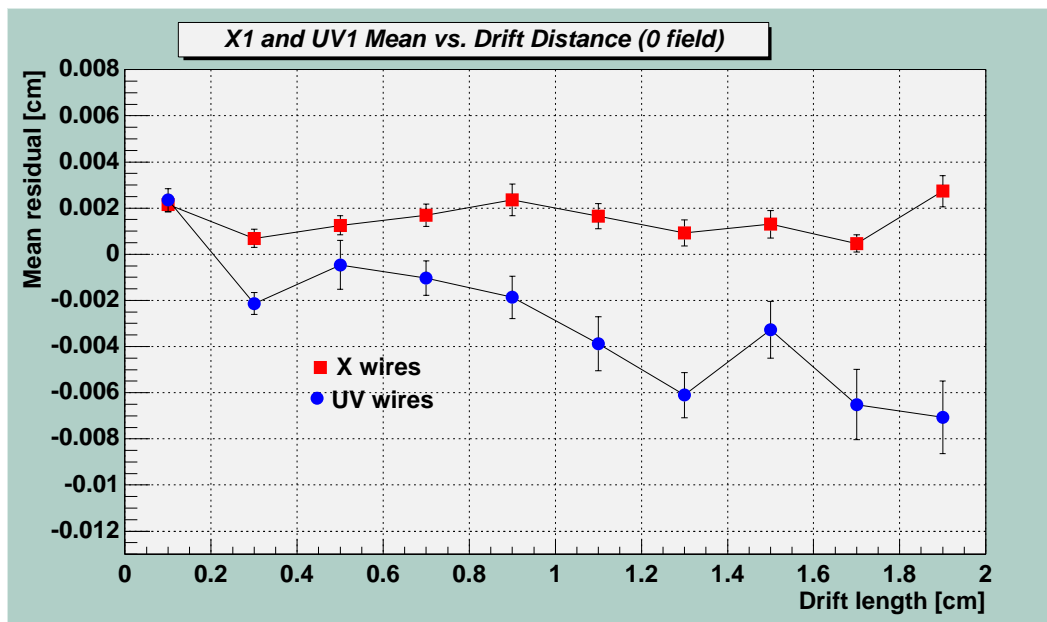


Figure 5.21: Mean residual in X1 and UV1 wires versus drift length for zero magnetic field.

due to deviations of the true space drift-time relation from the linear input relation. Apparently, for the drift region the resolution in both X and stereo wires is better than in the Monte Carlo data. Nevertheless, the nominal value of $150 \mu m$ is not reached without cutting on the used hits. Figure 5.23 shows that for stereo wires the mean deviation of the hits from the tracks in the drift region is similar to the value measured in the Monte Carlo data. The mean residual of the X wires in the drift region is now close to zero as it is expected. The large negative mean residual of the UV wires and the small positive offset in the X wire mean residual, observed in the back-drift region, are due to the inaccuracy of the space drift-time relation there.

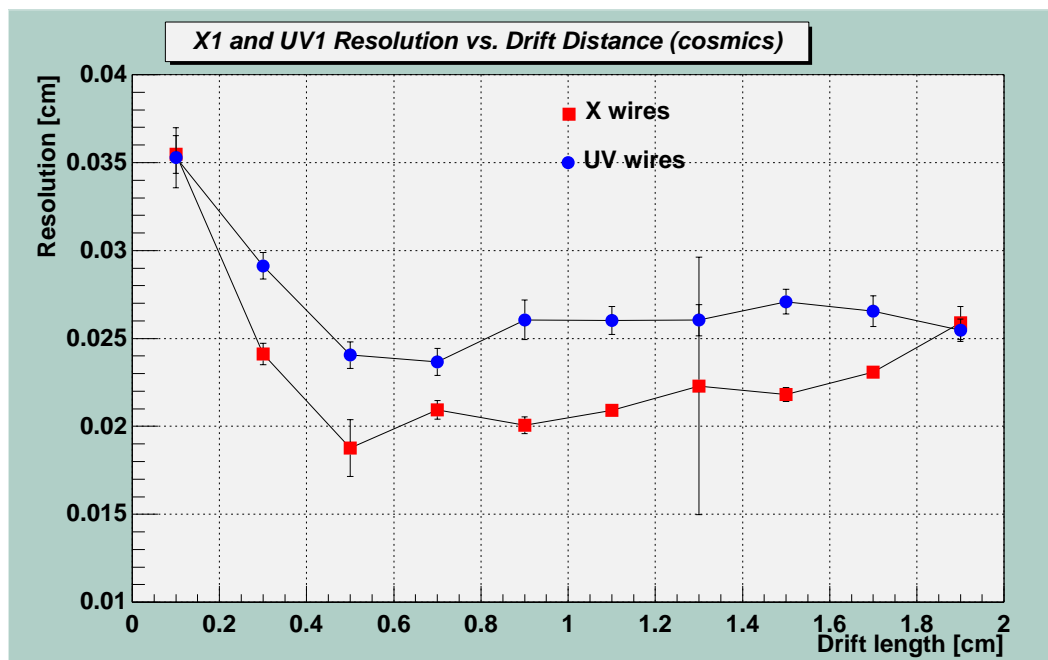


Figure 5.22: Resolution in X1 and UV1 wires versus drift length for cosmic-ray data.

Figures 5.24 and 5.25 show the resolution and the mean residual after making the same cuts used for the efficiency measurement described in chapter 5.2.2. To enhance the statistics the bin width has to be enlarged when the cuts are applied. For the same reason, also the second set of X and stereo wires is included into the analysis. A clear improvement in the resolution is visible over the complete drift length. The values for the X wires are now within reach of the nominal value. Except for the back-drift region the resolution is significantly better than in Monte Carlo data. There is no pronounced change in the mean of the residual distribution in the stereo wires when the cuts are used. However, in the region where the space drift-time relation is reliable, the

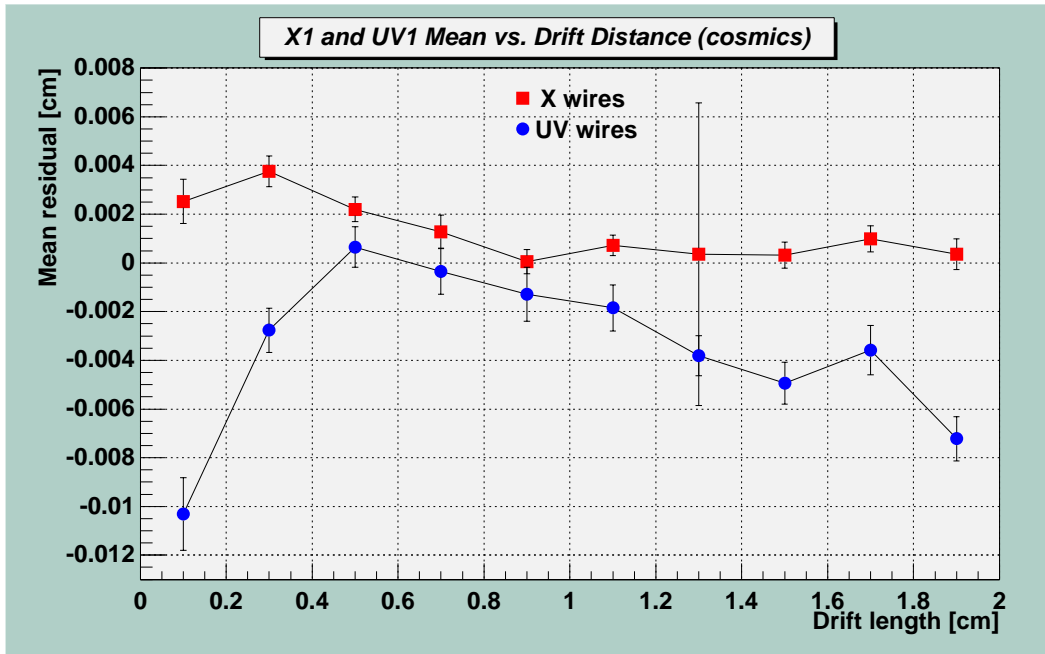


Figure 5.23: Mean residual in X1 and UV1 wires versus drift length for cosmic-ray data.

mean of the X wire residuals is clearly centered around zero now.

Although there are still improvements necessary, a design resolution of $150 \mu m$ is almost reproduced for the region with a reliable calibration. Taking into account that only a preliminary space drift-time relation was available, the results are encouraging. It remains to be checked, that the monitoring code and the tracking algorithm are 100% consistent with the Monte Carlo simulation, before corrections to the residual measurement can be optimized. A refined space drift-time relation is also needed.

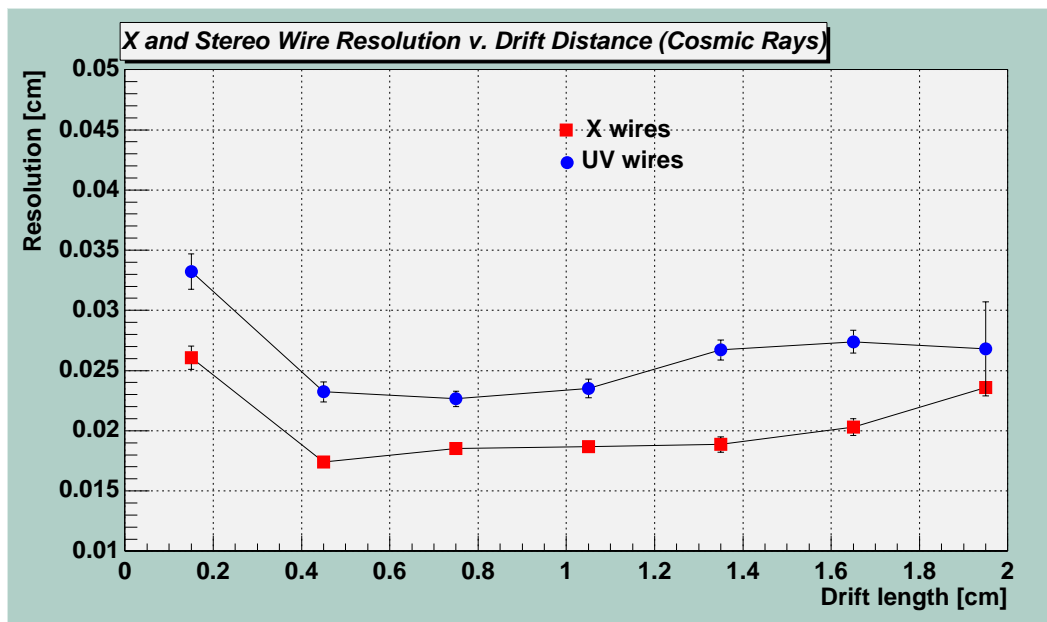


Figure 5.24: Corrected resolution in all X stereo wires versus drift length for cosmic-ray data.

Corrections to the Hit Calibration

For small and large drift distances the data points of the X wires in Fig. 5.25 are located at mean residuals larger respectively smaller than zero. Almost all data points of the stereo wires lie at negative values. As by convention the residual is defined as the track's distance to the wire minus the hit's distance to the wire, the sign of the shift indicates that, on the average, tracks registered by UV wires are closer to the wire than their associated hits. Thus, a too large drift velocity has been chosen for the stereo wires in the region where the space drift-time relation is trusted. For the X wires the sign of the deviation changes from small to large drift distances. Sign and magnitude of

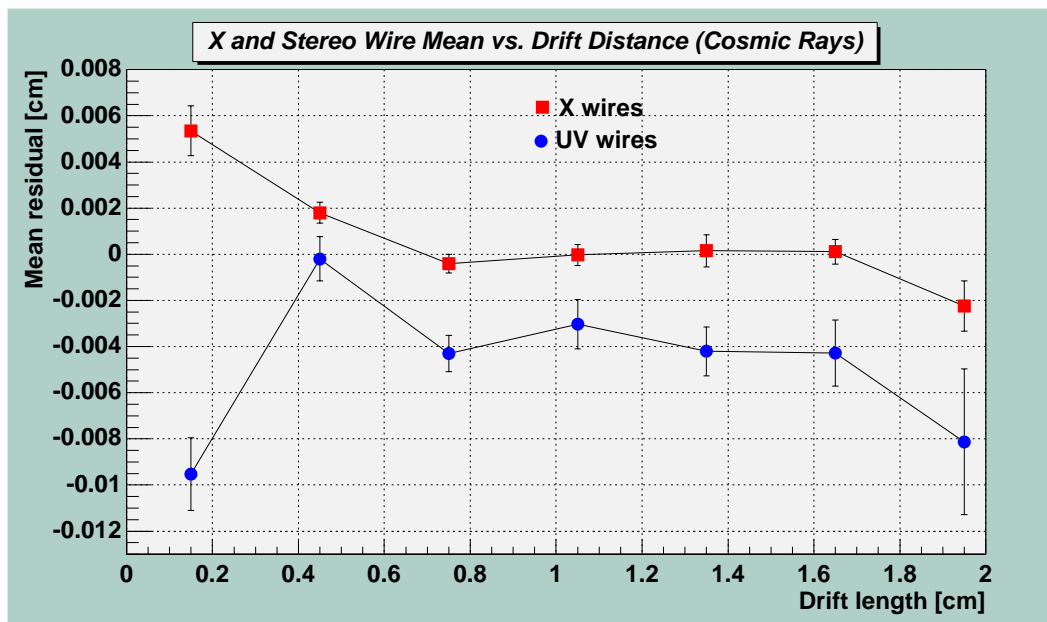


Figure 5.25: Corrected mean residual in all X and stereo wires versus drift length for cosmic-ray data.

the deviation thus can be used to tune the space drift-time relation. In the back-drift region the distances of hits on the UV wires from the sense wire are reconstructed with even larger negative mean. This can be understood from the shape of the reconstructed space drift-time relation: As the fit of the space drift-time relation is restricted to the drift region, the slightly smaller slope inside the back-drift region is bound to cause larger deviations of hits from the reconstructed trajectories. In the calibration, the slope, i.e. the drift velocity, is assumed to be the same inside and outside the drift region and thus the hits are systematically shifted to larger drift lengths. The position of the onset of the linear behavior is at approximately 15% of the maximum drift time (see

Fig. 4.17 to 4.19). The change of the slope in the mean deviation of hits on UV wires occurs at a drift length of $\approx 0.4\text{cm}$ which is roughly 15 % of the maximum drift length ($\approx 2.4\text{cm}$). The discontinuity in the space drift time relation therefore occurs at about the same point as the change in the slope of the mean residual plotted in Fig. 5.25. Furthermore, as explained above, the negative sign of the mean residual is in accordance with what one would expect. Further improvement of the resolution will be possible by using a more elaborate space drift-time relation that takes into account the discussed effects.

Chapter 6

Summary and Perspectives

6.1 Goals of the Thesis

The goal of the present thesis was to provide a set of analysis tools for measurement and evaluation of several basic drift chamber performance parameters. Testing and updating some aspects of the reconstruction software turned out to be also a necessary task. Compatibility of the drift-chamber online code with PHENIX coding conventions had to be established and maintained. Also contributions to the embedding of the track reconstruction software into the ROOT/PHOOL environment were made. Monte Carlo Data generated by the PHENIX simulation software were used to check the developed algorithms and to track down inconsistencies in the offline and simulation software. The field geometry and the space drift-time relation in the drift chamber at standard operating voltages were modeled with the wire-chamber simulation software GARFIELD. With the online monitoring tools, a space drift-time relation has been determined. Necessary corrections to the assumptions made for the

reconstruction have been discussed and ways to implement them have been identified. The single-wire efficiency and the resolution of the drift chamber have been measured using cosmic ray data.

6.2 Discussion of the Results

6.2.1 Space Drift-Time Relation

The measured space drift-time relation shows linear behavior outside the back-drift region. Closer to the anode wires deviations are visible. Assuming linear behavior over the entire drift length serves reasonably well as a first estimate for the reconstruction of the position of hits and the measurement of other parameters in the chamber. The shape of the functional dependence of drift time and position nevertheless needs to be determined more carefully. The key to an improved relation is a more sophisticated model of the reference hit distribution dN/dx that takes into account the correct drift lines in the back-drift region. The assumptions used in the calibration code are clearly oversimplified. Artifacts of the Monte-Carlo simulation of drift times have been found, which have to be investigated in more detail to make sure the simulated data are as close to the real detector response as possible. Further corrections to the space drift-time relation can also be made by exploiting the results of the measurement of the residual distribution which have been presented here.

6.2.2 Single-Wire Efficiency

The single-wire efficiency for the X wires of the chamber has been analyzed for several sets of voltage settings of the drift chamber. In addition, the back-drift efficiency has been studied. The results demonstrate, that efficiency and back-drift efficiency are at or very close to the design values of 99% and $< 1\%$, respectively. Improvements in the calibration and a thorough check of the hit association in the tracking software will be necessary to reconstruct stereo wire efficiencies in a reliable way.

6.2.3 Resolution

The spatial distribution of hits relative to the corresponding track has been measured for the different wire types. The reconstruction code could not quite reproduce the input position resolution of $150\mu m$ used for the generation of Monte Carlo data. The reasons are that low momentum particles that undergo multiple scattering are not excluded in the measurement and that there is no track model yet that takes a magnetic field into account. The average found resolutions are $\approx 250\mu m$ for the X wires and $\approx 350\mu m$ for the stereo wires. For cosmic rays the measured resolution is significantly better and also the mean residual is closer to the expected behavior than in simulated data. The design goal is almost reached for the X wires in the largest part of the drift region. As for both data sets the same analysis algorithm was used, the simulation software and the offline track reconstruction have to be investigated for discrepancies in the assumptions they make about the generation of hits

and about the computation of drift times.

6.3 Perspectives for the Monitoring Software

6.3.1 Algorithms

The software package DOOM has proven useful and reliable to a very large extent. The development is however not finalized. As the needs to monitor different parameters and to relate different variables to one another vary during the course of the analysis, the software has to be adapted to the specific requirements. Changes in the algorithms used for the different analyses in this thesis are e.g. necessary in the determination of the space drift-time relation. A better model of the reference distribution of hits in the drift chamber is needed. Also a method to automatically determine the edges of the drift-time distribution will be necessary once the calibration needs to be updated on a regular basis for reconstruction purposes. For real physics runs of PHENIX an automatic procedure to detect and report noisy and dead channels in the chamber has to be implemented.

6.3.2 Embedding into the PHENIX Software Development Process

DOOM uses many features of the PHENIX software library PHOOL. Nevertheless, PHOOL has capabilities for handling ROOT objects like histograms and ntuples that are not used yet, but may become valuable later. The recon-

struction software for the drift-chamber data has not been developed for the PHOOL/ROOT environment from the beginning and the modules will have to be tuned and adapted to this framework which in turn will probably require recoding some details of the online software. DOOM also needs an interface to the database in which the calibration data are stored. This has not yet been implemented in the current version, but PHENIX wide standards for this interface are under development.

6.3.3 Interactivity

Monitoring software is expected to run in an interactive mode. The user must have the ability to start, interrupt and resume a process. Graphical update of histograms on demand and reset functions of monitoring objects have to be made available. The basic requirement for this is multithreading capability of the software. This means that the objects instantiated for a monitoring process can be accessed by different processes at the same time. ROOT by default is not multithreaded. Therefore in the current version of the online software one needs to execute a predefined set of commands contained in a macro and can only use the output once the macro is finished. Interfacing a multithreaded ROOT version, which is expected to be available soon and DOOM is one of the major software goals that have to be achieved in order to provide an easy to use monitoring tool.

Bibliography

- [1] J.D. Bjoerken, Phys. Rev. D27 (1983), 140
- [2] For an introduction to the confining property of the strong interaction the reader is referred to standard text books on particle physics and field theory like e.g.: K.Gottfried and V.F. Weisskopf, Concepts in Particle Physics, Vols I and II, Oxford University Press, Oxford (1984)
and: George Sterman, An Introduction to Quantum Field Theory, Cambridge University Press (1993)
- [3] B. Petersson, Nuc. Phys. A 525 (1991), 237c
- [4] T. Hatsuda, Nuc. Phys. A 544 (1992), 27c
- [5] Lecture given by H. Satz at the 35th Course of the International School of Subnuclear Physics, (Erice 1997) - published in the proceedings
- [6] Cheuk Yin Wong, Introduction to High Energy Heavy-Ion Collisions, World Scientific (1994), Chapter 9
- [7] L.D. Landau and E.M. Lifshitz, Statistical Physics, Pergamon Press, Oxford (1980), Third Edition

- [8] Volker Koch, *Int. J. Mod. Phys. E6* (1997), pp 203-250
- [9] S.Klimt, M.Lutz, and W.Weise, *Phys. Lett. B* 249 (1990), pp 386-390
- [10] J. Friese, GSI Annual Report 1996
- [11] S.A. Bass, M. Gyulassy, H. Stoecker, and W. Greiner, *J. Phys. G: Nucl. Part. Phys.* 25 (1999) , R1-R57
- [12] *Nuc. Phys A* (1998), 261c-278c
- [13] L. Van Hove, *Phys. Lett. B* 118 (1982), 138
- [14] The NA44 Collaboration, *Phys.Lett. B*471 (1999), pp 6-12
- [15] X.N. Wang, *Phys.Rev. C*58 (1998), 2321
- [16] M. Gyulassy and M. Pluemer, *Phys. Lett B* 243 (1990), 432
- [17] D. Lissauer and E.V. Shuryak, *Phys. Lett. B* 253 (1991), 15
- [18] PHENIX Conceptual Design Report, BNL (1993), (unpublished)
- [19] W. Blum and L. Rolandi, *Particle Detection with Drift Chambers*, Second Edition, Springer Verlag (1994)
- [20] *Particle Physics Data Booklet*, Particle Data Group, Springer (1998)
- [21] A. Vorobyov et. al., *Monitoring of electron drift velocity in drift chambers with a decay recoils*, PNPI preprint (1990), 1582

- [22] An introduction into the Garfield DC simulation program is given on the CERN web pages at the URL:
<http://consult.cern.ch/writeup/garfield/>
- [23] The ROOT web pages provide an introduction into data analysis with ROOT: *<http://root.cern.ch/>*
- [24] D. Ben-Tzvi and M.B. Sandler, Pattern Recognition Lett. 11 (1990) 167
- [25] Stephen C. Johnson, John W. Noe, Federica Ceretto, Axel Drees, Thomas K. Hemmick, and Barbara Jacak, Presentation at 'Computing in Nuclear and High Energy Physics 1998' (CHEP '98)

Appendix A

Calibration Software Overview

A.1 Drift Chamber Object Oriented Monitoring Library

A.1.1 Dependencies upon other Software Modules

Drift Chamber Offline Reconstruction Code

The drift chamber offline reconstruction code is used by DOOM. It is segmented into modules that execute unpacking, calibration, and tracking routines as well as simulation and evaluation procedures. The modules are called by DOOM objects using the standard PHOOL commands to find, manipulate, and write data. The code is separated into two libraries defining the methods and the data types they use for input and output. It is available to DOOM as a shared library.

PHENIX Object Oriented Library

The PHOOL tools are contained in a shared library object that DOOM is linked with during compilation. It provides the framework for instantiation of data objects and execution of reconstruction code.

PHENIX Event and DCM Libraries

The Event library provides the event iterator classes as interface for the monitoring process to data sources. It also defines the event format. The DCM (Data Collection Module) library is used to extract drift-chamber information from an event once it has been stored in the PHOOL tree structure.

Customization Tool

To switch off noisy or not responding channels and to disable parts of the detector for a particular analysis, a customization tool with graphical user interface has been written for DOOM. It defines a configuration object which is created independently of a particular process and can be read in and used by several processes at a time.

A.1.2 Available Monitor Objects

The class library that contains the monitor objects is named “libDOOM.so”. The classes in this library and their purposes are described briefly in the following.

oMonitor A base class that has been provided by the online computing group

to ensure future compatibility of online and calibration code from different subsystem. It is the smallest common denominator of all online needs.

DchBaseMonitor The drift chamber monitoring base class. It is derived from `oMonitor` and is the base class from which all drift chamber calibration classes inherit in turn. It provides PHOOL event-handling features and introduces the customization tool. Its analysis member functions are all virtual functions and by default overridden in the child classes.

DchSDTRMonitor Instances of this class are used to obtain the space drift-time relation from Monte-Carlo data. It provides member functions to create the spatial reference distributions and to measure drift-time distributions. It performs the integration of the drift-time and reference distribution and the fit to the model function.

DchChannelMonitor The `ChannelMonitor` is used for both Monte Carlo and cosmic-ray data to create and update a display of the activity of the wires in the complete chamber or in particular boards. It is used to find dead and hot channels. It loads a customization object, unpacks event data, and fills the distribution histograms for the channels selected in the customization process.

DchGlobalResolutionMonitor This object can be used to determine the resolution from reconstructed Monte Carlo data. Its member functions call a drift chamber tracking module that finds the residuals and fill

histograms event-by-event for each wire type with the determined resolutions.

DchCosmicMonitor For the cosmic-ray test the methods for reconstructing drift times and positions needed to be corrected for the reference time. In PHENIX the common reference time of all signals is the RHIC clock. For cosmic rays one particular channel in the drift chamber is used to set the reference time. The CosmicMonitor finds the reference time and computes all times with respect to it. After the time spectrum has been corrected, the functions to find the space-drift time relation and the resolution are called in the same way as in the monitoring objects described above. Efficiency measurement for Monte Carlo and real data is implemented also in this class.